Check for updates

Advanced Energy Materials

ADVANCED ENERGY MATERIALS
www.advenergymat.de

REVIEW

Rational Design of High-Voltage Lithium-Ion Batteries: From Multiscale Mechanisms to Scalable Manufacturing

Zhong Xu[1,2,3] | Weiqing Yang[1,3]

[1]School of Materials Science and Engineering, Key Laboratory of Advanced Technologies of Materials (Ministry of Education), Southwest Jiaotong University, Chengdu, China | [2]Yibin Research Institute of Southwest Jiaotong University, Yibing, China | [3]Research Institute of Frontier Science, Southwest Jiaotong University, Chengdu, China

Correspondence: Weiqing Yang (wqyang@swjtu.edu.cn)

Received: 27 February 2026 | **Revised:** 18 April 2026 | **Accepted:** 6 May 2026

Keywords: degradation and thermal safety | electrode preparation technologies | high-voltage lithium-ion batteries | interfacial stability | multiscale coupling mechanisms

ABSTRACT

High-voltage lithium-ion batteries (HVLIBs) are increasingly considered promising candidates for meeting the growing demand for high energy density and extended cycle life in electric vehicles and grid-level energy storage. However, the performance and stability of HVLIBs are critically influenced by fabrication techniques, including dry/wet processing, in situ polymerization, and advanced electrode engineering. These methods shape the architecture of electrodes and directly affect the electrochemical behavior under high-voltage conditions, where challenges such as electrolyte oxidation, gas evolution, and cathode degradation become more accelerated. The fabrication processes are inherently coupled with multiscale phenomena, from atomic-level redox reactions and interfacial reconstruction to microscale mechanical failure and system-scale safety issues. In this review, we focus on recent advances in the processing and structural design strategies for HVLIBs, emphasizing how these approaches interact with complex physicochemical mechanisms across multiple scales. We discuss state-of-the-art characterization tools, multiscale modeling, and data-driven techniques that are employed to elucidate the intricate correlations between processing, structure, and performance. Finally, we identify key challenges and propose future directions to integrate scalable fabrication techniques with mechanistic insights, aiming to enable the rational design of next-generation high-voltage lithium-ion batteries.

1 | Introduction

The growing demand for high-performance energy storage solutions, driven by advancements in electric vehicles, grid-scale storage, and aerospace technologies, has accelerated the development of high-voltage lithium-ion batteries (HVLIBs). By expanding the operational voltage window, HVLIBs offer significantly higher energy densities than conventional lithium-ion systems, making them a key enabler for next-generation energy technologies [1–3]. Moreover, they play an essential role in supporting the global transition to sustainable and low-carbon energy infrastructures by facilitating the efficient storage and utilization of intermittent renewable energy sources such as solar and wind.

Despite their promise, the practical implementation of HVLIBs faces considerable challenges, particularly in terms of material stability and interfacial compatibility under high-voltage operation. Conventional electrode fabrication methods, such as slurry casting and calendaring, often fall short when applied to high-voltage chemistries due to issues such as electrode cracking, poor electrolyte wettability, and enhanced interfacial side reactions. To address these limitations, advanced manufacturing approaches, including dry electrode processing, three-dimensional structured

© 2026 Wiley-VCH GmbH

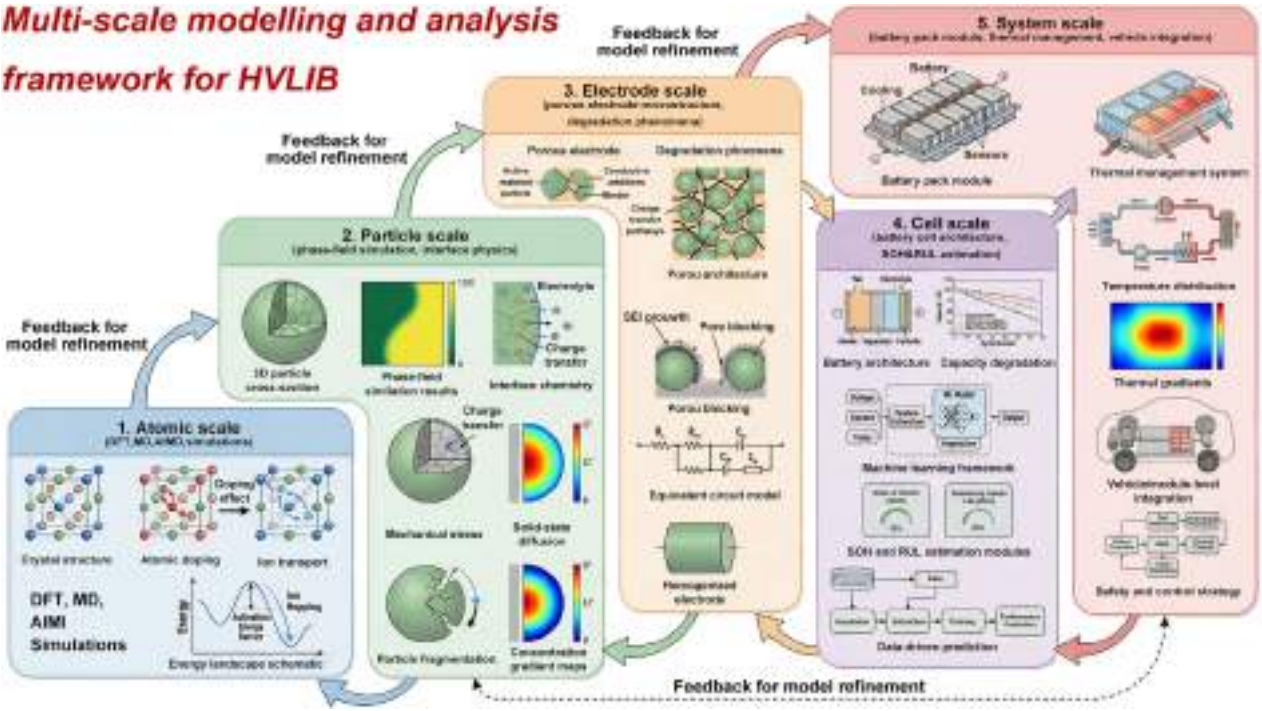


FIGURE 1 | Schematic illustration of the complex multiscale modeling and analysis framework for a high-voltage lithium-ion battery system [5].

electrodes, and in situ polymerization, are actively being investigated to improve mechanical robustness and electrochemical performance [4].

In addition to fabrication techniques, HVLIBs are governed by complex multiscale coupling phenomena, ranging from atomic-level electronic structure changes to mesoscale mechanical deformation and macroscale thermal effects (Figure 1) [5]. Under repeated high-voltage cycling, stress accumulation, volume expansion, and parasitic reactions can result in electrode degradation, electrolyte decomposition, and the formation of unstable interphases such as the solid electrolyte interphase (SEI) and cathode electrolyte interphase (CEI). These processes collectively contribute to capacity fading, increased impedance, and safety concerns. A comprehensive understanding and precise control of these coupled degradation mechanisms are therefore essential to enhancing the reliability, cycle life, and overall performance of high-voltage lithium-ion batteries.

Several recent review articles have summarized significant advances in high-voltage lithium-ion batteries (HVLIBs), particularly in areas such as electrolyte formulation, electrode stabilization, and advanced material design. However, a systematic review that specifically highlights the interplay between electrode/electrolyte forming technologies and the resulting multiscale physicochemical coupling mechanisms remains lacking. To address this gap, the present review aims to elucidate how various fabrication strategies influence the evolution of coupled degradation and stabilization processes across multiple length and time scales, "from initial electrode formation to long-term electrochemical cycling". To this end, the structure of this review is organized as follows. Section 2 summarizes the key challenges of HVLIBs, including cathode instability, electrolyte incompatibility, interfacial degradation, and limitations in solid-state systems. Section 3 presents advanced characterization and simulation techniques for probing high-voltage degradation mechanisms. Section 4 established process-structure-performance relationships by linking fabrication routes of electrodes, solid-state electrolytes, and battery manufacturing strategies to their structural and interfacial outcomes. Section 5 further integrates these insights into a multiscale coupling framework, correlating preparation processes with interfacial evolution and device-level performance. Finally, we conclude with perspectives on how combining mechanistic understanding with scalable processing can enable next-generation high-voltage lithium-ion batteries.

2 | The Key Issues Associated With High-Voltage Lithium-Ion Batteries

In the following subsections, we briefly outline the key challenges facing HVLIBs. These issues are inherently interconnected, arising from the strong coupling between materials chemistry, interfacial reactions, and electrochemical operating conditions. Specifically, challenges related to the structural and chemical stability of cathode materials, electrolyte compatibility, and electrode/electrolyte interfacial stability are closely linked and often mutually reinforcing. In addition, the development of solid-state batteries introduces new interfacial and transport limitations, highlighting the need for coordinated regulation across materials and interfaces.

2.1 | Structural and Chemical Stability of High-Voltage Cathode Materials

The dissolution of transition metal ions from cathode materials is a major contributor to capacity fading in batteries [6–8].

16146840, 2026, 26, Downloaded from https://advanced.onlinelibrary.wiley.com/doi/10.1002/aenm.71073 by Jilin University, Wiley Online Library on [07/11/2026]. See the Terms and Conditions (https://onlinelibrary.wiley.com/terms-and-conditions) on Wiley Online Library for rules of use; OA articles are governed by the applicable Creative Commons License

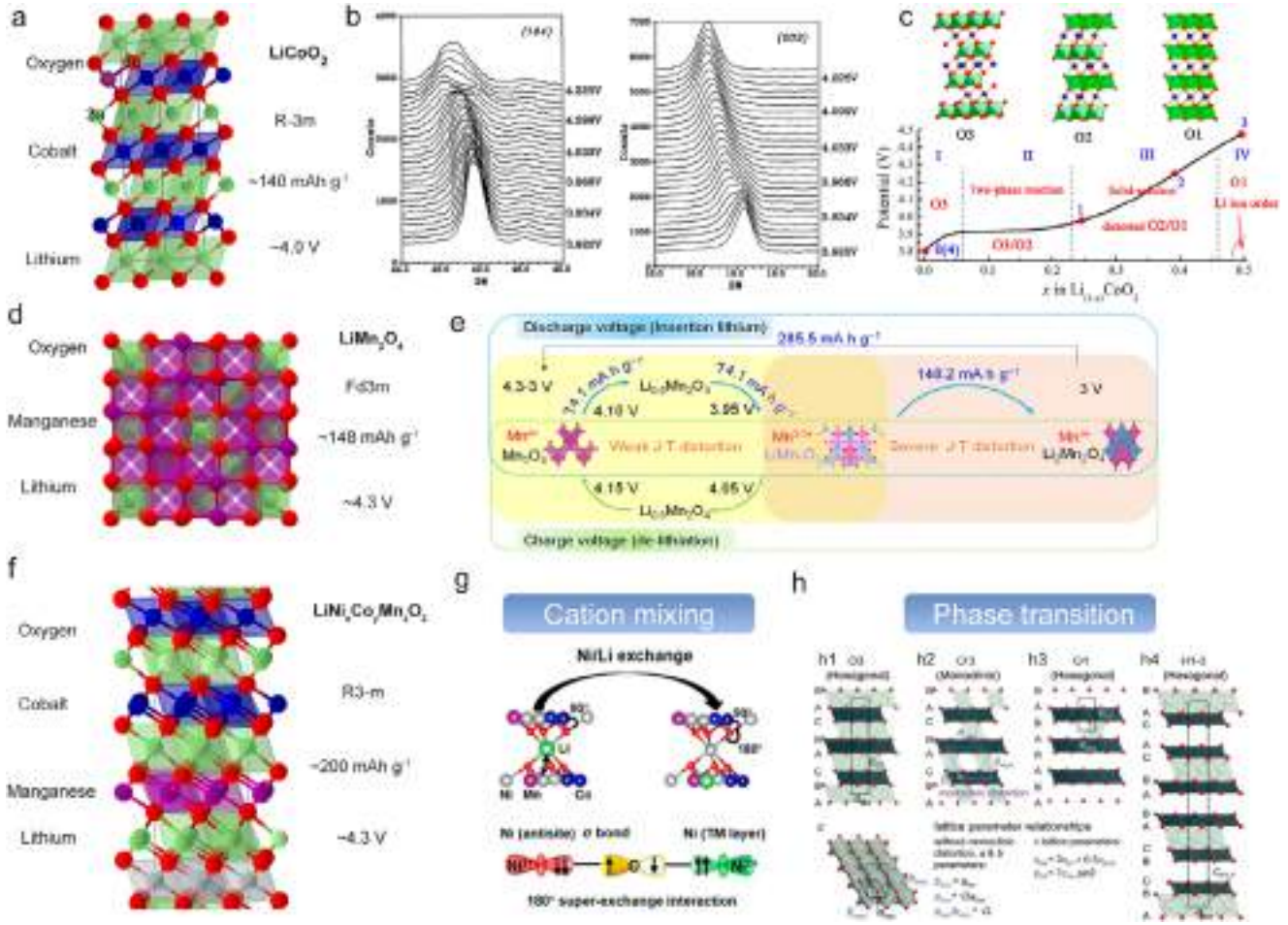


FIGURE 2 | (a) Crystal structure of $LiCoO_2$. (b) The formation process of a lithium ion superlattice in $LiCoO_2$ near 4.1 V and 3.93 V [13]. Copyright, Electrochemical Society, Inc. (c) The possible phase diagram of $Li_{(1-x)}CoO_2$ ($0 \leq x \leq 0.50$) [14]. Copyright, American Chemical Society. (d) Crystal structure of $LiMn_2O_4$. (e) Charging–discharging process of $LiMn_2O_4$ [1, 15]. Copyright, Elsevier. (f) Crystal structure of $LiNi_xCo_yMn_zO_2$. (g) Ni/Li exchange (disordering) process in layered $LiNi_xCo_yMn_zO_2$ materials [1, 16]. Copyright, American Chemical Society. (h) Illustrations of crystal structures relevant to layered Ni-rich cathodes [2, 17]. Copyright, John Wiley & Sons, Ltd.

Lithium hexafluorophosphate ($LiPF_6$), the most widely used salt in commercial electrolytes, exhibits limited thermal and chemical stability [9]. In the presence of trace amounts of water, $LiPF_6$ decomposes to generate LiF and hydrofluoric acid (HF). The HF formed further reacts with surface species such as Li_2CO_3 and LiOH on the electrode, producing CO_2 and H_2O, which leads to continuous consumption of lithium salt in the electrolyte. Meanwhile, the generated LiF tends to deposit on electrode interfaces and separator surfaces, impeding Li^+ transport and increasing interfacial resistance [10]. Hu et al. reported that once the concentration of LiF reaches a critical threshold, it begins to corrode the cathode material, leading to the dissolution of transition metal ions from the bulk phase [11]. These dissolved ions migrate through the electrolyte toward the anode, where they are incorporated into the SEI layer or reduced to metal.

2.1.1 | $LiCoO_2$

In 1980, Goodenough and coworkers first discovered the reversible electrochemical de/lithiation behavior of $LiCoO_2$, laying the foundation for its use as a cathode material in LIBs [12]. However, due to its relatively high operating voltage, the electrolytes available at that time could not adequately meet the requirements for stable cycling with $LiCoO_2$ cathodes. With the continuous advancement of electrolyte formulations, a range of high-voltage electrolytes has since been developed, enabling $LiCoO_2$ to become one of the earliest high-voltage cathode materials to achieve large-scale commercialization. $LiCoO_2$ crystallizes in the $R\bar{3}m$ space group and adopts an O3-type layered structure based on ccp oxygen anions arranged in an ABCABC. stacking sequence along the (001) direction, occupying the 6c positions. Li^+ and Co^{3+} ions alternately occupy the octahedral interstices of the ccp oxygen lattice at the 3a and 3b sites, respectively, as illustrated in Figure 2a.

During the de/lithiation process, the structural evolution of $LiCoO_2$ is highly dependent on the extent of lithium extraction. When the delithiation level is between 7% and 25%, the c-axis undergoes an expansion of approximately 2%, while Co–Co bond lengths shorten, leading to band splitting and overlap of the valence and conduction bands, thereby increasing the electronic conductivity [13] (Figure 2b). Between 25% and 50% delithiation, the layered structure remains largely unchanged.

16146840, 2026, 26, Downloaded from https://advanced.onlinelibrary.wiley.com/doi/10.1002/aenm.71073 by Jilin University, Wiley Online Library on [07/11/2026]. See the Terms and Conditions (https://onlinelibrary.wiley.com/terms-and-conditions) on Wiley Online Library for rules of use; OA articles are governed by the applicable Creative Commons License

At approximately 50% delithiation, however, a transition from disordered to ordered Li^+ arrangement occurs, accompanied by a phase transition from hexagonal to monoclinic symmetry. Using advanced ABF-STEM, Lu et al. were the first to construct the transformation sequence among the O1, O2, and O3 phases during electrochemical cycling [14]. Specifically, when the delithiation level is between 7% and 25%, the O3 phase transforms into O2; between 25% and 45%, O2 transitions to O1; and from 43% to 52% delithiation, O2 further converts to O1 (Figure 2c). Theoretically, complete Li^+ extraction from $LiCoO_2$ yields a specific capacity of 274 mAh g^{-1}. In practical applications within the voltage window of 2.5–4.2 V, approximately 50% of Li^+ can be reversibly intercalated/deintercalated, corresponding to a practical specific capacity of ~137 mAh g^{-1}. However, excessive delithiation often leads to irreversible structural collapse, severely limiting the reversible capacity and consequently constraining the achievable energy density of $LiCoO_2$-based LIBs.

2.1.2 | $LiMn_2O_4$

Spinel-structured lithium manganese oxide (LMO) has attracted increasing attention due to its environmental benignity and inherent safety. In 1983, Thackeray et al. first proposed spinel-structured $LiMn_2O_4$ as a promising cathode material [18]. This compound crystallizes in a cubic system with a space group of $Fd\bar{3}m$. Within its structure, oxygen atoms form a face-centered cubic (FCC) array, occupying the 32e sites, while lithium and manganese atoms occupy the 8a and 16d sites, respectively. This configuration results in a robust three-dimensional tunnel framework, as illustrated in Figure 2d, which provides Li^+ ions with continuous pathways for insertion and extraction. The theoretical capacity of $LiMn_2O_4$ is approximately 148 mAh g^{-1}. Due to its interconnected three-dimensional lithium-ion diffusion channels, Li^+ ions can reversibly intercalate into and deintercalate from the spinel lattice without inducing structural collapse, endowing $LiMn_2O_4$ with excellent rate capability and cycling stability. During lithium insertion and extraction, $LiMn_2O_4$ undergoes distinct phase transitions characterized by two major voltage plateaus centered at approximately 4.0 V and 3.0 V (vs. Li^+/Li). The higher-voltage plateau near 4.0 V corresponds to the extraction and insertion of Li^+ ions from the tetrahedral 8a sites, during which the spinel lattice retains its cubic symmetry. When the cell is deeply discharged, an additional plateau appears near 3.0 V, associated with Li^+ ions occupying the vacant octahedral 16c sites. This additional insertion induces structural distortions within the spinel lattice, transforming the cubic phase toward a more tetragonal configuration. Such distortions are driven by the Jahn–Teller effect, which arises from the reduction of Mn ions from an average oxidation state of +3.5 to +3.0, leading to cooperative distortions of the MnO_6 octahedra (Figure 2e).

Under high-voltage operation, even trace amounts of dissolved manganese can migrate from the cathode to the anode, resulting in significant capacity loss and a shortened cycle life. Three primary mechanisms contribute to the capacity fading of $LiMn_2O_4$. First, the presence of high-spin Mn^{3+} ions with an asymmetric electronic configuration ($t_2g^3e_g$ [1–3]) makes them structurally unstable. To stabilize these ions, the MnO_6 octahedra undergo Jahn-Teller (J-T) distortions, where the two axial Mn–O bonds elongate and the four equatorial Mn-O bonds contract [19]. Typically, this leads to a symmetry transition from cubic to orthorhombic near room temperature. During electrochemical delithiation, the J-T distortion accelerates structural degradation, resulting in the formation of $Li_2Mn_2O_4$ and compromised lattice integrity. Second, the high-spin Mn^{3+} ions make $LiMn_2O_4$ susceptible to manganese dissolution through a disproportionation reaction ($2Mn^{3+} \rightarrow Mn^{2+} + Mn^{4+}$) [20]. Experimental evidence suggests that even at typical operating potentials, soluble Mn^{2+} species are present in the electrolyte, likely originating from Mn_3O_4 species that readily dissolve in organic electrolytes [21]. Third, oxygen loss within the cathode structure reduces the mobility of Mn ions and triggers irreversible phase transformations, such as the formation of Li_2MnO_3, Mn_3O_4, or lattice rearrangements, all of which contribute to capacity decay. Moreover, the accumulation of dissolved Mn species can obstruct lithium-ion transport pathways, further deteriorating cycling performance and reducing the overall energy density [22–24].

2.1.3 | $LiNi_xCo_yMn_zO_2$

Due to the inherent Jahn–Teller distortion in spinel-structured $LiMn_2O_4$, which leads to poor cycling performance, the development of alternative cathode materials has become imperative. Layered ternary cathode materials with the general formula $LiNi_xCo_yMn_zO_2$ (NCM) have been rapidly developed and commercialized because they combine the respective advantages of $LiCoO_2$ (high structural stability), $LiNiO_2$ (high capacity), and $LiMnO_2$ (low cost). These materials exhibit high theoretical specific capacities and operating voltages along with superior electrochemical stability, making them one of the most widely studied and applied cathode families for lithium-ion batteries [25]. The crystal structure of $LiNi_xCo_yMn_zO_2$ is isostructural with $LiCoO_2$ and $LiNiO_2$, belonging to the layered $R\bar{3}m$ space group, in which the transition metal layer is randomly occupied by Ni, Co, and Mn cations (Figure 2f). Compared with $LiNiO_2$, the ternary system offers higher structural and chemical stability while providing greater energy and capacity densities than $LiCoO_2$. By carefully optimizing the Ni-Co-Mn ratio, these materials can achieve a desirable balance of high capacity, excellent cycling stability, and good rate capability. For instance, $LiNi_{0.3}Co_{0.3}Mn_{0.3}O_2$ (NCM111) was one of the early compositions adopted in electric vehicles.

However, as the demand for higher driving ranges in electric vehicles has increased, enhancing the specific capacity and energy density of lithium-ion batteries has become critical. Consequently, Ni-rich layered cathode materials have attracted widespread attention in both academia and industry due to their high discharge capacities (200–250 mAh g^{-1}) and elevated operating voltages (~4.3 V vs. Li^+/Li). With advances in synthesis and processing techniques, compositions such as $LiNi_{0.6}Co_xMn_{0.4-x}O_2$ (x = 0.05, 0.10, 0.15, 0.2) and $LiNi_{0.8}Co_{0.1}Mn_{0.1}O_2$ (NCM811) have been successfully developed, exhibiting outstanding electrochemical performance, including high specific capacity, which makes them promising candidates for high-energy battery applications [26]. In these materials, the redox activity of Ni^{2+}/Ni^{4+} is primarily responsible for capacity delivery. Hence, a higher Ni

16146840, 2026, 26, Downloaded from https://advanced.onlinelibrary.wiley.com/doi/10.1002/aenm.71073 by Jilin University, Wiley Online Library on [07/11/2026]. See the Terms and Conditions (https://onlinelibrary.wiley.com/terms-and-conditions) on Wiley Online Library for rules of use; OA articles are governed by the applicable Creative Commons License

content typically correlates with an increased specific capacity. To maximize the energy density, research has focused on further increasing the Ni content while reducing the proportion of Co to lower the material cost and environmental impact. For instance, in 2017, Sun et al. synthesized $LiNi_{0.9}Co_{0.05}Mn_{0.05}O_2$ (NCM90) [27], which demonstrated a high discharge capacity of 227 mAh g^{-1}. Subsequently, high-Ni layered cathodes such as $LiNi_{0.9}Mn_{0.05}O_2$ (NM90) and $LiNi_{0.9}Co_{0.1}O_2$ (NC90) were also reported in 2019. Nevertheless, increasing the Ni content also introduces several critical challenges that hinder the practical application of Ni-rich ternary cathodes in high-energy systems. On the one hand, a higher Ni content often leads to reduced structural and surface stability, resulting in pronounced capacity fading during cycling. On the other hand, these materials suffer from diminished thermal stability and increased reactivity with moisture, which can cause surface degradation and safety risks. Together, these issues limit the widespread use of high-Ni ternary cathodes and underscore the need for further research into surface stabilization, structural optimization, and interface engineering.

Increasing the Ni content in layered NCM cathodes or raising the upper cutoff voltage is an effective strategy to achieve higher reversible capacities and energy densities, as more Li^+ ions can be extracted during charging. However, higher Ni content inevitably brings critical drawbacks that severely constrain their practical application in HVLIBs. These drawbacks primarily include a significant decline in structural and surface stability, leading to rapid capacity fading, as well as degraded thermal stability and increased surface reactivity, which make high-Ni materials prone to moisture uptake and parasitic reactions.

2.1.4 | Cation Mixing

Cation mixing is a key structural issue for high-Ni cathodes in Figure 2g. Due to the similar ionic radii of Ni^{2+} (0.69 Å) and Li^+ (0.76 Å), a fraction of Ni^{2+} ions can migrate into the Li layers during high-temperature synthesis, resulting in undesired Ni/Li cation mixing [28]. Beyond the size effect, the driving force for cation mixing also includes magnetic interactions within the transition metal layer, where unpaired d-electrons of Ni^{2+} and Ni^{3+} form a superexchange network via oxygen ions, which thermodynamically favors the migration of Ni^{2+} to Li sites. Notably, the migration barrier of Ni^{2+} into Li vacancies decreases as delithiation proceeds, so Ni/Li cation mixing can intensify during cycling, especially with the generation of oxygen vacancies. This cation disordering significantly impedes Li^+ diffusion by reducing the interlayer spacing and blocking Li diffusion pathways, as Ni^{2+} occupying the Li layer becomes electrochemically inactive or undergoes further oxidation to Ni^{3+}, further shrinking the diffusion channels. Severe Ni/Li mixing can thus trigger irreversible phase transformations from the desired layered structure to spinel or rock-salt phases, where Li^+ in octahedral sites loses electrochemical activity, drastically reducing capacity [29]. On the other hand, moderate cation mixing may partially stabilize the structure by restricting transition metal migration and mitigating structural collapse during repeated cycling. Recent studies have shown that intentionally introducing a cation-mixed surface layer can enhance cycling stability at elevated temperatures by buffering lattice expansion and contraction [16].

2.1.5 | Structural Phase Transitions and Microcracking

Structural phase transitions and microcracking are additional challenges for high-Ni layered cathodes. These materials typically crystallize in the $R\bar{3}m$ space group with alternating TMO_6 and LiO_6 layers stacked in an O3-type sequence (Figure 2h) [17]. During deep delithiation, Li vacancies and Jahn-Teller distortions can drive the transformation of the ordered O3 structure to a monoclinic phase ($C2/m$), often referred to as the O′3 phase. Further delithiation can induce an O1 phase with an ABAB oxygen stacking sequence (P–3m1 space group). Mixed H1-3 phases are also frequently observed during the de/lithiation process [30–32]. For example, the phase transition sequence for $LiNiO_2$ is typically described as H1-M-H2-H3, where the transitions correspond to structural changes that affect Li^+ mobility. As delithiation progresses, the c-axis expands due to increased Coulombic repulsion, creating larger Li diffusion pathways; however, at higher states of charge, this expansion reverses, and the c-axis contracts sharply, hindering Li^+ transport [33]. This repeated phase transformation not only degrades Li^+ diffusion kinetics but also leads to significant volume fluctuations, generating substantial internal stresses within primary particles.

In practical high-Ni NCM cathodes, the secondary particles are spherical agglomerates of anisotropic primary particles. The anisotropic lattice expansion and contraction during cycling result in tensile and shear stress accumulation along grain boundaries, eventually forming microcracks. These cracks disrupt the electronic conductivity and expose fresh surfaces to the electrolyte, accelerating interfacial side reactions, increasing cathode-electrolyte interphase growth, and promoting irreversible phase transformations. This crack-induced degradation severely undermines cycling stability and is a major bottleneck for the practical application of high-Ni layered cathodes in next-generation high-energy-density LIBs [3, 34–37].

2.2 | Electrolyte Compatibility Under High Voltage

With the push toward higher energy densities, raising the operating voltage of cathode materials has become an effective strategy for next-generation lithium-ion batteries. However, this is often restricted by the oxidative decomposition of conventional electrolytes and their undesirable chemical interactions with the cathode surface at elevated voltages, which can accelerate cell degradation and failure. As a result, the electrolyte remains one of the critical bottlenecks for HVLIBs. Understanding the fundamental mechanisms and failure pathways of electrolyte behavior under high-voltage conditions and developing electrolytes with improved oxidative stability and safety are therefore essential for the practical advancement of HVLIBs.

To evaluate the electrochemical stability of electrolytes, a commonly used quantitative parameter is the electrochemical stability window (ESW), defined as the energy difference between the lowest unoccupied molecular orbital (LUMO) and the highest

16146840, 2026, 26, Downloaded from https://advanced.onlinelibrary.wiley.com/doi/10.1002/aenm.71073 by Jilin University, Wiley Online Library on [07/11/2026]. See the Terms and Conditions (https://onlinelibrary.wiley.com/terms-and-conditions) on Wiley Online Library for rules of use; OA articles are governed by the applicable Creative Commons License

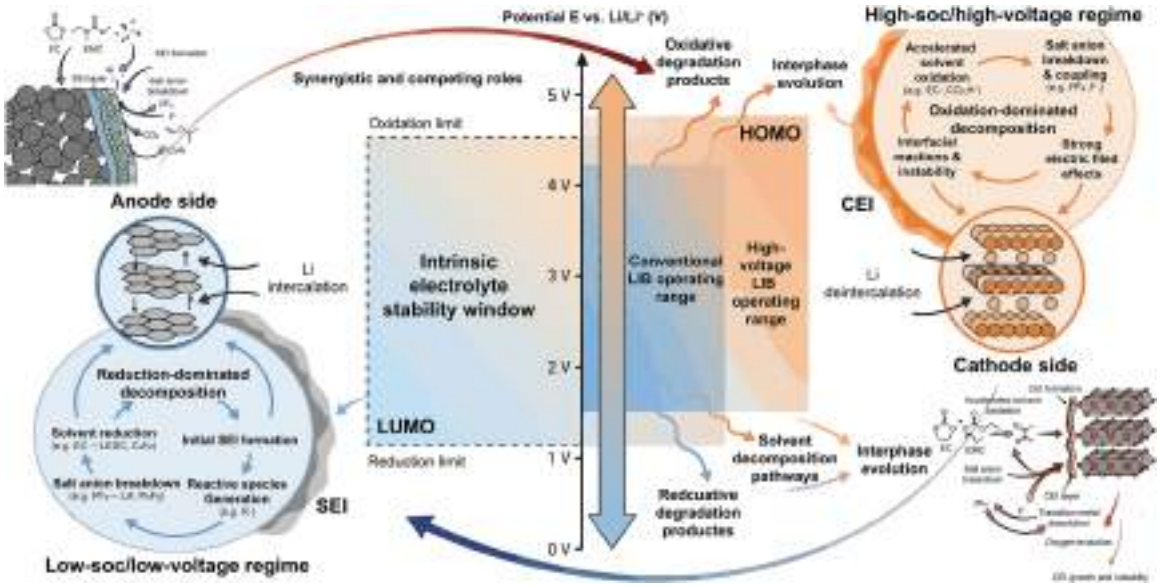


FIGURE 3 | Schematic diagram of the electrochemical instability of electrolytes under high voltage.

occupied molecular orbital (HOMO) (Figure 3). In general, the HOMO and LUMO levels of "Li^+–solvent" clusters are lower than those of isolated solvent molecules, while those of "anion–solvent" clusters are typically higher. As a result, researchers often consider the "anion–solvent" cluster with the highest HOMO level and the "Li^+–solvent" cluster with the lowest LUMO level as the most redox-active components in the electrolyte. These clusters are thus used to evaluate the electrochemical stability of the electrolyte [38, 39]. Specifically, if the HOMO level of the electrolyte exceeds the Fermi level of the cathode surface, the electrolyte is prone to oxidative decomposition. Conversely, if the LUMO level of the electrolyte is lower than the Fermi level of the anode surface, reductive decomposition is likely to occur. This framework provides a theoretical basis for predicting the redox stability of complex electrolyte systems based on molecular orbital energies.

However, in commercial electrolytes, the presence of salts, solvent coordination structures, and interactions between electrode materials and solvent molecules can significantly influence the ESW, often resulting in substantial deviations from theoretical predictions. Zhang et al. employed density functional theory (DFT) to calculate the redox potentials of conventional electrolyte solvents and determined their oxidation sequence to be diethyl carbonate (DEC) > ethyl methyl carbonate (EMC) > dimethyl carbonate (DMC) > ethylene carbonate (EC), indicating that EC has the highest oxidative stability [40]. Nevertheless, the absolute values of the calculated oxidation thermodynamic potentials showed considerable uncertainty, even exceeding experimental values by more than 1 V. This discrepancy arises because oxidation potentials derived solely from HOMO energies represent the behavior of isolated molecules in vacuum, whereas in practical electrolytes, solvent molecules are not isolated but instead interact strongly with lithium salts. These interactions lead to the formation of solvated complexes that participate directly in electron transfer processes during battery operation.

Furthermore, the dielectric constant of the solvent also affects its oxidative stability. For instance, EC, which has a high dielectric constant, tends to form strong complexes with hexafluorophosphate anions (PF_6^-). Under an applied electric field, these complexes migrate toward the cathode surface and undergo preferential oxidation. This behavior further contributes to the discrepancy between theoretical predictions and experimental results, emphasizing the necessity of including lithium salt effects in computational models. Xing et al. demonstrated that while the oxidation voltage of pure EC can reach up to 6.96 V, it rapidly drops below 5 V when adding PF_6^- or ClO_4^- anions, highlighting the critical impact of salt–solvent interactions on the overall oxidative stability of electrolyte systems [41].

Dehydrogenation reactions in electrolytes primarily refer to the hydrogen abstraction processes occurring at the electrode-electrolyte interface, which become particularly pronounced under extreme conditions such as high voltage or elevated temperature. These reactions not only deteriorate the cycling stability and battery safety but also result in gas generation and interfacial instability. As illustrated in Figure 3c, at low voltages (SOC < 80%), the EC component in conventional commercial electrolytes undergoes dehydrogenation at the cathode surface to form VC without generating gaseous byproducts. However, at high voltages (SOC > 80%), singlet oxygen ($^1O_2$) is released from $LiCoO_2$ electrodes and then chemically oxidizes EC molecules, leading to the formation of H_2O, CO_2, and CO. This is primarily due to the catalytic role of surface transition metal ions at low voltages, which lowers the energy barrier for electrolyte side reactions via direct interactions with solvent molecules. As a result, a stable cathode-electrolyte interface (CEI) cannot form under high-voltage conditions, and EC decomposition can initiate even at relatively low potentials. Moreover, the generated H^+ may bind with oxygen atoms in the cathode lattice to form −OH groups or be inserted into interlayer spaces of the cathode material [42].

16146840, 2026, 26, Downloaded from https://advanced.onlinelibrary.wiley.com/doi/10.1002/aenm.71073 by Jilin University, Wiley Online Library on [07/11/2026]. See the Terms and Conditions (https://onlinelibrary.wiley.com/terms-and-conditions) on Wiley Online Library for rules of use; OA articles are governed by the applicable Creative Commons License

With elevated voltages, electrolyte decomposition will be accelerated, producing gaseous byproducts such as CO_2 and CO, which are typically released at a molar ratio of ~3:1 or 4:1. Gasteiger and coworkers demonstrated that singlet oxygen ($^1O_2$) released from the transition metal oxide cathode can directly electrophilically attack the $-CH_2-$ groups in EC via an insertion mechanism, forming hydroxy groups [43]. These unstable intermediates subsequently decompose into carbonyl compounds and water. Further reactions between these intermediates and $^1O_2$ generate CO_2 and CO. Additionally, $^1O_2$ can react with EC to produce VC and hydrogen peroxide (H_2O_2), further exacerbating electrolyte degradation and accelerating battery performance decay. Linear carbonate solvents such as dimethyl carbonate (DMC) also undergo hydrolysis under high-voltage conditions, generating lithium methyl carbonate, methanol, and lithium carbonate [44]. These products may migrate to the anode and decompose further (causing cross-talk effects) or undergo further oxidation at the cathode to generate H_2O [45]. However, recent studies indicate that singlet oxygen may not be the primary driver of electrolyte oxidation under practical high-voltage conditions [46]. Instead, chemical oxidation reactions occurring directly at the surface of Ni-rich layered oxide cathodes are more likely responsible. Highly oxidized surface transition-metal sites and transient, strongly oxidizing intermediates (e.g., peroxo- or oxygen-centered radical species) can directly oxidize carbonate solvents at the solid–liquid interface. This suggests that the dominant parasitic reactions are interfacial in nature rather than gas-phase reactions involving freely diffusing $^1O_2$, providing a more consistent explanation for the strong dependence of electrolyte degradation on cathode surface chemistry and reconstruction.

The lithium salt component PF_6^- is also susceptible to hydrolysis, producing HF and organophosphates. HF would corrode the cathode surface, increase interfacial impedance, and contribute to capacity fade. Furthermore, Musgrave et al. proposed that when EC is adsorbed on the cathode surface, PF_6^- can facilitate ring-opening reactions of EC via coordination, leading to the formation of HF and PF_5. PF_5 can then catalyze further EC decomposition, generating CO_2 and organic carbonate oligomers [47]. Under high-voltage operation, carbonate-based solvents such as EC and EMC are prone to dehydrogenation on the surfaces of high-nickel cathode materials (e.g., NCM811) [43, 48]. This leads to the formation of dehydrogenated products, such as VC and oligomers, which may deposit on the cathode surface, forming inert interfacial layers. These layers can increase charge-transfer resistance and negatively affect battery performance.

2.3 | Interfacial Issues at the Electrode/Electrolyte Interface

For lithium-ion battery cathodes, the surface and interfacial regions of active materials are directly exposed to the electrolyte and conductive carbon, enabling ion transport and electron conduction. However, these interfaces are also sites for surface structural transitions and undesirable side reactions with liquid electrolytes, leading to the accumulation of reaction byproducts and inactive phases, which increase charge transfer resistance and reduce discharge capacity. In the case of high-nickel layered cathode materials, the high oxidative reactivity of Ni^{4+} ions and the ease of Mn^{2+} dissolution, combined with intrinsic structural and surface instabilities under high voltage, inevitably trigger surface reconstruction, transition metal dissolution, byproduct accumulation, and oxygen evolution. This section classifies and discusses these interfacial degradation mechanisms, emphasizing that they often occur synergistically rather than independently.

2.3.1 | Surface Structural Transitions

During repeated cycling, the surface of layered cathode materials tends to transform into spinel-like or rock-salt phases, which severely impede Li^+ and electron transport, resulting in increased interfacial resistance and rapid capacity fade. The structural stability of layered cathodes strongly depends on the upper cutoff voltage. When charged to higher voltages, Ni^{2+} ions in the lattice can migrate due to their ionic radius being similar to that of Li^+, occupying Li sites and driving irreversible structural transitions toward spinel ($Fd\bar{3}m$) and rock-salt (NiO) phases [49, 50]. The formation of this insulating rock-salt layer significantly hinders electrode kinetics, accelerating capacity decay (Figure 4a). Sung et al. demonstrated that the irreversible phase transition on high-Ni cathode surfaces correlates with the charging voltage: below 4.5 V, surface structures can convert to spinel or rock-salt phases, whereas above 4.7 V, increased oxidation states promote lattice oxygen release, further driving structural degradation toward rock-salt phases [51]. Moreover, lattice oxygen release is a key contributor to surface structure instability, not only at extreme voltages but also within the H^2–H^3 phase transition range (>4.2 V). In this regime, the Fermi level shifts from the $Ni_3d_e_{2g}$ band to the top of the O_2p band, activating lattice O^{2-} ions. The surface-active oxygen readily escapes from the lattice, undermining the reversibility and stability of the H^3 phase and kinetically promoting phase transitions [52–54].

2.3.2 | Surface Side Reactions

During high-temperature synthesis, lithium volatilization often leads to a lithium deficiency in the bulk, so excess lithium is typically added to the precursors. This practice can leave residual lithium compounds on the surface of high-Ni cathodes [59]. These residuals react with electrolytes to form insulating layers, while highly oxidative Ni^{4+} further exacerbates electrolyte decomposition, consuming the electrolyte and producing a thick, resistive CEI. In fact, performance degradation often originates at the surface: beyond irreversible phase transitions, the chemical state and surface reactivity with the electrolyte are major limiting factors. When exposed to air, lithium-containing impurities can react with moisture and CO_2 to form Li_2CO_3 and other basic species, increasing the surface alkalinity [60–62]. Residual Li_2CO_3 and LiOH may induce gelation during slurry mixing with binders, causing poor electrode coating uniformity and adhesion. More critically, these surface impurities can be corroded by acidic species in the electrolyte, causing local structural collapse. Such reactions can also generate harmful and flammable gases (CO_2 and alkanes) [63]. The fragile surface of high-Ni materials further reacts with liquid electrolytes (Figure 4b), forming diverse compounds depending on the type of lithium salt and carbonate solvents used. For example, $LiClO_4$-based electrolytes mainly generate carbonate species, whereas $LiPF_6$-based systems

16146840, 2026, 26, Downloaded from https://advanced.onlinelibrary.wiley.com/doi/10.1002/aenm.71073 by Jilin University, Wiley Online Library on [07/11/2026]. See the Terms and Conditions (https://onlinelibrary.wiley.com/terms-and-conditions) on Wiley Online Library for rules of use; OA articles are governed by the applicable Creative Commons License

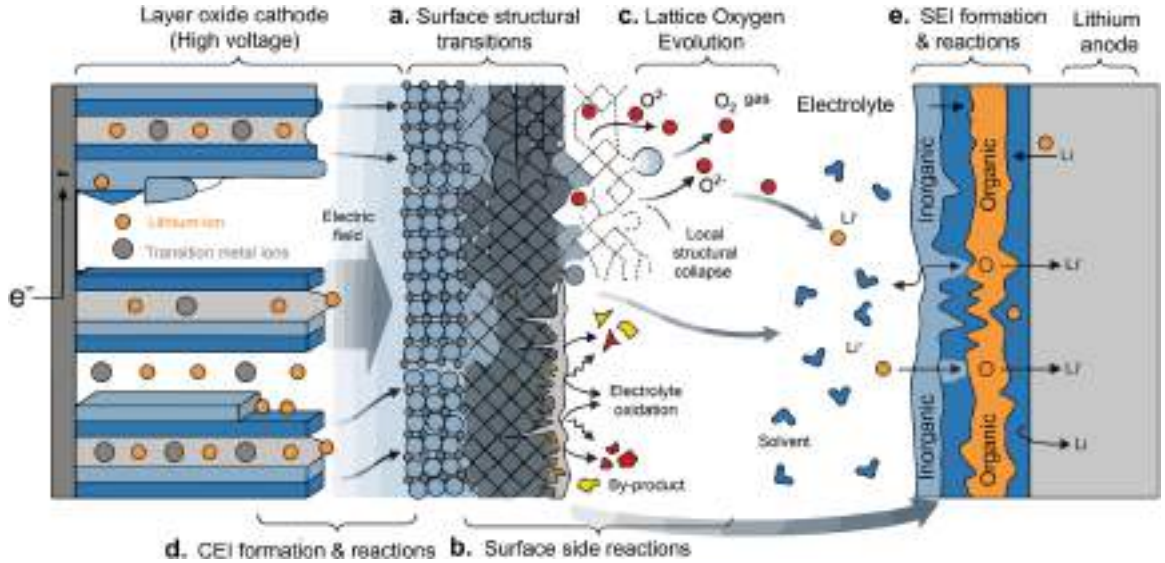


FIGURE 4 | (a) Surface structural transitions [49]. (b) Surface side reactions and composition of cathode materials [55]. (c) Schematic diagram of lattice oxygen evolution [56]. (d) Schematic diagram of unstable CEI and corresponding reaction species [57]. (e) The formation and reactions of SEI for Li^+ transport kinetics performance [58].

produce LiF and $Li_xPF_yO_z$ compounds. These side-products, including LiOH, Li_2CO_3, and P/O/F species such as LiF, Li_xPF_y, and $Li_xPF_yO_z$, not only block Li^+ transport but also continue consuming the electrolyte over long-term cycling, further increasing interfacial resistance and compromising electrochemical performance.

2.3.3 | Lattice Oxygen Evolution

Raising the charging voltage activates lattice oxygen, which participates in redox reactions, leading to oxygen loss. The onset potential for oxygen evolution strongly depends on the Ni content: for $LiNi_{1/3}Co_{1/3}Mn_{1/3}O_2$, oxygen release starts at approximately 4.6 V, while for $LiNi_{0.8}Co_{0.1}Mn_{0.1}O_2$, it begins near 4.2 V. At elevated potentials, the Fermi level shifts from the Ni_3d_e_{2g} band to the O 2p band, activating O^{2-} ions that can escape as O_2 gas or react with carbonate solvents to form CO_2, intensifying cathode-electrolyte interfacial side reactions. The loss of lattice oxygen destabilizes the H3 phase, promotes irreversible transitions to spinel or rock-salt phases, and reduces the oxidation state of transition metals [48]. In Figure 4c, Lim et al. confirmed this mechanism by correlating structural evolution with gas evolution during thermal decomposition, detecting both O_2 and CO_2 emissions [56].

Compared with the compact and well-formed SEI on the anode, the CEI is typically incomplete and insufficient to prevent direct contact between the cathode active material and the electrolyte. This results in the continuous and gradual oxidative decomposition of the electrolyte during subsequent charge/discharge cycles, especially under high-voltage operation in batteries, a phenomenon known as parasitic oxidation [64, 65]. Parasitic oxidation persistently consumes active lithium, leading to rapid capacity fading. Additionally, the accumulation of reaction byproducts on the cathode surface increases the interfacial resistance and triggers a variety of side reactions. Throughout this process, a range of complex organic and inorganic deposits, along with gaseous products, accumulate on the cathode surface. As illustrated in Figure 4d, the interfacial species include carbonates, polycarbonates, alcohols, oxides, ethers, LiF, Li_2CO_3, $Li_xPO_yF_z$, and RCF_x [66–68]. Although these components are chemically similar to those found in SEI and exhibit comparable thicknesses (~3 nm), the structural and chemical properties of CEI differ significantly from those of SEI. Parasitic oxidation is also accompanied by gas evolution, including CO_2, CO, O_2, H_2, and CH_4. These gases can adsorb onto the cathode surface, hindering lithium-ion transport and leading to increased internal pressure. Researchers have found that the severity of parasitic reactions and the volume of gas generation increase with rising voltage [69]. The cumulative effect of all parasitic processes within the battery, including electrolyte oxidation, SEI formation, and repair, ultimately contributes to accelerated degradation and shortened battery lifespan. Parasitic heat flow offers a valuable diagnostic tool to quantify the extent and rate of parasitic reactions occurring within the battery and serves as a predictive indicator of battery life. Smith et al. reported that in full cells with graphite anodes, the parasitic current is largely independent of the applied current [70]. Therefore, under conditions where heat flows associated with polarization and entropy change can be neglected, controlled-current calorimetric measurements can be used to isolate and quantify net heat generation. The observed heat flow differences in such scenarios can be attributed to parasitic heat.

Although the SEI formed on the anode side in HVLIB systems is generally considered less critical than the CEI for maintaining stability under high-voltage operation, its role remains indispensable. To enable stable electrochemical performance above 4.3 V (vs. Li^+/Li), significant efforts have been made to develop EC-free electrolyte systems, such as high-concentrated electrolytes [71], localized high-concentration electrolytes (LHCEs) [72], and fluorinated electrolytes [73]. The improved performance observed with these advanced electrolyte formulations is

16146840, 2026, 26, Downloaded from https://advanced.onlinelibrary.wiley.com/doi/10.1002/aenm.71073 by Jilin University, Wiley Online Library on [07/11/2026]. See the Terms and Conditions (https://onlinelibrary.wiley.com/terms-and-conditions) on Wiley Online Library for rules of use; OA articles are governed by the applicable Creative Commons License

primarily attributed to the formation of robust CEI layers that effectively suppress electrolyte decomposition at the cathode interface. This strategy is conceptually similar to the use of film-forming additives (e.g., VC and triallyl phosphate) in EC-free systems. However, the molecular-scale interactions among Li^+ ions, anions, and solvents at the electrode/electrolyte interface remain poorly understood. These interactions critically influence Li^+ transport kinetics, electrolyte electrochemical stability, and overall electrode performance (Figure 4e). The lack of comprehensive insight into these mechanisms, especially when the focus is solely on cathode-side stabilization, has inadvertently led to new challenges on the anode side. For instance, it has been reported that EC-free electrolytes can induce serious side effects, including compromised cycling stability and safety risks in LIBs. In particular, the absence of EC may result in uncontrolled lithium plating on graphite anodes during fast charging or high-rate cycling, raising significant safety concerns. Therefore, a deeper molecular-level understanding of interfacial behaviors and reaction mechanisms at both cathode and anode surfaces is essential for the rational design of next-generation electrolytes tailored for high-voltage lithium-ion batteries.

2.4 | Challenges in Solid-State Batteries

The pursuit of high-voltage operation in conventional liquid electrolyte systems is fundamentally constrained by oxidative decomposition, parasitic side reactions, and interfacial instability at elevated potentials. These intrinsic limitations not only accelerate electrolyte degradation but also induce gas evolution, impedance growth, and rapid capacity fading. In this context, solid-state batteries (SSBs) have emerged not merely as an alternative for higher energy density but also as a fundamentally different strategy to address the core instability of liquid electrolytes under high-voltage conditions. By replacing flammable liquid electrolytes with solid-state electrolytes (SSEs), SSBs effectively suppress solvent oxidation and mitigate interfacial side reactions, thereby enabling compatibility with high-voltage cathodes and lithium metal anodes [74–76]. The latter offers an ultrahigh theoretical capacity (3860 mAh g^{-1}) and low redox potential (–3.04 V vs. SHE), opening a pathway toward energy densities exceeding 500 Wh kg^{-1}. More importantly, the nonflammable, nonvolatile nature, together with the high thermal stability and mechanical rigidity of SSEs, provides intrinsic resistance against thermal runaway and dendrite penetration, directly addressing safety concerns exacerbated under high-voltage operation (Figure 5a) [77–79].

Depending on the electrolyte chemistry, SSBs can be broadly categorized into polymer-, oxide-, and sulfide-based systems, each exhibiting distinct trade-offs in ionic conductivity, electrochemical stability, processability, and environmental sensitivity (Figure 5b) [80]. From a high-voltage perspective, the key requirement for SSEs lies in sustaining a wide electrochemical stability window (typically 2–5.0 V vs. Li^+/Li) while maintaining stable electrode/electrolyte interfaces. Accordingly, significant efforts have been devoted to developing SSEs capable of withstanding high oxidative potentials, as summarized in Table 1.

Among these, inorganic SSEs have attracted particular attention due to their superior oxidative stability compared to liquid electrolytes. However, a critical discrepancy exists between theoretically predicted and experimentally observed electrochemical stability windows. For instance, density functional theory (DFT) calculations suggest relatively narrow stability windows for representative materials such as LGPS (1.71–2.15 V), LLTO (1.75–3.71 V), LLZO (0.05–2.91 V), LATP (2.16–4.31 V), and LAGP (2.70–4.27 V) [95], whereas experimental measurements often report apparently wider windows. This inconsistency is largely attributed to the use of inert electrodes in half-cell configurations, which underestimate realistic interfacial reactivity. In practical full-cell systems, direct contact between SSEs and high-voltage cathodes frequently induces interfacial decomposition. For instance, at ~3.8 V, the LLZO/LNMO interface undergoes continuous degradation, leading to a cathode surface phase transition and the formation of $Li_{0.35}Ni_{0.05}NiO_2$, which increases the interfacial resistance and ultimately causes battery failure [96].

Sulfide-based SSEs, often considered promising due to their high ionic conductivity and nominally wide stability window (0 to 5 V vs. Li^+/Li) [97], still suffer from pronounced interfacial instability under high-voltage operation. Oxidative decomposition above ~3.8 V generates sulfur species and other byproducts, increasing interfacial resistance and reducing Coulombic efficiency, particularly when paired with 4 V-class layered cathodes. Notably, such instability is highly interface-dependent and can be mitigated through interfacial engineering. For instance, surface sulfuration of LNMO effectively stabilizes the interface, enabling sulfide electrolytes to operate under 5 V conditions (Figure 5c). Nevertheless, sulfide SSEs also face critical practical challenges, including severe moisture sensitivity and toxic H_2S gas release, necessitating stringent processing conditions.

To overcome these limitations, emerging inorganic SSEs, particularly halide-based systems, have demonstrated improved compatibility with high-voltage cathodes. For example, $Li_2In_{1/3}Sc_{1/3}Cl_4$ exhibits stable operation up to 4.8 V with excellent cycling durability [82] (Figure 5d). Similarly, ytterbium-based halide electrolytes show good compatibility with 4 V-class cathodes such as LCO and Ni-rich NCM without requiring surface coatings [98]. Interface engineering strategies, such as vacuum-assisted deposition of Li_3InCl_6 interlayers [99, 100], further enhance interfacial stability and enable sustained high-voltage cycling. These findings highlight that the practical electrochemical stability of SSEs is governed not only by bulk thermodynamics but also by dynamic interfacial reactions under realistic operating conditions, emphasizing the necessity of full-cell-level evaluation.

Despite their intrinsic advantages in suppressing high-voltage-induced side reactions and improving safety, SSBs still face several critical challenges that hinder their practical implementation (Figure 5e) [83]. Lithium dendrite penetration through solid electrolytes remains a major concern, particularly under high current densities. In addition, interfacial instability at the Li metal/SSE interface, including nonuniform SEI formation, leads to increased resistance and reduced cycling stability. Mechanical degradation induced by volume changes during cycling further exacerbates interfacial failure. These challenges underscore that although SSBs provide a promising pathway to fundamentally overcome the limitations of liquid systems under high

16146840, 2026, 26, Downloaded from https://advanced.onlinelibrary.wiley.com/doi/10.1002/aenm.71073 by Jilin University, Wiley Online Library on [07/11/2026]. See the Terms and Conditions (https://onlinelibrary.wiley.com/terms-and-conditions) on Wiley Online Library for rules of use; OA articles are governed by the applicable Creative Commons License

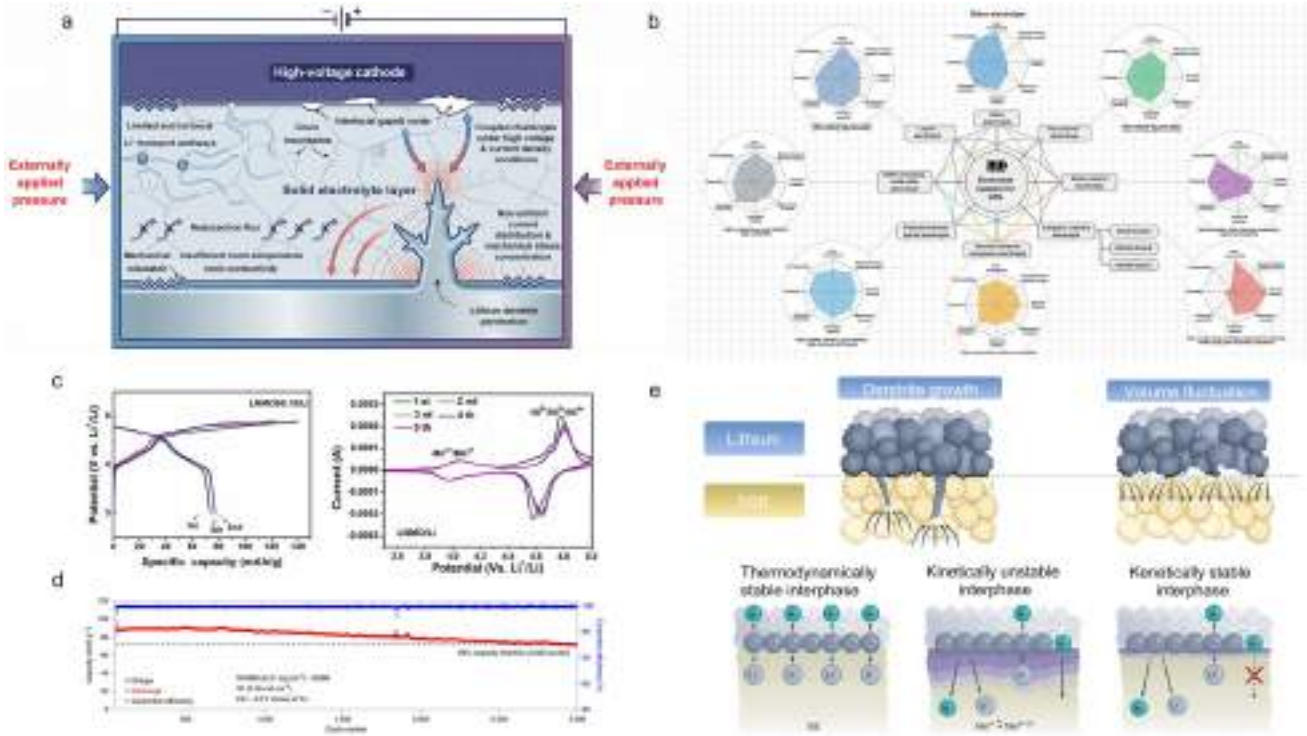


FIGURE 5 | (a) Schematic diagram of a solid-state electrolyte matching a high-voltage cathode and a lithium metal anode. (b) Distinguished properties of various electrolytes [80]. (c) Electrochemical stability under 5 V operation after surface sulfuration of LNMO [81]. Copyright, Elsevier. (d) Long-term and high-voltage electrochemical performance of $Li_2In_{1/3}Sc_{1/3}Cl_4$ [82]. Copyright, Springer Nature. (e) Critical issues between lithium metal anodes and SSEs [83]. Copyright, Springer Nature.

TABLE 1 | Advanced high-voltage SSEs and battery performance of high-voltage ASSLMBs.

SSE	Conductivity (S cm^{-1})	ESW	Cell constitution	Cell voltage window	Cycle performance	Refs.
$Li_{2.75}Y_{0.16}Er_{0.16}Yb_{0.16}In_{0.25}Zr_{0.25}Cl_6$	1.17×10^{-3}	4.6 V	Li-In|LCO	2.5–4.6 V	91.6%@50 cycles	[84]
$Li_{2.2}In_{0.2}Sc_{0.2}Zr_{0.2}Hf_{0.2}Ta_{0.2}Cl_6$	4.69×10^{-3}	5.2 V	Li-In|NCM	3.0–5.5 V	71.9%@111 cycles	[85]
P(PEGMEA)+BTO	4.16×10^{-5}	4.7 V	Li|NCM811	2.8–4.7 V	64%@500 cycles	[86]
PVDF-HFP+TMP	7.90×10^{-4}	5.2 V	Li|NCM811	2.8–4.7 V	91.5%@300 cycles	[87]
P(TFPO-PEE)	3.98×10^{-3}	5.1 V	Li|NCM622	2.8–4.7 V	74.2%@100 cycles	[88]
PVDF-TrFE+LiDFP	1.91×10^{-3}	5.1 V	Li|LNMO	3.5–5.1 V	60%@200 cycles	[89]
$Li_{2.5}ZrCl_5F_{0.5}O_{0.5}$	1.17×10^{-3}	4.8 V	Li|NCM955	2.5–4.3 V	81.2%@500 cycles	[90]
LLZTO+TEGDME	2.70×10^{-4}	5.2 V	Li|NCM811	2.8–4.5 V	90%@200 cycles	[91]
PLiMTFSI-*b*-PPFEMA	4.45×10^{-4}	5.1 V	Li|LCO	2.8–4.6 V	70%@190 cycles	[92]
PEO-Mg-Al-LiTFSI	2.30×10^{-4}	4.8 V	Li|NCM811	2.8–4.8 V	63.5%@100 cycles	[93]
LPIFD	3.00×10^{-4}	4.5 V	Li|NCM811	2.8–4.5 V	76.2%@450 cycles	[94]

16146840, 2026, 26, Downloaded from https://advanced.onlinelibrary.wiley.com/doi/10.1002/aenm.71073 by Jilin University, Wiley Online Library on [07/11/2026]. See the Terms and Conditions (https://onlinelibrary.wiley.com/terms-and-conditions) on Wiley Online Library for rules of use; OA articles are governed by the applicable Creative Commons License

voltage, their reliable operation still requires deeper mechanistic understanding and advanced interface engineering strategies [101–105].

3 | Advanced Techniques for High-Voltage Degradation Mechanisms

The severe interfacial instability at cathode/electrolyte interfaces under high-voltage conditions (>4.5 V), as discussed above, necessitates a comprehensive understanding of both the chemical and structural evolution occurring during electrochemical operation. In contrast to metal anode interfaces, where reductive decomposition dominates, high-voltage cathode interfaces are primarily governed by oxidative degradation, space-charge layer formation, and transition-metal-driven interfacial reactions [106–108]. Elucidating these processes requires the integration of multimodal characterization techniques across multiple length and time scales, enabling the correlation of interfacial chemistry, structural evolution, and electrochemical behavior.

3.1 | Characterization Techniques for High-Voltage Degradation Mechanisms

For chemical and electrochemical degradation mechanisms, identifying the composition and evolution of cathode/electrolyte interphases is essential to clarify reaction pathways and their impact on Li^+ transport and interfacial resistance. To this end, a combination of advanced spectroscopic and diffraction techniques, including X-ray diffraction (XRD), X-ray photoelectron spectroscopy (XPS), X-ray absorption spectroscopy (XAS), and Raman spectroscopy, has been widely employed. These techniques provide complementary insights into bulk phase transitions, surface chemical states, and local bonding environments under high-voltage operation (Figure 6). In summary, we have provided a comprehensive table presenting the advantages of different characterization techniques for the analysis of high-voltage cathode interface structure and composition in Table 2.

Electron microscopy techniques provide direct visualization of interfacial morphology and microstructural evolution. Scanning electron microscopy (SEM) and transmission electron microscopy (TEM) enable the observation of interfacial contact, crack formation, and morphological degradation, while high-resolution TEM and associated spectroscopic techniques (e.g., EDS, EELS) allow for atomic-scale analysis of interphase formation and elemental redistribution [109]. However, the interaction between high-energy electron beams and sample surfaces can induce damage, potentially altering the structure and composition of sensitive interphases such as the SEI and CEI, thereby leading to misinterpretation of results. To address this limitation, cryogenic electron microscopy (cryo-EM) has been developed to preserve the native structure of samples by rapid freezing at ultralow temperatures. By vitrifying the surrounding liquid environment (e.g., using liquid nitrogen), cryo-EM minimizes the effects of vacuum exposure and electron beam irradiation. For example, cryo-EM analysis has revealed that no continuous CEI layer can be detected on NMC cathode surfaces after 100 cycles, suggesting that CEI formation may be spatially heterogeneous and does not uniformly cover individual particles [110]. Moreover, the thickness of the CEI layers can be quantitatively determined from cryo-EM images, although significant variations are observed depending on the cathode material and electrolyte system [111–113].

Atomic force microscopy (AFM) provides another powerful approach for probing interfacial properties by measuring the intermolecular forces between a probe and the sample surface. In particular, AFM-based modulus mapping offers valuable information on the composition and mechanical properties of CEI layers. Recent studies have shown that the modulus of the CEI is strongly influenced by the cathode chemistry, electrolyte composition, and testing conditions [114–116]. Generally, CEI layers with higher inorganic content and more uniform distribution exhibit larger modulus values and improved interfacial stability. Notably, AFM can be readily integrated into in situ electrochemical methods, enabling direct observation of CEI formation and evolution during battery operation. For instance, Chen et al. [117] investigated the behavior of $LiCoO_2$ at high voltages and found that while the bulk crystal facets remained largely unchanged during charging, a thin film with a fibrous morphology formed at particle edges at 4.5 V and disappeared upon discharging to 3 V. AFM analysis further revealed the formation of surface microcracks and slip steps under different states of charge, providing critical insights into the dynamic structural evolution of cathode materials during cycling.

For chemical characterization, synchrotron-based X-ray techniques play a central role in probing high-voltage degradation. Operando XRD enables real-time tracking of cathode structural evolution, such as phase transitions from layered to rock-salt or spinel-like structures induced by deep delithiation and oxygen release. However, such bulk-sensitive techniques often lack sufficient resolution to directly resolve interfacial reactions. In contrast, X-ray photoelectron spectroscopy (XPS), with its high surface sensitivity, is particularly effective in identifying interfacial decomposition products and electronic structure changes. For example, XPS analysis has revealed the formation of oxidized species such as Li_2CO_3, LiF, and transition-metal-containing compounds at high-voltage interfaces, which originate from electrolyte oxidation and cathode surface reconstruction [118–120]. The sensitivity of XPS to subtle binding energy shifts further enables the detection of changes in electronic structure, providing insights into the alignment of energy levels that govern interfacial stability. In addition, time-of-flight secondary ion mass spectrometry (TOF-SIMS) has emerged as a powerful technique for probing interfacial chemical compositions with high sensitivity. By bombarding the sample surface with primary ions, TOF-SIMS generates secondary ions that carry detailed compositional information. This method is particularly effective for tracking transition metal dissolution from cathodes and their subsequent reactions with electrolyte components at high-voltage interfaces. Characteristic ionic fragments such as MnF_3^-, FeF_2^-, FeF_3^-, MnF_2^-, NiF_3^-, and NiO^- can be readily detected, providing direct evidence of interfacial side reactions and decomposition pathways [6, 7, 121]. Furthermore, TOF-SIMS enables in-depth analysis of the reactivity of different components and their associated reaction pathways, offering valuable insights into the complex chemistry governing high-voltage interfacial degradation [122–125].

16146840, 2026, 26, Downloaded from https://advanced.onlinelibrary.wiley.com/doi/10.1002/aenm.71073 by Jilin University, Wiley Online Library on [07/11/2026]. See the Terms and Conditions (https://onlinelibrary.wiley.com/terms-and-conditions) on Wiley Online Library for rules of use; OA articles are governed by the applicable Creative Commons License

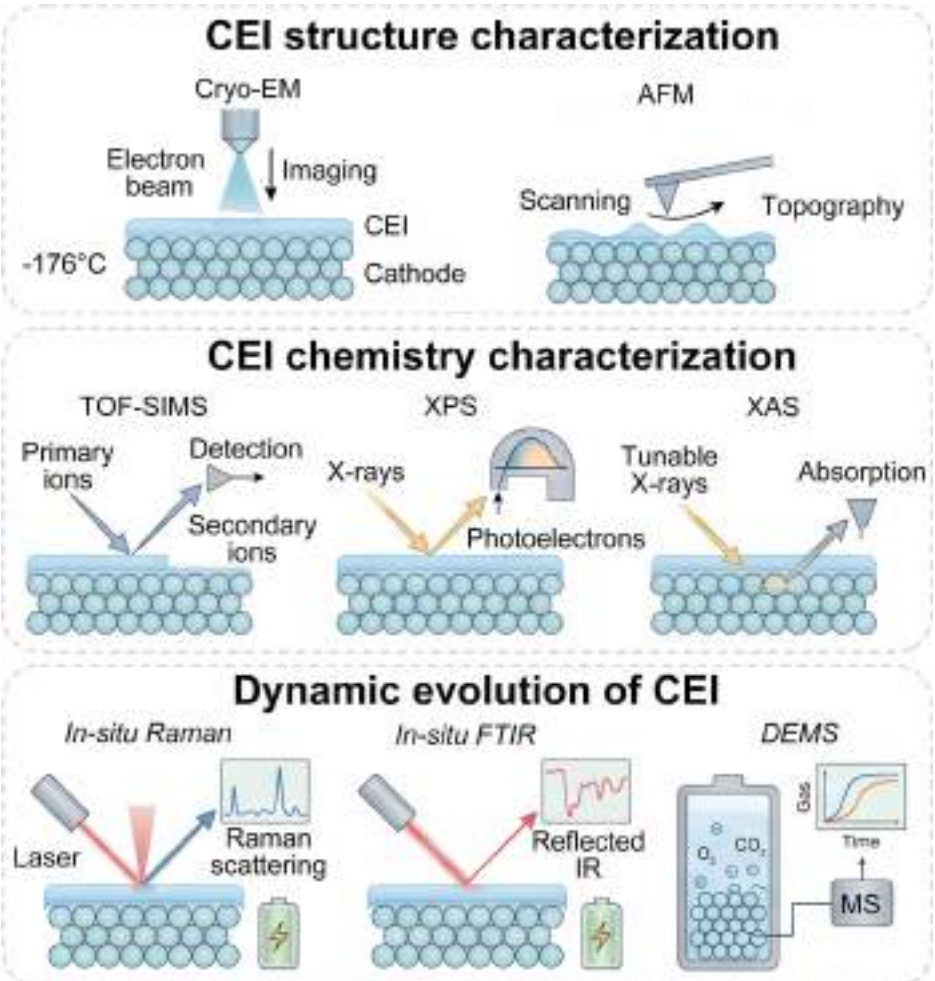


FIGURE 6 | Schematic diagrams illustrating advanced characterization techniques for the high-voltage CEI.

X-ray absorption spectroscopy (XAS), including XANES and EXAFS, offers element-specific information on local coordination environments and oxidation states, making it particularly valuable for tracking transition metal redox behavior and oxygen participation in high-voltage reactions. Operando XAS studies have demonstrated that transition metal migration and oxygen redox activity are closely coupled to interfacial degradation, leading to the formation of disordered surface layers that impede Li^+ transport [126]. Importantly, XAS can distinguish between bulk and interfacial regions, enabling the identification of localized degradation processes that are often undetectable by conventional diffraction techniques [127].

Beyond the monitoring of interfacial morphology and chemical composition, operando techniques for probing dynamic interfacial evolution are equally critical for understanding high-voltage degradation mechanisms. In situ Raman spectroscopy provides detailed insights into the evolution of molecular and crystal structures in cathode materials during electrochemical cycling. As electrochemical reactions proceed, changes in bonding environments and lattice vibrations are reflected in Raman spectra through peak shifts, intensity variations, and the emergence or disappearance of characteristic vibrational modes [128–130]. Notably, Raman spectroscopy is also an effective tool for detecting the formation of O−O bonds and peroxide species in lithium-rich layered oxides, which are closely associated with oxygen redox activity and structural instability at high voltages [131].

In situ Fourier transform infrared (FTIR) spectroscopy offers complementary information on interfacial chemical evolution. For instance, the Liu group employed operando FTIR to monitor the dynamic evolution of the CEI during electrochemical cycling, revealing that CEI instability originates from its reversible transformation during charge/discharge processes. This behavior leads to a continuous "formation-dissolution-reformation" process, driven by ongoing electrolyte consumption, ultimately contributing to interfacial degradation [132].

Differential electrochemical mass spectrometry (DEMS) is another powerful real-time technique that couples electrochemical cells with mass spectrometry to detect gaseous products generated during battery operation. DEMS enables the identification of gas evolution at cathode interfaces, including species originating from electrolyte decomposition and cathode degradation, thereby providing a more comprehensive picture of interfacial reactions [133–135]. For example, Amine et al. employed DEMS and coherent X-ray diffraction to establish a voltage threshold (>4.47 V) for O_2 release in $LiTMO_2$ cathodes, linking lattice expansion and transition metal migration to surface oxygen loss [136].

16146840, 2026, 26, Downloaded from https://advanced.onlinelibrary.wiley.com/doi/10.1002/aenm.71073 by Jilin University, Wiley Online Library on [07/11/2026]. See the Terms and Conditions (https://onlinelibrary.wiley.com/terms-and-conditions) on Wiley Online Library for rules of use; OA articles are governed by the applicable Creative Commons License

TABLE 2 | The advantages of various characterization techniques for high-voltage cathode interface structure and composition analysis.

Characterization information	Technique	Advantages
Structure	SEM	Provides mesoscale morphology and surface features; useful for evaluating electrode integrity and interface evolution after high-voltage cycling
	TEM	Atomic-/nanoscale resolution imaging; enables direct visualization of CEI thickness, crystallinity, and cathode/electrolyte interface structure
	Cryo-EM	Preserves native CEI structure by minimizing beam damage and air exposure; reveals fragile and metastable interphases formed at high voltage
	AFM	High-resolution surface topography and mechanical mapping; capable of probing local stiffness, adhesion, and charge distribution at CEI
Chemistry	XAS	Element-specific probe of oxidation states and local coordination; particularly powerful for tracking transition metal redox and oxygen activity at high voltage
	XPS	Surface-sensitive chemical analysis (~nm depth); provides elemental composition and chemical states of CEI components with high resolution
	TOF-SIMS	Ultrahigh surface sensitivity with spatial mapping; detects light elements and organic/inorganic fragments, enabling detailed CEI compositional profiling
Dynamic evolution	In situ XRD	Monitors real-time structural evolution of cathodes during cycling; correlates phase transitions with CEI formation at high voltage
	In situ FTIR	Tracks molecular-level evolution of electrolyte decomposition products and CEI species during operation
	In situ Raman	Provides real-time insight into structural and chemical changes, including bond evolution and reaction pathways at the cathode interface
	DEMS	Enables real-time, operando detection of gas evolution with high sensitivity; provides direct insight into electrolyte oxidation, cathode oxygen release, and interfacial decomposition processes under high-voltage operation

3.2 | Simulation Techniques for High-Voltage Degradation Mechanisms

The complex degradation processes at high-voltage interfaces, involving coupled electrochemical, chemical, and mechanical phenomena, are often difficult to fully resolve by experiments alone. In this context, computational simulations play a crucial role in providing atomistic to mesoscale insights into interfacial reactions, ion transport, and structural evolution. By bridging multiple length scales, simulation techniques complement advanced characterization and enable a more fundamental understanding of degradation mechanisms under high-voltage conditions (Figure 7).

At the electronic and atomic scales, density functional theory (DFT) has been extensively employed to evaluate the intrinsic stability of solid electrolytes and interfacial materials. In particular, DFT calculations enable the prediction of electrochemical stability windows based on the alignment of electronic energy levels, as well as the identification of likely decomposition pathways at high potentials [137]. For cathode/SSE interfaces, DFT has revealed that many oxide and sulfide electrolytes are thermodynamically unstable above 4.0~4.5 V and undergo oxidative decomposition to form resistive interphases [138]. Importantly, such calculations also provide insights into interfacial reaction energies, charge transfer behavior, and the formation of space-charge layers arising from differences in chemical potential across the interface [95, 139, 140]. However, it is now widely recognized that the practical stability window often exceeds the thermodynamic limit, owing to kinetic barriers that suppress interfacial reactions, highlighting the necessity of coupling DFT with dynamic simulations and experimental validation [141].

To capture the dynamic evolution of interfaces and ion transport processes, molecular dynamics (MD) simulations, including both classical and ab initio approaches, are widely used [142]. MD simulations can provide detailed information on Li^+ diffusion behavior, electrolyte reactions, and the formation of disordered interphases under electrochemical driving forces. In high-voltage systems, MD studies have demonstrated that interfacial instability is closely linked to local structural fluctuations and the breakdown of coordination environments, which facilitate parasitic reactions and impede ion transport [143]. Furthermore, MD simulations are particularly valuable for investigating the formation and evolution of space-charge layers, which play a critical role in determining interfacial resistance and rate capability [144].

At larger length scales, phase-field modeling offers a powerful framework for describing the mesoscale evolution of interfaces during electrochemical cycling. By incorporating thermodynamic and kinetic parameters derived from atomistic calculations, phase-field models can simulate the growth of interfacial layers, crack formation, and chemo-mechanical coupling effects that lead to performance degradation [145–147]. For high-voltage

16146840, 2026, 26, Downloaded from https://advanced.onlinelibrary.wiley.com/doi/10.1002/aenm.71073 by Jilin University, Wiley Online Library on [07/11/2026]. See the Terms and Conditions (https://onlinelibrary.wiley.com/terms-and-conditions) on Wiley Online Library for rules of use; OA articles are governed by the applicable Creative Commons License

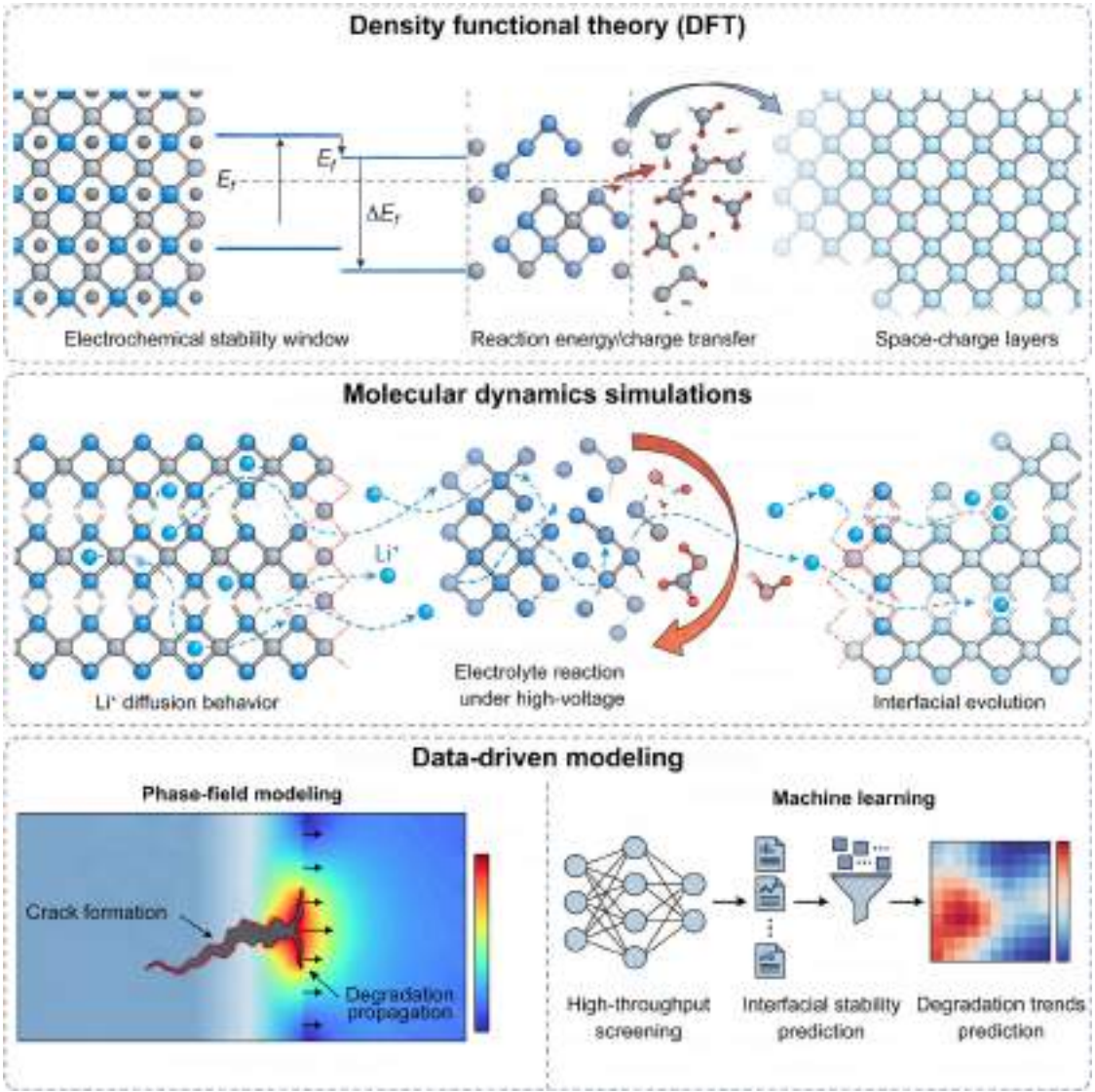


FIGURE 7 | Schematic diagrams illustrating simulation techniques for high-voltage degradation mechanisms.

cathodes, such models have been used to elucidate how interfacial reactions and volume changes induce stress accumulation, ultimately resulting in loss of contact and accelerated degradation [148]. These approaches thus provide a direct link between microscopic mechanisms and macroscopic failure behavior.

More recently, data-driven approaches and machine learning (ML) techniques have emerged as promising tools for accelerating the discovery and optimization of materials for HVLIBs [149–151]. ML-assisted methods enable high-throughput screening of electrolyte and coating materials with enhanced oxidative stability, as well as the development of surrogate models that can predict interfacial properties and degradation trends. In addition, machine learning potentials have been increasingly integrated with molecular dynamics simulations to extend accessible time and length scales while maintaining near first-principles accuracy.

Overall, each simulation and modeling approach discussed above provides distinct yet complementary insights into high-voltage degradation mechanisms. A comprehensive understanding therefore requires the integration of multiscale computational techniques, linking electronic structure calculations with atomistic dynamics and mesoscale evolution. This highlights the importance of developing coupled simulation frameworks that can bridge different length and time scales while maintaining consistency with experimental observations. Furthermore, closer synergy between simulations and advanced characterization techniques is essential for validating predicted reaction pathways and interfacial phenomena under realistic operating conditions. Continued progress in high-throughput computation, machine learning-assisted modeling, and physically informed data-driven approaches will further enhance predictive capabilities, enabling more accurate identification of degradation mechanisms and rational design of stable HVLIBs.

4 | Process–Structure–Performance Relationships in High-Voltage Lithium-Ion Batteries

In HVLIBs, performance is governed not only by material composition but more critically by preparation technologies.

16146840, 2026, 26, Downloaded from https://advanced.onlinelibrary.wiley.com/doi/10.1002/aenm.71073 by Jilin University, Wiley Online Library on [07/11/2026]. See the Terms and Conditions (https://onlinelibrary.wiley.com/terms-and-conditions) on Wiley Online Library for rules of use; OA articles are governed by the applicable Creative Commons License

Fabrication routes directly determine particle crystallinity, defect distribution, surface chemistry, and interfacial structure, which in turn control voltage stability, interfacial degradation, and safety under high-field operation. Therefore, preparation technologies should be viewed as key enablers that bridge material design with battery performance rather than auxiliary steps. This chapter focuses on how specific fabrication strategies regulate structural and interfacial features and how these features ultimately dictate high-voltage performance.

4.1 | Preparation Routes of High-Voltage Electrode Materials and Performance Implications

This section focuses on how preparation strategies translate into specific structural and interfacial features that control electrochemical behavior. Bottom-up approaches primarily define bulk properties such as phase purity, particle size, and defect distribution, which influence Li^+ transport and structural stability under deep delithiation. In contrast, top-down strategies regulate the surface chemistry and interfacial structure, playing a critical role in suppressing electrolyte oxidation and stabilizing cathode/electrolyte interfaces. In practice, these approaches are often combined, enabling the rational design of electrode materials with optimized bulk structure and interfacial stability, which are both essential for reliable operation under high-voltage conditions.

4.1.1 | Synthesis Strategies of High-voltage Electrode Materials: From Atomic to Voltage Stability

The synthesis pathway of high-voltage electrode materials establishes their initial cation ordering, particle morphology, and defect distribution, which collectively dictate lithium-ion transport, structural robustness, and interfacial reactivity under high electric fields.

4.1.1.1 | High-Temperature Solid-State Synthesis: Cation Disorder and High-Voltage Degradation. High-temperature solid-state synthesis is widely used for layered cathode materials due to its simplicity and scalability. However, diffusion-limited kinetics and elevated sintering temperatures inherently induce particle coarsening and Li/Ni cation mixing, both of which are detrimental to structural stability and capacity retention at high voltages. This method typically involves mixing lithium sources (e.g., LiOH, Li_2CO_3) with transition metal precursors, followed by high-temperature calcination (Figure 8a). While it can preserve precursor morphology, the resulting materials often exhibit inhomogeneous particle size distribution and uneven crystallinity, depending on precursor design and processing conditions. Qiu et al. modified solid-state routes with precursors that can improve crystallinity and reduce the Li^+ diffusion length, leading to enhanced capacity and rate performance [152]. Nevertheless, variability in particle morphology and structural integrity remains common, even though capacities above 180 mAh g^{-1} at low rates and reasonable cycling stability have been reported [153–155] (Figure 8b).

A key limitation of this method lies in excessive grain growth during prolonged high-temperature sintering, which often leads to broad or bimodal particle size distributions [159–161]. The Zhang group systematically investigated the impact of sintering temperature on the grain size distribution of cathode particles [156]. As shown in Figure 8c, the particle sizes of NCM811 cathode materials range from ~200 nm to over 100 μm. Such heterogeneity results in poor particle packing and increased porosity in electrodes, disrupting Li^+ transport pathways and promoting interfacial side reactions with the electrolyte. Consequently, both internal transport limitations and external parasitic reactions accelerate capacity fading under high-voltage operation.

In addition, Li/Ni cation disorder is a critical issue in Ni-rich layered oxides (e.g., NCM811), arising from the similar ionic radii of Ni^{2+} and Li^+. During high-temperature synthesis, Ni^{2+} readily occupies Li sites, leading to anti-site defects that significantly degrade electrochemical performance. These defects reduce the Li-layer spacing, hinder Li^+ diffusion via a pinning effect, and introduce electrochemically inactive Li species (Figure 8d) [157]. Furthermore, oxidation of anti-site Ni^{2+} during initial charging induces lattice contraction, contributing to irreversible capacity loss (Figure 8e) [158, 162]. Overall, while solid-state synthesis offers practical advantages, its intrinsic tendency to generate structural heterogeneity and cation disorder limits high-voltage performance, highlighting the need for improved precursor engineering and process optimization.

4.1.1.2 | Coprecipitation: Precursor Engineering for High-Voltage Interfacial Stability. By enabling atomic-level mixing and precise control over precursor morphology, coprecipitation directly influences secondary particle density and surface chemistry, which in turn regulate electrolyte penetration, CEI formation, and voltage-induced degradation during prolonged cycling. Co-precipitation is widely adopted for synthesizing high-voltage layered oxide precursors due to its simplicity, scalability, low cost, and ability to achieve atomic-level mixing of transition metals [163–165]. This method enables precise control over precursor composition, particle morphology, crystal ordering, and impurity levels, all of which critically dictate the electrochemical performance of the final cathode. By tuning co-precipitation conditions, dense and uniform secondary particles can be produced in large batches suitable for industrial applications.

Typically, precursor synthesis involves two stages: (1) continuous feeding of metal salt solutions (e.g., Ni, Co, Mn acetates or sulfates) into an ammoniacal reactor, where metal ions form aqua complexes ($[TM(NH_3)_n]^{2+}$); (2) gradual addition of NaOH to precipitate metal hydroxides, while a dynamic dissolution and recrystallization equilibrium is maintained (Figure 9a). Under controlled pH and ammonia concentrations, nucleation occurs rapidly upon supersaturation, followed by crystallite growth and aggregation into primary particles, which eventually self-assemble into spherical secondary particles by Ostwald ripening (Figure 9b) [166]. Careful modulation of parameters such as pH, ammonia concentration, feed rate, temperature, and stirring conditions allows precise control over both the size and packing morphology of precursor particles.

Even under vigorous stirring, primary particle growth tends to remain anisotropic due to differences in surface energy across crystallographic planes. Yang et al. used DFT to reveal that the

16146840, 2026, 26, Downloaded from https://advanced.onlinelibrary.wiley.com/doi/10.1002/aenm.71073 by Jilin University, Wiley Online Library on [07/11/2026]. See the Terms and Conditions (https://onlinelibrary.wiley.com/terms-and-conditions) on Wiley Online Library for rules of use; OA articles are governed by the applicable Creative Commons License

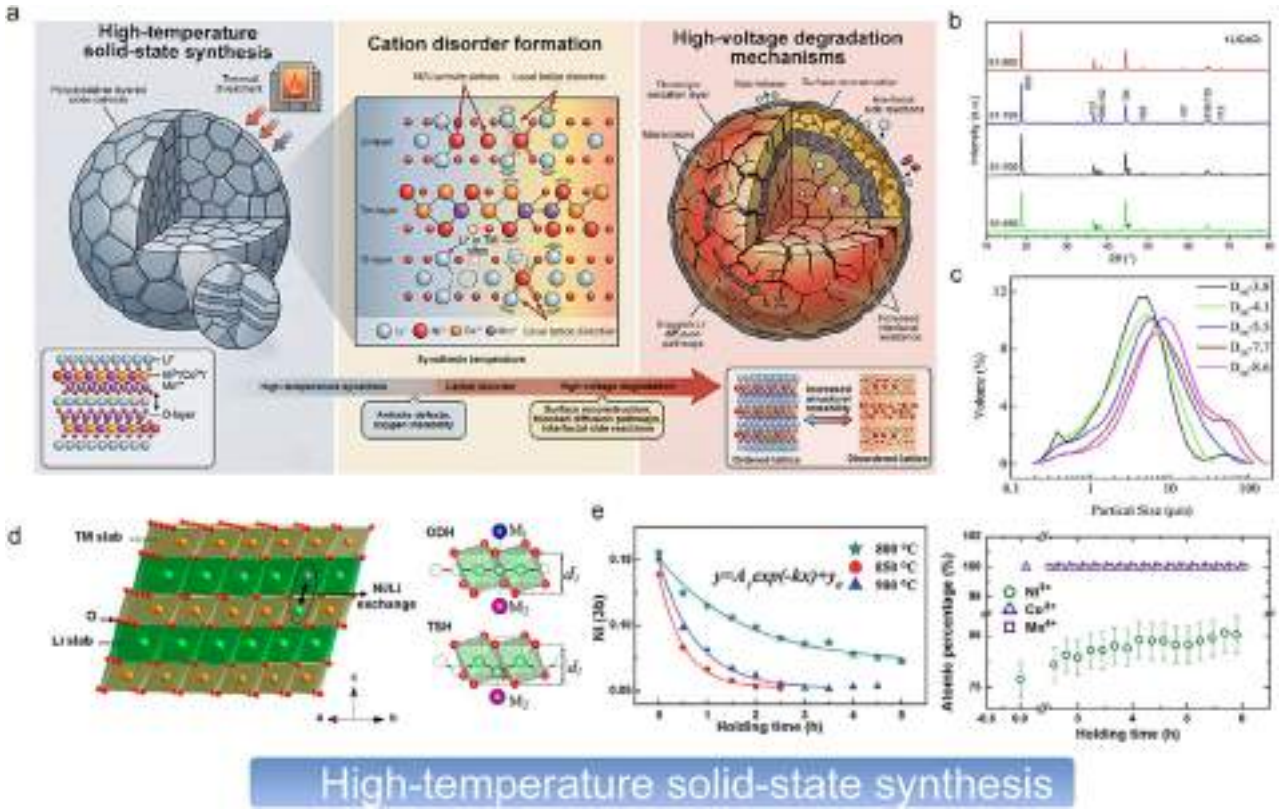


FIGURE 8 | (a) Schematic diagram of high-temperature solid-state synthesis. (b) XRD patterns of NCA cathode materials prepared by two solid-state methods [152]. Copyright, Springer Berlin Heidelberg. (c) Summarized distribution curves of NCM811 cathode materials prepared by high-temperature solid-state synthesis [156]. Copyright, Elsevier. (d) Schematic diagram of the Ni-Li exchange process [157]. Copyright, American Chemical Society. (e) Tuning thermodynamic and kinetic parameters to control the Ni/Li ordering in high-Ni layered NMC materials [158]. Copyright, John Wiley & Sons, Ltd.

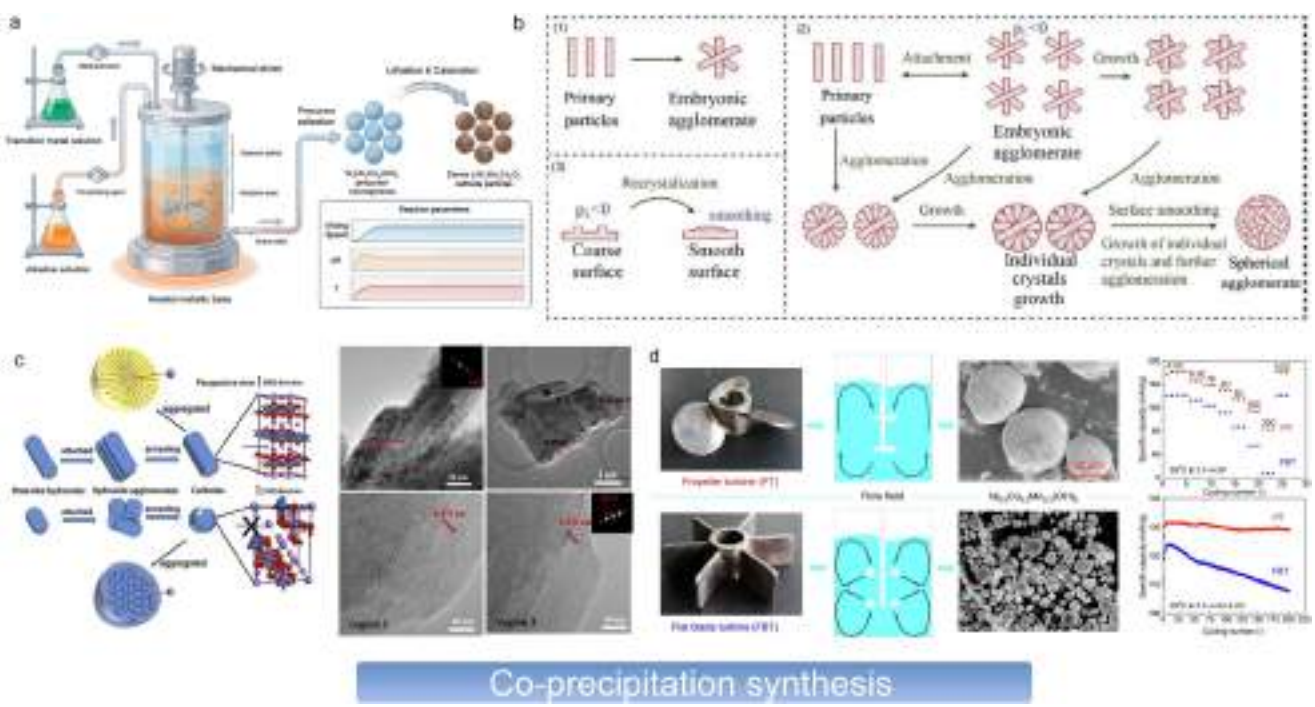


FIGURE 9 | (a) Schematic diagram of coprecipitation synthesis. (b) The formation of embryonic agglomerates, secondary particles, and recrystallization [166]. Copyright, John Wiley & Sons, Ltd. (c) Schematic illustration of ordered and disordered agglomerates and corresponding HRTEM patterns [167]. Copyright, Elsevier. (d) Photos of different types of impellers and corresponding battery performances [2, 168]. Copyright, Elsevier.

16146840, 2026, 26, Downloaded from https://advanced.onlinelibrary.wiley.com/doi/10.1002/aenm.71073 by Jilin University, Wiley Online Library on [07/11/2026]. See the Terms and Conditions (https://onlinelibrary.wiley.com/terms-and-conditions) on Wiley Online Library for rules of use; OA articles are governed by the applicable Creative Commons License

(001) plane of $Ni_{1/3}Co_{1/3}Mn_{1/3}(OH)_2$ exhibits the highest surface energy, leading to preferential growth along this direction. Moreover, surface charge affects adsorption behavior, and ammonium ions (NH^{4+}) preferentially adsorb on negatively charged facets, influencing crystal orientation. As demonstrated in Figure 9c, increasing the ammonia concentration above ~1.5 mol L^{-1} shifts growth dominance to the (001) face, resulting in more ordered, densely packed platelet particles that enhance cycling stability but reduce rate capability. Conversely, lower ammonia levels and higher pH promote less ordered primary particles with preferable rate performance [167].

The formation of dense secondary aggregates requires slow coprecipitation under moderate supersaturation in the presence of ammonia, enabling a dissolution–recrystallization mechanism. Because the solubility (K_{sp}) of transition-metal hydroxides is low, these dynamics only manifest within a narrow pH range: lower pH fosters complexation, while higher pH favors rapid precipitation and suppresses secondary particle maturity. Accordingly, the ideal precipitation pH for producing spherical, uniform secondary particles differs depending on Ni/Co/Mn ratios, as complexation behavior varies for each metal ion and thus influences nucleation/growth pathways. Stirring conditions further impact particle morphology. In experiments by Noh et al., $Ni_{0.5}Co_{0.2}Mn_{0.3}(OH)_2$ precursors prepared at 1000 rpm exhibited high tap densities (2.20 g cm^{-3}) with dense spherical secondary particles, whereas 300 rpm produced irregular shapes with significantly lower density (~1.08 g cm^{-3}) [169]. Similarly, in Figure 9d, Huang et al. compared different impeller types: propeller, inclined turbine, flat blade, and Rushton [168]. They found that only the propeller turbine (PT) generated uniformly dense spherical precursors with tap densities exceeding 2.0 g cm^{-3}.

4.1.1.3 | Hydrothermal Synthesis: Single-Crystal Architectures for High-Voltage Robustness. Hydrothermal synthesis facilitates the formation of highly crystalline and mechanically robust particles, whose reduced internal grain boundaries effectively suppress microcrack formation and parasitic interfacial reactions under high-voltage operation. Hydrothermal synthesis represents a versatile solution-based strategy for producing advanced lithium transition metal oxides, wherein transition metal compounds (Ni, Co, Mn) and lithium salts are dissolved in water and crystallized under high-temperature, high-pressure conditions in a sealed autoclave (Figure 10a). This approach facilitates the formation of well-crystallized, uniformly sized particles with high phase purity and mechanical robustness. Unlike conventional solid-state methods, hydrothermal processes yield submicron-scale structures with reduced particle brittleness and lower susceptibility to moisture uptake, attributes that significantly benefit downstream electrode fabrication. However, this technique relies on specialized high-pressure reactors and imposes limitations on large-scale industrial implementation.

Ge et al.172 reported a CaO-assisted regeneration strategy in which CaO scavenges fluorine impurities as CaF_2, enabling the recovery of structurally intact Ni–Co–Mn oxides with stabilized oxygen vacancy-rich surfaces (Figure 10b). The regenerated cathodes exhibit robust cycling performance (~150 mAh g^{-1} with >95% retention at 1 C) and enhanced Li-ion transport with reduced interfacial resistance. This work highlights an effective route for restoring fluorine-contaminated NCM materials in closed-loop recycling.

Guo and co-workers further advanced the approach by synthesizing single-crystalline NCM811 microrods using a modified hydrothermal oxalate route [171]. In this process, $Ni(CH_3COO)_2{\cdot}4H_2O$ and $Co(CH_3COO)_2{\cdot}4H_2O$ were dissolved in 100 mL ethanol solution, followed by the sequential addition of urea and oxalic acid ($H_2C_2O_2{\cdot}2H_2O$). The mixture was then transferred to an autoclave and heated at 180 °C for 12 h to yield a uniform oxalate precursor ($Ni_{0.89}Co_{0.11}C_2O_4{\cdot}2H_2O$). This was subsequently mixed with $Mn(NO_3)_2$ and a 50% excess of $LiOH{\cdot}H_2O$ in ethanol to form a suspension, which was dried and subjected to thermal treatment at 500°C for 6 h, followed by sintering at 750°C for 12 h (Figure 10c). The resulting NCM811 microrods displayed exceptional electrochemical characteristics. As shown in Figure 10d, this cathode material delivered an initial discharge capacity of 187.2 mAh g^{-1} and retained 95.1% of its capacity after 100 cycles. Even under aggressive high-rate cycling (5 C, 2.8–4.4 V), the cathode maintained a high discharge capacity of 140 mAh g^{-1}. These results highlight the hydrothermal method's potential in enabling high-performance, structurally stable single-crystal NCM cathodes through controlled precursor chemistry and optimized sintering profiles.

4.1.1.4 | Sol–Gel Method: Chemical Homogeneity vs. Cation Disorder at High Voltage. Although sol–gel synthesis enables excellent compositional homogeneity, the coordination environment during gelation strongly affects Li/Ni site occupancy, which has a pronounced impact on lithium-ion mobility and irreversible capacity loss at elevated voltages. The sol–gel method is a quintessential soft-chemistry approach that enables atomic-level homogeneity in precursor mixing, effectively addressing the dispersion and compositional uniformity challenges inherent to high-temperature solid-state reactions. In a typical sol–gel synthesis, metal precursors are first dissolved in a solvent to form a homogeneous solution, followed by the addition of complexing agents to yield a stable sol. Upon gelation, the resultant gel is subjected to drying and subsequent calcination in the presence of lithium sources to produce the cathode materials (as shown in Figure 11a). The entire process progresses through a continuous phase evolution, from molecular to polymeric states, transitioning through sol and gel intermediates, and ultimately crystallizing into the desired oxide phase [173].

Despite its advantages in chemical uniformity and structural control, the sol–gel method remains constrained by prolonged processing times, poor batch-to-batch reproducibility, and the high cost of reagents, factors that hinder its scalability for industrial applications. Moreover, NCM materials synthesized via this method often exhibit pronounced cation disorder, particularly Li/Ni site mixing, which detrimentally affects lithium-ion mobility and overall electrochemical performance. To mitigate these issues, researchers have explored the influence of various solvents and chelating systems on the sol-gel process. Organic agents such as polyvinyl alcohol, glycolic acid, adipic acid, sucrose, and citric acid have been employed to modulate the coordination environment and gelation behavior. Notably, Julien et al. demonstrated that using sucrose as a chelating agent effectively reduced Li/Ni cation mixing in $LiNi_{1/3}Co_{1/3}Mn_{1/3}O_2$,

16146840, 2026, 26, Downloaded from https://advanced.onlinelibrary.wiley.com/doi/10.1002/aenm.71073 by Jilin University, Wiley Online Library on [07/11/2026]. See the Terms and Conditions (https://onlinelibrary.wiley.com/terms-and-conditions) on Wiley Online Library for rules of use; OA articles are governed by the applicable Creative Commons License

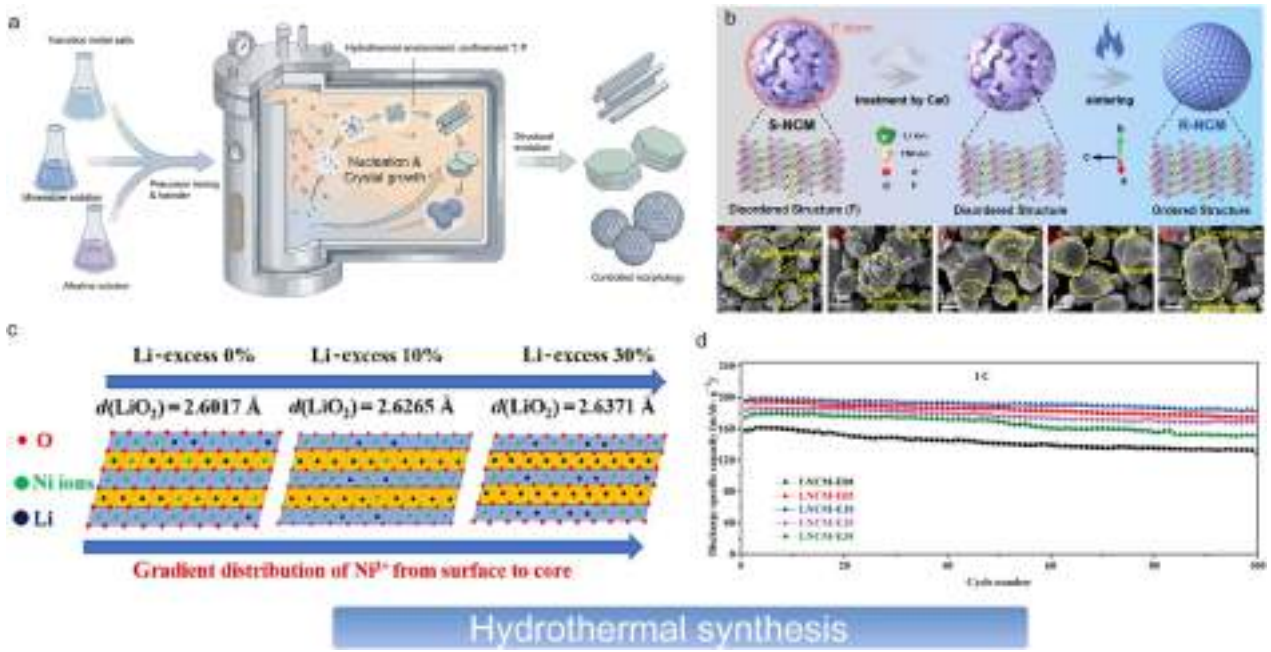


FIGURE 10 | (a) Schematic diagram of hydrothermal synthesis. (b) Schematic of a simple regeneration mechanism and corresponding SEM images [170]. Copyright, Royal Society of Chemistry. (c) Prepared single-crystalline NCM811 cathode materials via hydrothermal synthesis and (d) corresponding electrochemical performance [171]. Copyright, Tsinghua University Press.

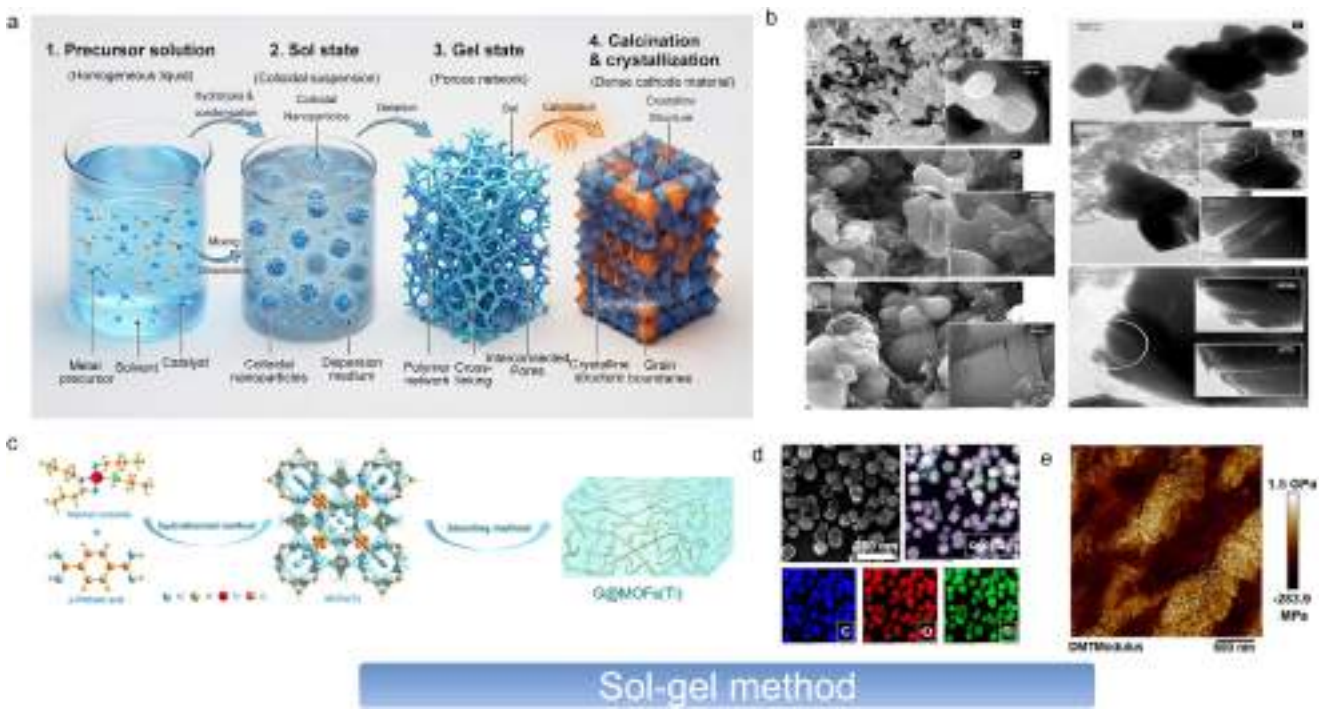


FIGURE 11 | (a) Schematic diagram of the sol–gel method [173]. (b) SEM and TEM images of as-prepared $LiNi_{1/3}Co_{1/3}Mn_{1/3}O_2$ powder [174]. Copyright, Elsevier. (c) Synthesis process of G@MOFs. (d) HRTEM image of synthesized MOF powder. (e) Young's modulus mapping of G@MOFs [175]. Copyright, Royal Society of Chemistry.

resulting in improved capacity retention over extended cycling [174]. These findings underscore the importance of molecular design in tailoring precursor chemistry to optimize cathode functionality (Figure 11b). Beyond cathode synthesis, the sol-gel route also offers a promising platform for fabricating gel polymer electrolytes (Figure 11c–e), which have been shown to enhance the electrochemical interface stability and rate performance of high-energy NCM materials [175]. This dual application potential

16146840, 2026, 26, Downloaded from https://advanced.onlinelibrary.wiley.com/doi/10.1002/aenm.71073 by Jilin University, Wiley Online Library on [07/11/2026]. See the Terms and Conditions (https://onlinelibrary.wiley.com/terms-and-conditions) on Wiley Online Library for rules of use; OA articles are governed by the applicable Creative Commons License

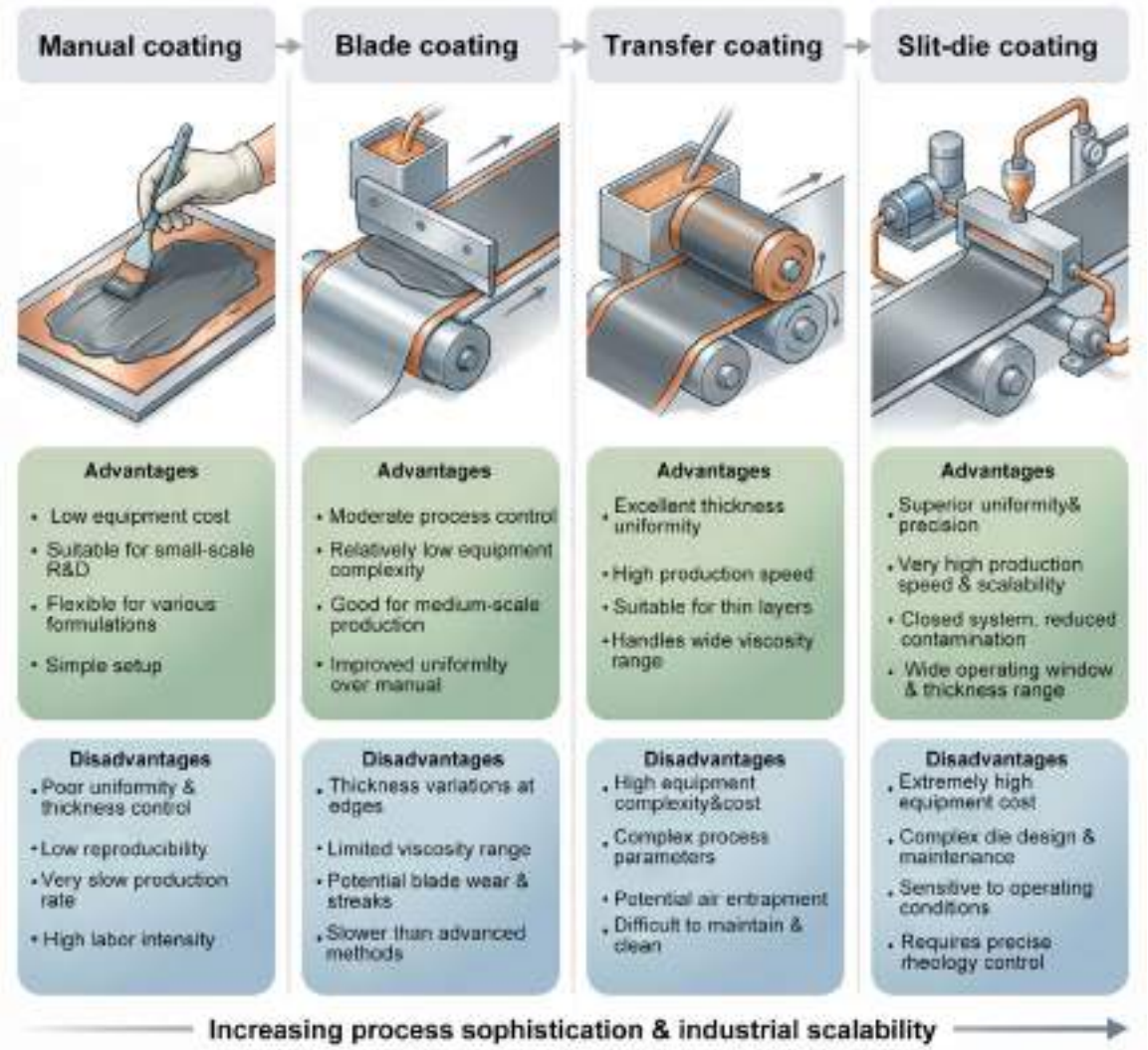


FIGURE 12 | Advantages and disadvantages of coating approaches in wet coating technologies [177].

highlights the versatility of sol-gel chemistry in next-generation lithium battery systems.

4.1.2 | Electrode Manufacturing Technologies and Their Influence on High-voltage Transport and Stability

Beyond material synthesis, electrode manufacturing processes determine mesoscale features such as porosity gradients, binder distribution, and mechanical integrity, which critically control charge transport, interfacial resistance, and degradation pathways in high-voltage electrodes.

4.1.2.1 | Wet Coating Electrode Fabrication: Binder Migration and High-Voltage Polarization. Wet coating remains the dominant fabrication strategy for lithium-ion battery electrodes, involving slurry preparation, film casting, and thermal drying (as shown in Figure 12). It enables precise control over electrode thickness and composition and is widely adopted in industrial production due to its maturity and scalability. Typically, slurries composed of active materials, conductive additives, and polymer binders (e.g., PVDF dissolved in NMP) are cast onto current collectors, followed by solvent evaporation to form dense electrode films [176].

Despite these advantages, wet coating introduces intrinsic limitations that are particularly detrimental under high-voltage conditions. The reliance on volatile solvents such as NMP results in high energy consumption and environmental burden, with solvent evaporation accounting for a major fraction of processing energy. More critically, solvent evaporation induces binder migration, leading to the accumulation of PVDF near the electrode surface. This forms an insulating layer that increases the interfacial resistance and exacerbates polarization, especially under high electric fields.

At the microstructural level, drying-induced gradients also result in nonuniform particle packing, pore distribution, and mechanical stress, particularly in thick electrodes. These effects can cause crack formation and delamination, disrupt electron/ion transport pathways, and accelerate capacity decay. For instance, electrodes with high mass loading often exhibit significantly increased crack density and impedance, posing a major challenge for high-energy (>400 Wh kg^{-1}) systems.

16146840, 2026, 26, Downloaded from https://advanced.onlinelibrary.wiley.com/doi/10.1002/aenm.71073 by Jilin University, Wiley Online Library on [07/11/2026]. See the Terms and Conditions (https://onlinelibrary.wiley.com/terms-and-conditions) on Wiley Online Library for rules of use; OA articles are governed by the applicable Creative Commons License

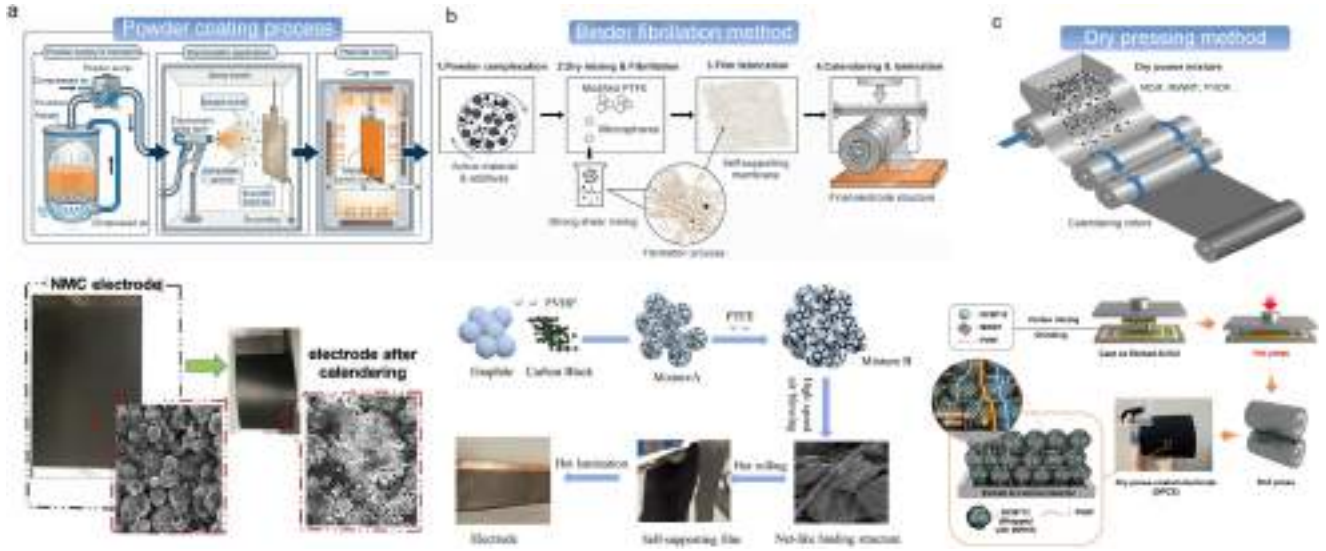


FIGURE 13 | (a) Schematic diagram of the powder coating process [179]. Copyright, Elsevier. (b) Schematic diagram of the binder fibrillation method [180]. Copyright, John Wiley & Sons, Ltd. (c) Schematic diagram of the dry pressing method [181]. Copyright, Springer Nature.

To mitigate these issues, strategies such as surface reconstruction and interfacial engineering have been explored. For example, controlled surface modification of $LiCoO_2$ can generate stable rock-salt-like layers that enhance structural integrity and cycling stability at high voltages. Overall, while wet coating underpins current battery manufacturing, its binder redistribution, energy-intensive processing, and structural heterogeneity represent key bottlenecks for high-voltage applications, motivating the development of alternative fabrication routes and process optimization strategies.

4.1.2.2 | Dry Electrode Fabrication: Thick-Electrode Enablement for High-Voltage Applications. Dry electrode fabrication eliminates solvent-driven binder redistribution, fundamentally altering porosity, tortuosity, and mechanical integrity, thereby enabling stable thick electrodes with reduced polarization and improved voltage utilization. Compared with slurry casting, this approach minimizes solvent use, lowers environmental impact, and avoids impurity incorporation. Dry processing can be broadly classified into powder coating, binder fibrillation, and dry pressing (Figure 13) [178].

In the powder coating process, charged particles are electrostatically deposited onto current collectors and thermally bonded, forming flexible and uniform films (Figure 13a) [182, 183]. Binder fibrillation relies on shear-induced transformation of PTFE into a fibrous network that entangles active materials and conductive additives, creating a self-supporting structure (Figure 13b) [184]. Dry pressing, in contrast, compacts premixed powders onto current collectors by calendaring, producing dense electrodes with high mechanical strength and scalable manufacturability (Figure 13c). Across these methods, shear forces and compaction conditions critically determine particle distribution, film uniformity, and defect formation.

A key advantage of dry processing lies in its ability to precisely control electrode porosity and ion transport pathways [185]. Unlike slurry-cast electrodes, which often suffer from high porosity and binder gradients, dry electrodes exhibit reduced porosity and more uniform microstructures, leading to lower tortuosity and improved Li^+ transport [179, 186, 187]. This is particularly beneficial for high-loading electrodes, where wet processes typically induce cracking and delamination. As a result, dry electrodes can achieve high areal capacities (10 mAh cm^{-2}) while maintaining structural integrity and strong adhesion [188–190].

In addition, the absence of polar solvents makes dry fabrication highly compatible with moisture- and solvent-sensitive systems, such as sulfide-based solid-state batteries [191–193]. The uniform binder distribution and lack of migration also prevent the formation of insulating surface layers, enhancing the interfacial conductivity and high-voltage stability. These features make dry processing especially promising for high-energy-density applications. Furthermore, dry electrodes enable the production of thick electrodes (>5 mA h cm^{-2}) without binder-carbon domain migration, which is critical for achieving high energy density [181, 194, 195]. Notably, the fibrillated PTFE binder would not obstruct electrolyte infiltration pathways and offer better compatibility with high-nickel cathode materials that are difficult to disperse uniformly [196], making it a promising strategy for high-energy and high-power applications. Additionally, dry electrodes exhibit fewer edge defects than their slurry-cast counterparts, rendering them more suitable for large cylindrical cell formats and enhancing production yield.

Despite these advantages, several challenges remain. Achieving uniform particle deposition in powder coatings, controlling fibrillation sensitivity, and mitigating mechanical wear during calendaring all require further optimization. Therefore, continued development of processing control and equipment design is essential to fully realize the potential of dry electrode fabrication for next-generation high-voltage batteries.

16146840, 2026, 26, Downloaded from https://advanced.onlinelibrary.wiley.com/doi/10.1002/aenm.71073 by Jilin University, Wiley Online Library on [07/11/2026]. See the Terms and Conditions (https://onlinelibrary.wiley.com/terms-and-conditions) on Wiley Online Library for rules of use; OA articles are governed by the applicable Creative Commons License

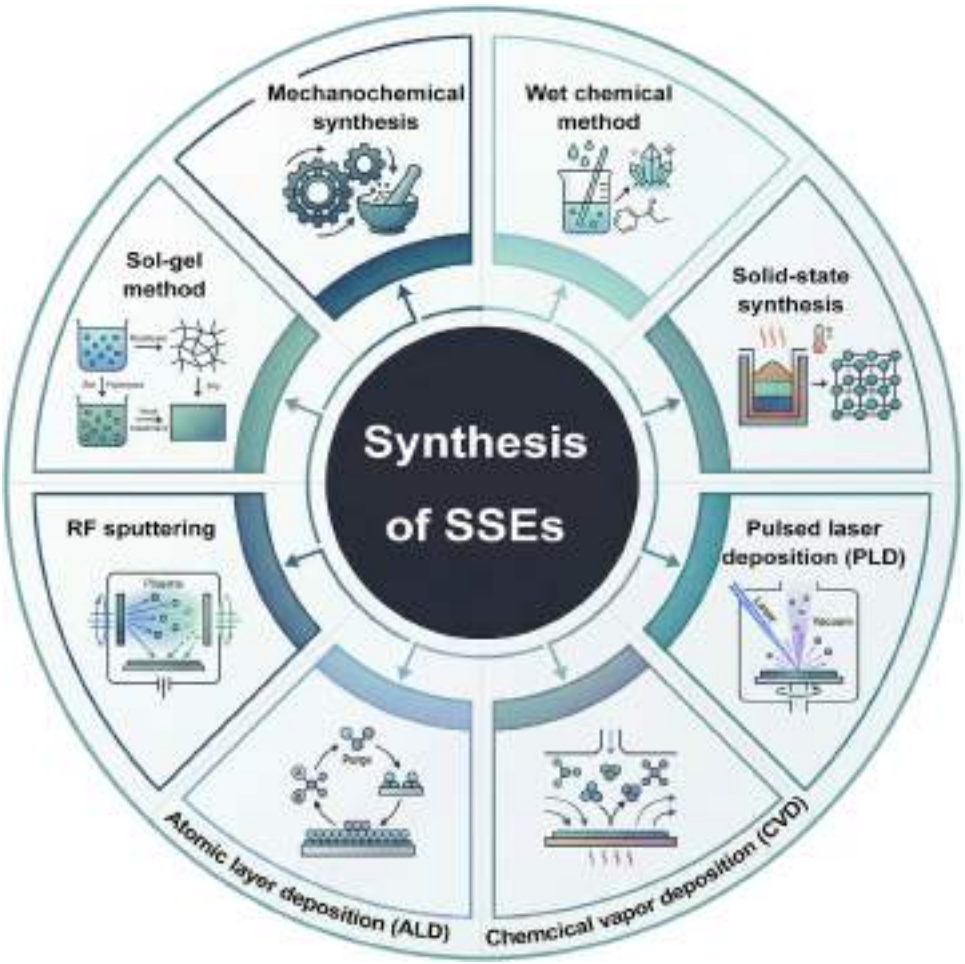


FIGURE 14 | Different synthesis approaches to SSEs for HVLIBs.

4.2 | Preparation of High-Voltage Solid-State Electrolyte: Processing-Dependent Ionic Transport and Stability

For high-voltage solid-state electrolytes, fabrication routes critically determine not only ionic conductivity but also oxidative stability and interfacial compatibility. Under elevated potentials, microstructural heterogeneities, such as defects, impurity phases, and grain boundary chemistry, are significantly amplified, often acting as initiation sites for parasitic reactions and electrolyte decomposition [197].

Consequently, even for identical compositions, variations in synthesis pathways can lead to substantial differences in electrochemical performance. For example, $Li_7P_3S_{11}$ prepared via mechanochemical methods exhibits ~50 times higher ionic conductivity than its wet-chemistry counterpart [198], accompanied by distinct interfacial stability. More importantly, processing-induced differences in phase purity and defect distribution directly affect electronic leakage and grain boundary reactivity, thereby governing the effective electrochemical stability window under high-voltage operation. Therefore, this section reviews key fabrication strategies (Figure 14), including solid-state reaction, sol–gel, coprecipitation, hydrothermal methods, tape casting, sputtering, and in situ polymerization, with emphasis on how processing governs ionic transport and stability under high-voltage conditions.

4.2.1 | Conventional Fabrication Routes: Phase Control and Grain Boundary Effects

The traditional methods for preparing solid-state electrolytes are primarily classified into four categories: high-temperature solid-state synthesis, sol–gel synthesis, coprecipitation, and hydrothermal methods. Conventional synthesis methods primarily affect the crystallographic phase and grain boundary structure of solid-state electrolytes, which dominate the lithium-ion transport resistance and high-voltage interfacial compatibility.

4.2.1.1 | Hydrothermal Method. Hydrothermal processing enables fine particle size and controlled doping, effectively reducing grain-boundary resistance and improving electrochemical stability at high voltages. This approach is particularly advantageous when element doping is employed to enhance the performance of solid-state electrolytes. For example, Peng et al. synthesized Ga-doped $LiTi_2(PO_4)_3$ (LTP), which exhibited superior conductivity compared to undoped LTP [199]. In comparison to sol–gel and coprecipitation methods, the key advantage of the hydrothermal process is that crystallized powders can typically be

16146840, 2026, 26, Downloaded from https://advanced.onlinelibrary.wiley.com/doi/10.1002/aenm.71073 by Jilin University, Wiley Online Library on [07/11/2026]. See the Terms and Conditions (https://onlinelibrary.wiley.com/terms-and-conditions) on Wiley Online Library for rules of use; OA articles are governed by the applicable Creative Commons License

obtained without requiring high-temperature sintering, avoiding potential issues such as the formation of micron-sized agglomerates and eliminating the need for grinding, which could introduce impurities. However, the hydrothermal method is highly dependent on specialized equipment, often requiring high-pressure reactors, which in turn increases the cost of production.

A polyanionic coordination strategy has been introduced to develop a new class of amorphous fluoride solid electrolytes for high-voltage all-solid-state batteries. One-step ball milling of Li_3PO_4 and TiF_4 yields $Li_xTi(PO_4)_{x/3}F_4$ electrolytes, in which the optimized composition exhibits enhanced room-temperature ionic conductivity, exceptional oxidative stability, and favorable mechanical properties, enabled by weak Li^+ interactions within a flexible dual-coordination network. When applied in 5 V-class $LiNi_{0.5}Mn_{1.5}O_4$ all-solid-state batteries, this electrolyte markedly improves capacity retention and cycling stability, highlighting a promising electrolyte design paradigm for high-energy solid-state systems [200].

4.2.1.2 | Coprecipitation Method. Coprecipitation-derived fine powders lower sintering barriers, facilitating dense microstructures that suppress intergranular degradation under high-voltage stress. This method, similar to the sol-gel process, involves the preparation of a solution followed by the addition of a precipitating agent to generate solid precipitates, which are subsequently washed and heat-treated to yield precursor powders. As a wet-chemical synthesis technique, this method ensures uniform mixing of the raw materials and offers advantages such as small particle size, excellent chemical homogeneity, and precise control over dopant levels. Powders produced via coprecipitation typically have smaller grain sizes than those produced by the high-temperature solid-state method. For instance, Hamao et al. synthesized LLZO using coprecipitation, obtaining an average particle size of 9.66 μm, which is significantly smaller than that produced via high-temperature solid-state synthesis (~23 μm) [201]. This smaller grain size can reduce the sintering temperature and time, thereby lowering production costs. The Ci group successfully synthesized LAGP at 750°C using coprecipitation, which is 400°C lower than the high-temperature solid-state method [202]. Thus, the coprecipitation method offers significant advantages, particularly in producing powders with fine particle sizes, which can drastically reduce sintering temperature and time, lower costs, and facilitate doping to improve the performance of solid-state electrolytes.

4.2.1.3 | Sol–Gel Method. Sol–gel synthesis offers molecular-level dopant control, allowing deliberate tuning of bulk and grain-boundary conduction pathways critical for high-voltage operation. This method allows for atomic-level mixing of elements, solving issues related to the dispersion and uniformity of reactants in high-temperature solid-state reactions. During the process, the precursors are dissolved in a solvent to form a uniform solution, which is then transformed into a gel by adding a suitable chelating agent. This gel is subsequently heated, dried, and sintered to yield the final product. Compared to high-temperature solid-state synthesis, the sol-gel method produces precursor materials with fine particle sizes, excellent chemical homogeneity, and lower sintering temperatures. The Stenina group [203] synthesized Al and Zr codoped $Li1+xAl_xZr_yTi_{2-x-y}(PO_4)_3$, demonstrating that the ratio of Al and Zr could be fine-tuned to achieve optimal performance, with the best performing materials being $Li_{1.2}Al_{0.2}Zr_{0.1}Ti_{1.7}(PO_4)_3$ and $Li_{1.1}Al_{0.1}Zr_{0.2}Ti_{1.7}(PO_4)_3$. Kim et al. investigated the effect of element doping on LLZO performance and found that doping with 0.1 mol Rb, 0.2 mol Ga, and 0.6 mol Nb resulted in a high ionic conductivity of 2.22×10^{-4} S cm^{-1} at room temperature and a low activation energy of 0.23 eV [204]. In summary, the sol-gel method plays an important role in the design and development of solid-state electrolytes, offering advantages such as the multifunctionality of precursors and the ability to form inorganic, organic, or hybrid networks in solution. These advantages make it especially suitable for producing solid-state electrolytes with enhanced properties.

4.2.1.4 | High-Temperature Solid-State Method. Although scalable, high-temperature solid-state routes require careful optimization to avoid secondary phase formation that compromises high-voltage ionic transport. This method, a traditional technique for preparing solid-state electrolytes, offers several advantages, such as simplicity, scalability, and suitability for large-scale production. During this process, solid-state electrolytes are typically synthesized by doping elements to enhance their performance. However, when improving the performance, it is essential to consider the production cost. Additionally, the influence of the synthesis process on performance is often due to its impact on the phase structure. Thus, understanding the relationship between the processing parameters and phase structure is critical for optimizing solid-state electrolytes. For instance, Aleksandrov et al. found that heat treatment temperature had a significant effect on the phase structure of LLZO [205], while the heat treatment time did not significantly affect the phase structure. Overall, optimizing the process parameters to obtain high-performance phase structures is a crucial strategy.

4.2.2 | Thin-Film Electrolyte Fabrication for High-Voltage Interfacial Engineering

Thin-film fabrication strategies, including vapor deposition and atomic layer deposition (ALD), have evolved beyond conventional electrolyte synthesis routes and are now increasingly employed as interfacial engineering tools to address the critical challenges in high-voltage solid-state batteries. Unlike bulk solid electrolytes, whose intrinsic electrochemical stability is often thermodynamically limited, thin-film approaches enable the construction of artificial interphases that kinetically suppress interfacial degradation. At high voltages (>4.5 V vs. Li^+/Li), the cathode/solid-state electrolyte interface typically suffers from severe parasitic reactions, including oxidative decomposition of the electrolyte, transition metal dissolution, and the formation of space-charge layers that impede Li^+ transport [86, 206, 207]. In this context, thin-film deposition techniques provide unique opportunities to decouple bulk electrolyte properties from interfacial stability by introducing ultrathin, conformal coatings that function as ionically conductive yet electronically insulating barriers.

4.2.2.1 | Vapor Deposition. Vapor deposition techniques, including physical vapor deposition (PVD) and chemical vapor

16146840, 2026, 26, Downloaded from https://advanced.onlinelibrary.wiley.com/doi/10.1002/aenm.71073 by Jilin University, Wiley Online Library on [07/11/2026]. See the Terms and Conditions (https://onlinelibrary.wiley.com/terms-and-conditions) on Wiley Online Library for rules of use; OA articles are governed by the applicable Creative Commons License

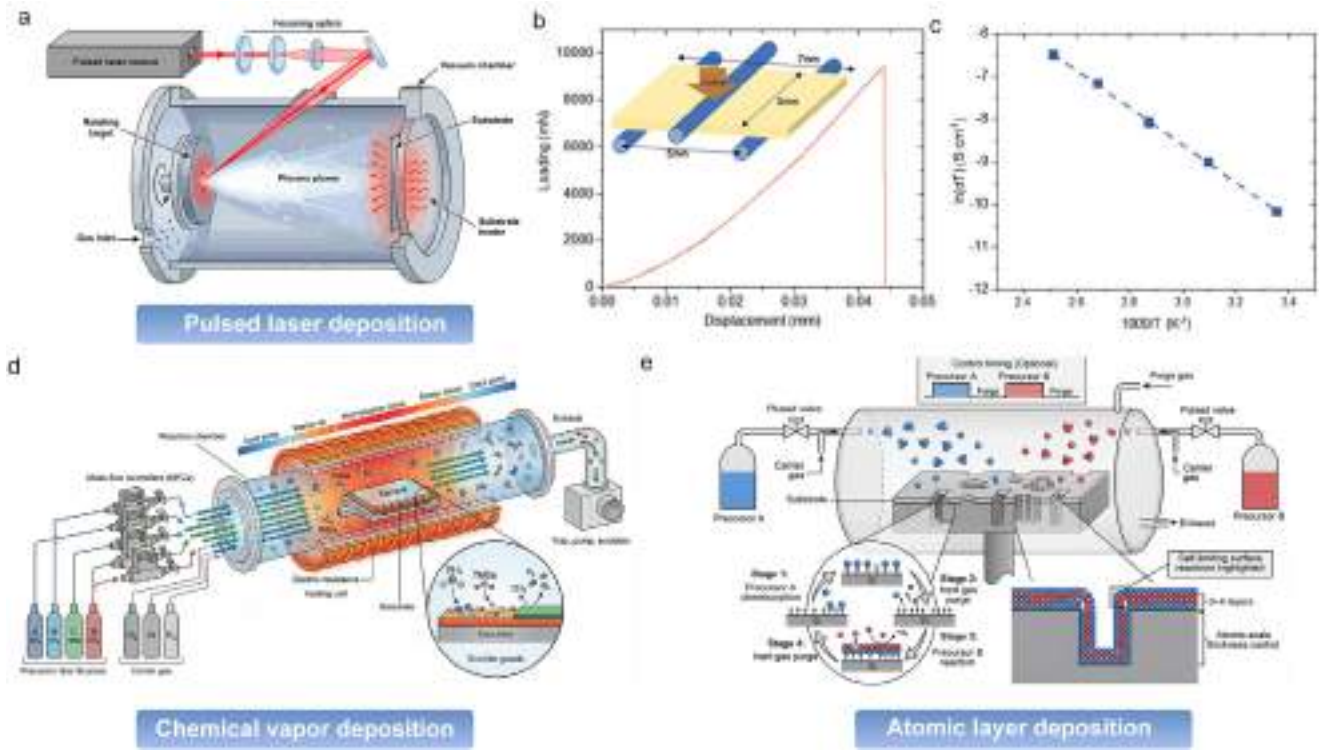


FIGURE 15 | (a) Schematic diagram of pulsed laser deposition. (b) Load–displacement curve of the LLZO film prepared by PLD. (c) Arrhenius plot of the temperature-dependent ionic conductivities of the LLZO film [209]. Copyright, John Wiley & Sons, Ltd. Schematic diagram of (d) chemical vapor deposition and (e) atomic layer deposition.

deposition (CVD), enable the fabrication of dense and compositionally controlled thin films that can act either as standalone electrolytes or, more importantly, as interfacial buffer layers (Figure 15a). PVD methods such as sputtering and pulsed laser deposition (PLD) allow precise tuning of film stoichiometry and defect chemistry, which is critical for stabilizing high-voltage interfaces. For instance, radio-frequency magnetron sputtering has been used to deposit amorphous $Li_{3.3}PO_{3.9}N_{0.17}$ films, which exhibit improved stability against lithium metal and moderate ionic conductivity of 2×10^{-6} S cm^{-1} at 25°C. More importantly, such LiPON-type films are known to possess enhanced oxidative stability (up to 5.5 V) compared to conventional oxide electrolytes, primarily due to nitrogen incorporation that lowers the HOMO energy level [208].

From an interfacial perspective, PLD is particularly advantageous for constructing nanoscale artificial interlayers with controlled thickness and composition. These ultrathin coatings can effectively suppress direct contact between high-voltage cathodes (e.g., layered oxides) and unstable SSEs, thereby mitigating interfacial side reactions. However, despite their high theoretical stability, the practical effectiveness of PLD-derived films is often limited by defects, pinholes, and incomplete coverage, which can lead to localized degradation under prolonged cycling at high voltages. Nevertheless, Hui et al. developed an atmospheric plasma spraying (APS) method for fabricating $Li_7La_3Zr_2O_{12}$ (LLZO) films with thicknesses of approximately 300 μm [209]. The LLZO thin films displayed a flexural strength of 157 MPa, offering notable mechanical flexibility, and achieved an ionic conductivity of 3.82 $\times 10^{-5}$ S cm^{-1} at room temperature (Figure 15b,c). Symmetric Li|LLZO (PEO-coated) | Li cells exhibited low overpotentials of 55 mV at 0.05 mAh cm^{-2} and stable cycling, while full cells with $LiFePO_4$ cathodes delivered initial discharge capacities of 110 mAh g^{-1} with minimal polarization at 0.05 C. During annealing, Al from the crucible diffused into the LLZO films, forming an Al–O eutectic phase at grain boundaries that promoted densification. Increasing the annealing temperature reduced the porosity, with the relative density improving from 90.97% to 97.22% after annealing at 1100°C for 11 h. This tunability highlights the scalability of APS for large-area electrolyte film production.

CVD offers superior conformality over complex and porous electrode architectures, making it particularly suitable for coating high-surface-area cathodes (Figure 15d). For example, aerosol-assisted CVD has been successfully applied to NASICON-type thin films ($Li_{1.5}Al_{0.5}Ge_{1.5}(PO_4)_3$ (LAGP) and $Li_{1.3}Al_{0.3}Ti_{1.7}(PO_4)_3$ (LATP)), which could serve as protective interfaces and suppress interfacial reactions [210]. Notably, polymer-based interlayers prepared via CVD have also demonstrated the ability to accommodate interfacial strain and reduce space-charge layer resistance, owing to their mechanical compliance.

Nevertheless, a key limitation of CVD-derived coatings lies in the balance between film crystallinity and interfacial compatibility. High-temperature processing improves ionic conductivity but may induce undesirable interdiffusion or phase transformation at the interface. Furthermore, even when phase-pure films are achieved under optimized conditions, their ability to withstand high voltages is often governed by kinetic stability rather than thermodynamic immunity, meaning that long-term operation above 4.5 V remains challenging.

16146840, 2026, 26, Downloaded from https://advanced.onlinelibrary.wiley.com/doi/10.1002/aenm.71073 by Jilin University, Wiley Online Library on [07/11/2026]. See the Terms and Conditions (https://onlinelibrary.wiley.com/terms-and-conditions) on Wiley Online Library for rules of use; OA articles are governed by the applicable Creative Commons License

4.2.2.2 | Atomic Layer Deposition. ALD represents one of the most powerful techniques for interfacial engineering in solid-state batteries, owing to its self-limiting surface reactions, which enable nanometer thickness control and exceptional conformality (Figure 15d). In high-voltage systems, ALD is primarily used to deposit ultrathin protective layers (typically <10 nm) that function as artificial cathode/electrolyte interphases. For example, ALD-grown LiPON films exhibit relatively wide electrochemical stability windows and can effectively suppress oxidative decomposition at the interface [211]. The incorporation of nitrogen has been shown to systematically influence film structure and ionic conductivity, highlighting the importance of compositional tuning in optimizing interfacial performance [212]. More importantly, ALD enables the fabrication of multilayer or doped interphases, such as Al-doped LLZO or oxide-nitride hybrid coatings, which combine high ionic conductivity with improved chemical stability. These coatings can reduce interfacial impedance, suppress space-charge layer formation, and inhibit transition metal migration from the cathode [213–215].

However, despite the theoretical promise of ALD-derived interphases, their practical performance at high voltages is often constrained by several factors. First, the electrochemical stability window of most oxide-based coatings is still fundamentally limited by their electronic structure, making them susceptible to slow oxidative decomposition above 4.5–5.0 V. Second, the extremely small thickness required to maintain low resistance can compromise their ability to act as complete barriers, particularly in the presence of mechanical defects or volume changes during cycling. As a result, ALD coatings are better understood as kinetically stabilizing layers rather than absolute protective barriers.

4.2.3 | In Situ Polymerization Electrolyte Fabrication for High-Voltage Interfacial Engineering

To address the issues of poor interfacial contact between solid polymer electrolytes (SPEs) and electrodes, as well as the excessive thickness of electrolyte layers, in situ polymerization has emerged as an effective interfacial engineering strategy [216, 217]. By constructing the electrolyte directly within the battery, this fabrication approach enables intimate electrode/electrolyte integration, thereby enhancing interfacial compatibility and improving stability under high-voltage operation. In situ polymerization represents a simple yet efficient route for the fabrication of solid-state batteries (SSBs). Typically, a homogeneous precursor solution composed of low-viscosity monomers, initiators, and lithium salts is infused into a preassembled cell, allowing thorough infiltration into the porous electrode framework. Subsequent thermal or photochemical polymerization converts the liquid precursor into a solid polymer electrolyte, forming conformal and well-contacted interfaces. Owing to its operational simplicity and effectiveness in interface regulation, this strategy has been widely adopted in both quasisolid-state and solid-state battery systems [218].

The most commonly employed configuration is the separator-assisted strategy, in which the precursor is introduced into a preassembled sandwich structure (cathode/separator/anode) and polymerized within a sealed cell. The separator serves as a physical barrier to prevent internal short circuits, rendering the process highly compatible with conventional LIB manufacturing, in addition to the additional polymerization step. However, this approach presents several inherent limitations. The separator contributes additional inactive mass and nonconductive regions, thereby compromising the energy density. Commercial separator materials, such as cellulose, glass fiber, polyolefins (e.g., Celgard), and PVDF, may further constrain performance optimization. More critically, certain monomers may undergo parasitic reactions on lithium metal, leading to the formation of unstable passivation layers. Consequently, careful selection of precursor chemistry and polymerization pathways is essential, particularly with respect to the electrochemical stability and interfacial reactivity of monomers.

To overcome these challenges, separator-free direct deposition strategies have been developed as an alternative in situ polymerization route. In this approach, the precursor is directly cast onto composite electrode films and then polymerized, yielding electrodes integrated with SPE layers. These electrodes are subsequently assembled into solid-state batteries. In SSB systems, polymerization is typically conducted on the cathode side, followed by pairing with a lithium metal anode. More advanced designs employ stepwise polymerization to construct distinct SPEs on both cathode and anode surfaces, effectively mitigating parasitic reactions at the lithium interface and suppressing transition metal dissolution from the cathode.

For example, Yang et al. reported UV curing outside and subsequent thermal curing inside cell methods to fabricate high-performance SPEs [219]. Compared with separator-assisted methods, direct deposition eliminates redundant mass and inactive ion-transport regions while avoiding direct exposure of lithium metal to reactive precursors. Nevertheless, this strategy imposes stringent requirements on the mechanical robustness and structural integrity of the SPE to ensure sufficient resistance against dendrite penetration in the absence of a separator [220–222].

From a mechanistic perspective, in situ polymerization can be broadly classified into free-radical and ionic polymerization. Free-radical polymerization, typically involving monomers with unsaturated double bonds, proceeds via radical-induced chain growth and remains the most widely utilized pathway. In contrast, cationic polymerization can proceed under relatively mild conditions and, in some cases, enables the direct formation of solid or quasisolid electrolytes without introducing additional impurities. Anionic polymerization relies on electron-withdrawing substituents that activate the double bond, allowing for the formation of highly stable propagating species. In principle, such systems can exhibit high reactivity, yielding polymers with extremely high molecular weights. Table 3 summarizes the key performance metrics of representative high-voltage SPE systems fabricated via in situ polymerization, including electrochemical stability windows, cycling stability, and interfacial impedance evolution.

Despite its promise, current research on in situ polymerization remains largely confined to laboratory-scale coin cells, which typically employ excess lithium and low cathode loadings. These conditions deviate significantly from practical pouch cell

16146840, 2026, 26, Downloaded from https://advanced.onlinelibrary.wiley.com/doi/10.1002/aenm.71073 by Jilin University, Wiley Online Library on [07/11/2026]. See the Terms and Conditions (https://onlinelibrary.wiley.com/terms-and-conditions) on Wiley Online Library for rules of use; OA articles are governed by the applicable Creative Commons License

TABLE 3 | Key performance metrics of high-voltage SPEs via in situ polymerization.

Electrolytes	Ionic conductivity (S cm^{-1})	Voltage window	Polymerization methods	Refs.
SN/LiTFSI/PEGDA	1.1×10^{-4}	4.7 V	Free-radical polymerization	[223]
HFBA/PETEA/LiTFSI	6.3×10^{-4}	4.5 V	Free-radical polymerization	[224]
V-PDOL	1.87×10^{-4}	4.7 V	Free-radical polymerization	[225]
LiMATFSI/POSS	9.09×10^{-5}	5.5 V	Free-radical polymerization	[226]
PVdF/$LiPF_6$/PTMA	7.3×10^{-3}	5.0 V	Free-radical polymerization	[227]
P95/$LiBF_4$/LiTFSI	1.0×10^{-4}	5.5 V	Cationic polymerization	[228]
PDOL/$LiPF_6$	1.5×10^{-5}	4.2 V	Cationic polymerization	[229]
PNGDE/LIFSI	1.0×10^{-4}	4.0 V	Cationic polymerization	[230]
PDCL/LiTFSI	3.54×10^{-5}	5.1 V	Cationic polymerization	[231]
PTXE/LiDFOB	3.76×10^{-3}	6.06 V	Cationic polymerization	[232]
MMA/LiTFSI	1.19×10^{-3}	5.0 V	Anionic polymerization	[233]
P(4CL-TMC)/COF	1.1×10^{-5}	5.25 V	Anionic polymerization	[234]
PECA-SIPN-GF	1.39×10^{-4}	4.97 V	Anionic polymerization	[235]
DOL/LiDFOB	3.6×10^{-4}	4.8 V	Anionic polymerization	[236]
PCTEG/LiTFSI	2×10^{-5}	4.5 V	Anionic polymerization	[237]

configurations, where precise balancing of cell components is essential and minor structural imperfections may be amplified, leading to performance degradation. Therefore, although in situ polymerization offers substantial potential for the development of high-performance solid-state batteries, significant challenges remain for practical implementation. Future efforts should focus on achieving stable operation under realistic conditions, including high cathode loading, ultrathin SPE layers, and limited lithium inventory, which represent critical bottlenecks toward commercialization.

4.3 | Battery Pack Manufacturing Strategies for High-Voltage Safety and Reliability

At the pack level, manufacturing technologies critically govern mechanical robustness, thermal regulation, and electrical insulation constraints that are substantially intensified under high-voltage operation due to increased parasitic reactions, heat generation, and dielectric stress. Accordingly, battery packaging is evolving toward advanced materials, structurally integrated designs, and sustainable manufacturing processes to ensure stability under elevated electrochemical and thermal loads (Figure 16).

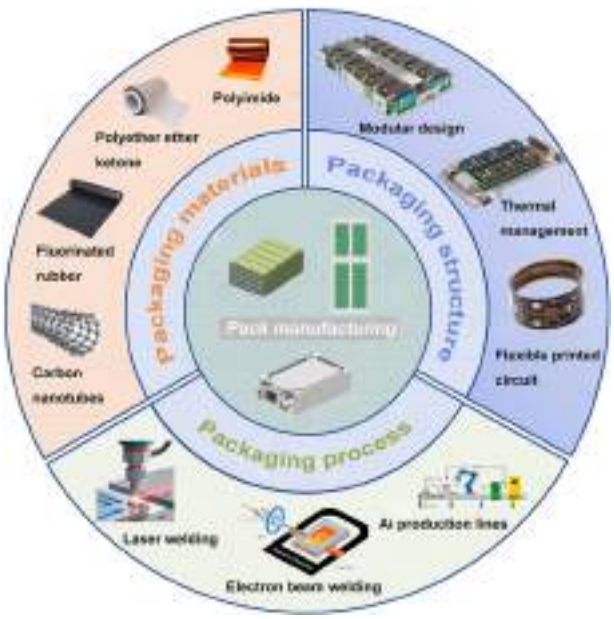


FIGURE 16 | Pack manufacturing for HVLIBs in packaging materials, packaging structure, and packaging process.

4.3.1 | Diversification of Packaging Materials

High-voltage operation imposes stringent requirements on chemical stability, dielectric strength, and thermal tolerance, driving the transition toward hybrid and functionalized packaging materials. The integration of high-performance polymers, such as polyimide (PI) [238] and polyether ether ketone (PEEK) [239], with metal alloys (e.g., aluminum or stainless steel) enables a balance between mechanical robustness and electrical insulation while mitigating degradation induced by high-voltage polarization. Material design is increasingly tailored to voltage-induced stresses. For instance, elevated potentials accelerate electrolyte decomposition and interfacial reactions, necessitating packaging materials with superior chemical inertness and barrier properties. Fluorinated rubber, silicone rubber, and ceramic components are therefore introduced to suppress gas permeation, resist oxidative environments, and enhance thermal stability. Emerging materials further address high-voltage challenges. Graphene, with its high electrical conductivity and thermal dissipation capability,

16146840, 2026, 26, Downloaded from https://advanced.onlinelibrary.wiley.com/doi/10.1002/aenm.71073 by Jilin University, Wiley Online Library on [07/11/2026]. See the Terms and Conditions (https://onlinelibrary.wiley.com/terms-and-conditions) on Wiley Online Library for rules of use; OA articles are governed by the applicable Creative Commons License

facilitates rapid heat spreading and reduces localized Joule heating under high current densities. Similarly, carbon nanotubes (CNTs) and metal organic frameworks (MOFs) improve interfacial stability and barrier performance. In addition, smart materials with stimuli-responsive behavior (e.g., thermally induced expansion forming transient insulation layers) provide adaptive protection against thermal runaway triggered by high-voltage operation [240].

4.3.2 | Structural Innovation in Packaging

Under high-voltage conditions, nonuniform current distribution and localized overheating become more pronounced, making structural design essential for mitigating electrochemical and thermal heterogeneities. Modular architectures improve current distribution pathways and reduce electrical resistance at the pack level, thereby alleviating polarization and enhancing overall energy utilization [241].

Thermal management is particularly critical, as high-voltage operation significantly increases heat generation. Advanced cooling strategies, including liquid cooling and phase change materials (PCMs), enable efficient heat dissipation and temperature buffering. Internalized cooling systems, such as microchannel designs, further enhance thermal uniformity and enable real-time regulation, effectively suppressing hotspot formation that could otherwise accelerate degradation or trigger safety failures [242–244]. To maximize energy density without exacerbating thermal and electrical risks, 3D stacking technologies optimize spatial utilization while shortening current pathways, thereby reducing resistive losses under high-voltage operation. Meanwhile, flexible printed circuits (FPCs) provide reliable and low-resistance electrical connections, accommodating complex geometries while maintaining structural integrity under mechanical and electrochemical stress.

4.3.3 | Environmentally Friendly Manufacturing Process

High-voltage battery systems require manufacturing processes with tighter tolerances and higher reliability, as minor defects can be amplified under elevated electric fields. Precision welding techniques, such as laser and electron beam welding, enable high-integrity joints with minimal heat-affected zones, thereby reducing defect formation and enhancing electrical and mechanical stability [245–247]. In parallel, automated production lines ensure consistent fabrication quality, which is particularly critical for high-voltage applications where variability can lead to uneven current distribution and localized failure. Intelligent control over coating, assembly, and inspection processes allows precise regulation of structural and interfacial properties, improving both safety and long-term reliability under high-voltage operation.

5 | The Multiscale Coupling Mechanisms of Preparation and Performance

As HVLIBs operate under increasingly demanding conditions, performance is governed by tightly coupled phenomena across multiple scales. From atomic-scale reactions to electrode- and cell-level architectures, fabrication processes dictate structural features and interfacial states, which in turn control transport behavior, degradation pathways, and overall battery stability. This section focuses on how specific preparation methods translate into microstructural evolution, interfacial characteristics, and mesoscale transport properties and how these collectively determine macroscopic performance. Through this multiscale perspective, the chapter aims to bridge the gap between fundamental mechanisms and practical battery engineering, providing insights into how coordinated regulation across scales governs the performance, durability, and safety of high-voltage battery systems.

5.1 | Atomic and Nanoscale Interface Chemistry Governed by Electrode Preparation

5.1.1 | Interface Contact Between Electrode Particles

At the atomic and nanoscale, interfacial contact between electrode particles is not an intrinsic material property but is largely governed by electrode preparation routes, including binder selection, conductive network design, and particle-level engineering. These preparation-dependent interfaces determine the local ion/electron transport continuity, mechanical stress distribution, and ultimately macroscopic electrochemical performance.

Insufficient solid–solid contact remains a critical bottleneck for HVLIBs. In conventional lithium-ion systems, liquid electrolytes provide continuous Li^+ transport pathways and effectively infiltrate porous electrodes, ensuring good utilization of active materials. In contrast, solid-state or densely packed systems often suffer from poor interparticle contact (Figure 17). For example, oxide-based cathodes exhibit limited deformability, resulting in relatively low packing densities (70%–80%) even after pressing, while similar issues arise in rigid anode materials. These limitations highlight that interparticle contact quality, determined during fabrication and assembly, directly governs ion transport efficiency and electrochemical stability.

5.1.1.1 | Binder-Mediated Interparticle Contact and Mechanical Integrity. Binder chemistry and architecture directly regulate particle–particle and particle-collector interfaces, determining whether atomic-scale contact can be maintained under repeated electrochemical and mechanical stresses [248]. An ideal binder should provide strong adhesion, mechanical robustness, and electrochemical stability while accommodating volume changes and preserving conductive pathways [249]. Conventional binders (e.g., PVDF, CMC, PAA) offer sufficient adhesion but often fail under large volume fluctuations, especially in Si-based anodes, leading to interfacial degradation and capacity fading.

To address these limitations, advanced binders with self-healing, elastic, and conductive functionalities have been developed. Self-healing systems based on reversible bonding can repair microcracks, while elastic binders buffer volume expansion and maintain structural integrity [250, 251]. Conductive binders further integrate electronic pathways with interfacial adhesion, enhancing charge transfer and cycling stability (Figure 18a)

16146840, 2026, 26, Downloaded from https://advanced.onlinelibrary.wiley.com/doi/10.1002/aenm.71073 by Jilin University, Wiley Online Library on [07/11/2026]. See the Terms and Conditions (https://onlinelibrary.wiley.com/terms-and-conditions) on Wiley Online Library for rules of use; OA articles are governed by the applicable Creative Commons License

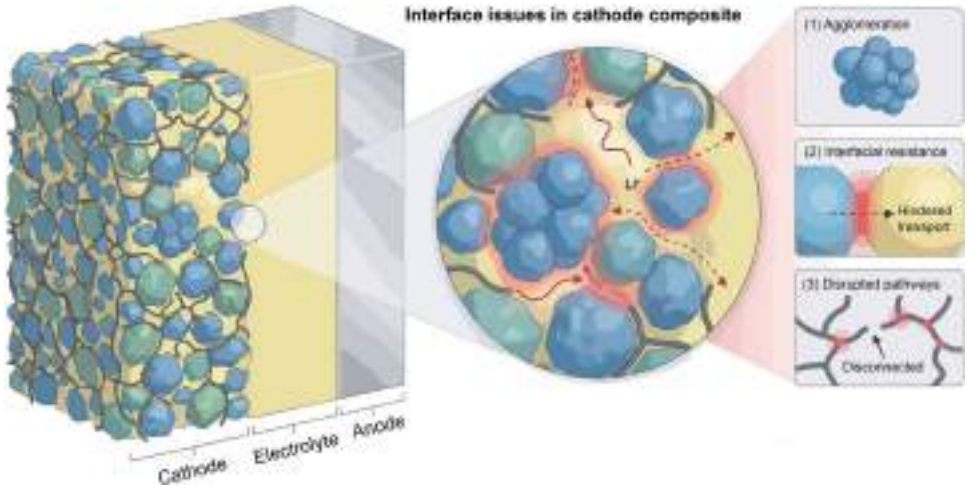


FIGURE 17 | Interface issues in the cathode composite.

[250, 252]. Overall, binder design serves as a critical bridge linking electrode fabrication to interfacial stability and long-term performance. A water-soluble polycarboxylate was developed to form robust chemical bonds between –COOH groups and surface –OH moieties on Si particles, thereby improving interfacial adhesion and stability [253]. The sodium carboxylate groups further enhanced the electronic conductivity and charge transfer, enabling a prolonged cycle life and improved electrochemical performance (Figure 18b). Overall, binder design should prioritize interfacial adhesion and structural resilience, providing a basis for advanced interface engineering in high-performance LIBs. Strategies include (1) introducing functional groups to construct protective interphases with self-healing capabilities, (2) employing branched, grafted, or 3D elastic networks to mitigate stress while facilitating charge transport, (3) optimizing binder content to balance electronic conductivity, mechanical strength, and active material loading, and (4) developing synergistic electrode-binder interfacial architectures to stabilize electrode structure and extend cycle life (Figure 18c). Representative electrochemical performance metrics of different binder classes are summarized in Table 4. Overall, binder design serves as a critical bridge linking macroscopic electrode fabrication to nanoscale interfacial stability. By governing adhesion strength, stress accommodation, and electronic continuity at particle interfaces, advanced binders translate preparation-level decisions into sustained atomic-scale contact and long-term cycling stability in high-performance LIBs.

5.1.1.2 | Conductive Additive Networks as Mesoscale Bridges for Nanoscale Charge Transport. Conductive additives establish mesoscale electron pathways that bridge discrete particles, converting localized contacts into continuous charge-transport networks [270]. Their architecture critically influences conductivity, rate capability, and cycle life. For example, while carbon black ensures uniform dispersion, its high surface area can accelerate side reactions [254]. Hybrid systems combining carbon black with carbon nanotubes (CNTs) improve structural resilience and interfacial contact, enabling high-capacity retention (Figure 18d). Similarly, 3D conductive frameworks (e.g., Ketjen Black) and conductive polymers (e.g., PEDOT:PSS) enhance electronic conductivity and suppress interfacial resistance [255]. As shown in Figure 18e, the resulting electrodes exhibit enhanced conductivity (4.2 S cm^{-1}), suppressed interfacial resistance, and capacities approaching 2000 mAh g^{-1} after 100 cycles at 1 A g^{-1}. These results highlight that conductive additives are not merely compositional components but preparation-controlled structural elements that govern interfacial charge-transfer kinetics and overall electrode performance.

5.1.1.3 | Particle-Level Structural Engineering for Interface Stabilization. Particle-level structural design provides a direct route to stabilizing interfaces by regulating stress distribution, surface chemistry, and electrolyte accessibility. Strategies such as heterostructure design and surface coating can suppress side reactions, improve ion transport, and enhance structural integrity.

For instance, Si-based composites with carbon coatings or 3D conductive frameworks effectively mitigate volume expansion, reduce direct electrolyte contact, and stabilize SEI formation, leading to improved cycling stability (Figure 18f) [256]. This design reduces direct Si-electrolyte contact, prevents repeated SEI rupture, and delivers a stable capacity of 849 mAh g^{-1} over 1000 cycles with minimal impedance growth. Similarly, Furquan et al. employed laser-induced synthesis to construct Si–graphite composites featuring SiC nanowires and a spontaneous ~3 nm carbon/oxide coating [257] (Figure 18g). Dual-layer or heterostructure coatings further combine mechanical buffering with enhanced conductivity, enabling high capacity retention over extended cycling [257]. Collectively, particle-level engineering demonstrates how preparation strategies can simultaneously regulate nanoscale interfacial chemistry and macroscopic electrode stability, providing an effective pathway to reconcile high capacity with long cycle life.

5.1.2 | Interface Between Electrode and Electrolyte

Electrode/electrolyte interphases represent a quintessential multiscale coupling domain, where electrolyte formulation and surface preparation govern atomic-scale reactions, ultimately determining interfacial kinetics, stability, and safety under high-voltage operation.

16146840, 2026, 26, Downloaded from https://advanced.onlinelibrary.wiley.com/doi/10.1002/aenm.71073 by Jilin University, Wiley Online Library on [07/11/2026]. See the Terms and Conditions (https://onlinelibrary.wiley.com/terms-and-conditions) on Wiley Online Library for rules of use; OA articles are governed by the applicable Creative Commons License

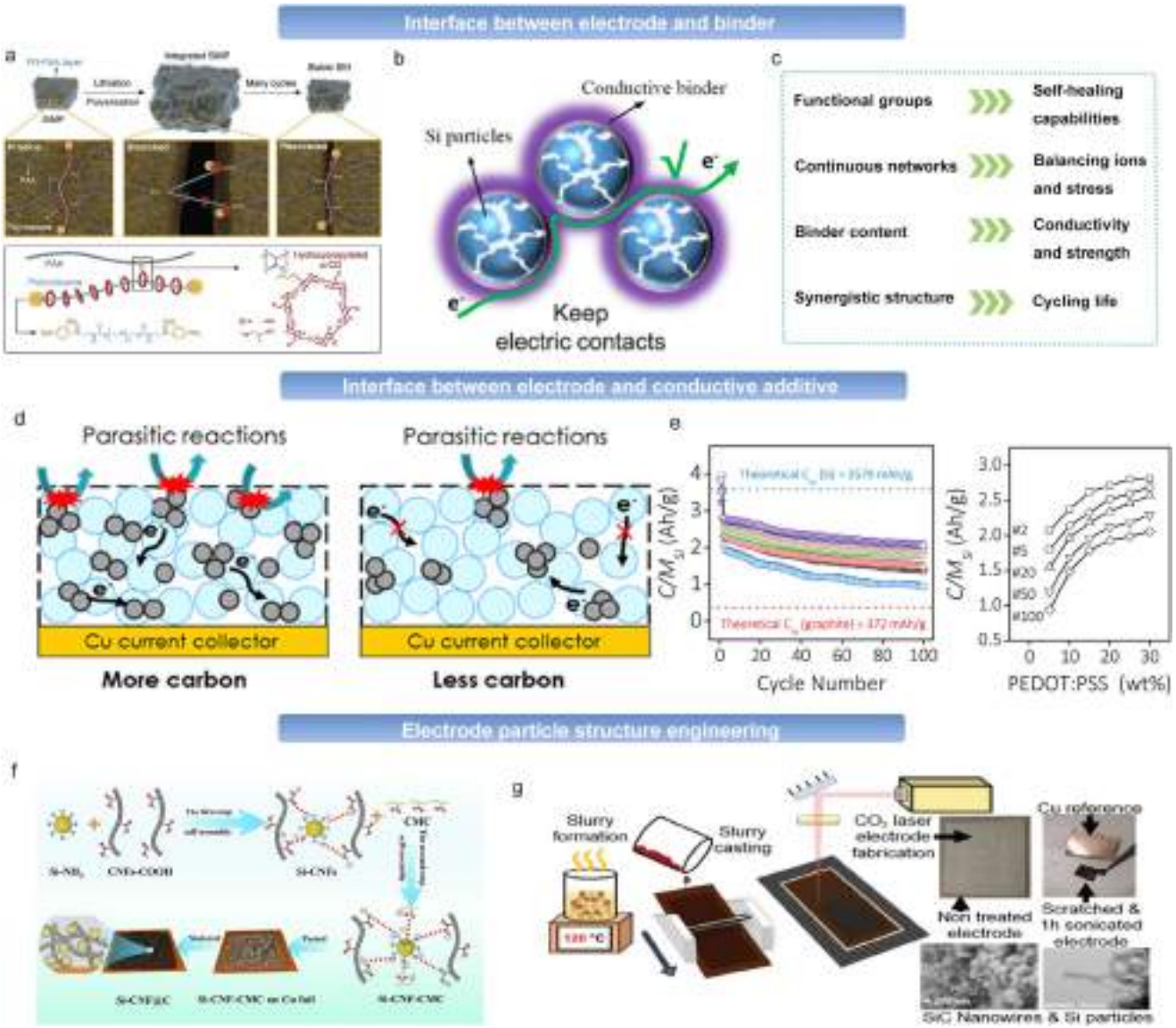


FIGURE 18 | (a) Proposed stress dissipation mechanism of the PR-PAA binder for SiMP anodes [251]. Copyright, American Association for the Advancement of Science. (b) Conductive binder to address volume issues [253]. Copyright, Elsevier. (c) Advanced binder design principle. (d) Role of carbon conductive additive in Si anode [254]. Copyright, American Chemical Society. (e) Cycling performance of PEDOT:PSS/SiNP electrodes [255]. Copyright, American Chemical Society. (f) Synthetic procedure of the Si-CNF@C electrode [256]. Copyright, Elsevier. (g) Schematic of silicon-graphite-furfuryl alcohol electrode fabrication [257]. Copyright, Elsevier.

5.1.2.1 | Preparation-Regulated Formation and Evolution of Anode/Electrolyte Interfaces. During cycling, interfacial electrons at the Li surface trigger electrolyte decomposition, forming a passivation layer known as the SEI [271, 272]. This layer, first defined by Peled [273, 274], is electronically insulating yet ionically conductive, and its formation is fundamentally dictated by electrolyte reactivity. According to frontier orbital theory, electrolyte stability is governed by HOMO-LUMO energy levels, which determine the tendency for reductive decomposition and thus interphase formation [275, 276] (Figure 19a).

The composition and structure of the SEI are strongly dependent on electrolyte formulation (salts, solvents, additives) [281, 282], which regulate Li^+ solvation and decomposition pathways. Typically, the SEI consists of organic species (e.g., ROLi, RCOOLi, $ROCO_2Li$; R = alkyl group) and inorganic phases (e.g., Li_2CO_3, LiOH, Li_2O) [283–285], forming a heterogeneous mosaic structure [286]. Similarly, on the cathode side, electrolyte decomposition generates CEI films that coat active particles [287] (Figure 19b). A widely accepted bilayer model divides the SEI into organic-rich porous domains and inorganic-rich dense regions, which together govern Li^+ transport through coupled pore diffusion and defect-mediated migration (Figure 19c) [278]. However, the intrinsically low ionic conductivity and structural heterogeneity of these phases often limit interfacial kinetics and promote inhomogeneous Li deposition Figure 19d [279, 288–290].

Importantly, although SEI formation originates from spontaneous electrochemical reactions, its thickness, composition, and mechanical integrity are highly preparation dependent, including electrolyte design, surface pretreatment, and artificial interphase engineering. Native SEI layers are typically fragile and uneven,

16146840, 2026, 26, Downloaded from https://advanced.onlinelibrary.wiley.com/doi/10.1002/aenm.71073 by Jilin University, Wiley Online Library on [07/11/2026]. See the Terms and Conditions (https://onlinelibrary.wiley.com/terms-and-conditions) on Wiley Online Library for rules of use; OA articles are governed by the applicable Creative Commons License

TABLE 4 | Summary of the electrochemical performance of advanced electrodes and binders.

Electrode	Binder	Structure	Current density	Cycle performance	Refs.
SiNP	OS-CMC	3D crosslink network	0.4 A g^{-1}	57.3%@100 cycles	[258]
SiMP	SHP-CB	Hydrogen-bond-directed network	0.4 A g^{-1}	79.2%@120 cycles	[259]
Si	CA-PAA	In situ cross-linking network	0.1 C	89.5%@300 cycles	[260]
SiO_x/graphite-NCM811	4A-PAA	Star-shaped network	0.1 A g^{-1}	81.5%@100 cycles	[261]
Si@SiO_x	PANI-PA	Conductive polymer network	1 A g^{-1}	64.2%@500 cycles	[262]
$Li_{1.2}Co_{0.13}Ni_{0.13}Mn_{0.54}O_2$	CMC	Hydrogen-bond-directed network	0.2 A g^{-1}	79.5%@500 cycles	[263]
$Li_{1.2}Ni_{0.2}Mn_{0.6}O_2$	SA	3D crosslink network	0.1 C	93.3%@50 cycles	[264]
$LiNi_{0.5}Mn_{1.5}O_4$	Chitosan	3D crosslink network	1 C	92.7%@100 cycles	[265]
$LiNi_{0.5}Mn_{1.5}O_4$	PAN-PVA	Copolymer	0.01 A g^{-1}	96.5%@30 cycles	[266]
$LiMn_2O_4$	PVA	Hydrogen-bond-directed network	0.2 C	82.1%@300 cycles	[267]
$LiNi_{0.5}Mn_{1.5}O_4$	P(BMA-AN-St)	Copolymer	0.5 C	82.5%@300 cycles	[268]
$Li_3V_2(PO_4)_3$	LiPAA	Conductive polymer network	10 C	91.5%@1400 cycles	[269]

leading to continuous electrolyte decomposition, increased resistance, and dendrite growth.

To enhance interfacial stability, in situ strategies have been developed to construct robust inorganic-rich SEI layers. For example, nitrogen-containing treatments or $LiNO_3$ additives promote the formation of Li_3N, while halide-based chemistries (LiF, LiCl, etc.) provide higher mechanical strength and ionic conductivity [291–293]. Fluorinated electrolytes and additives (e.g., FEC, LiFSI) are particularly effective in forming LiF-rich interphases, which suppress parasitic reactions and stabilize Li deposition [294]. Other additives, including ionic liquids and borate compounds, further regulate interphase uniformity and composition (Figure 19e) [280, 295, 296].

Alternatively, ex situ artificial interphases offer precise control over interface properties. Coatings such as carbon-based layers, polymers, and inorganic films (e.g., Al_2O_3, Li_3PO_4) deposited via ALD or sputtering can enhance mechanical robustness and ensure uniform Li^+ flux [297–300]. Incorporating lithophilic components further homogenizes the ion distribution, reduces the local current density, and suppresses dendrite growth. In addition, interphases that immobilize anions can increase Li^+ transference numbers, improving interfacial transport kinetics [301].

Despite significant progress, no single strategy can fully stabilize the interface. For HVLIBs, interphase instability is further exacerbated by strong oxidative conditions and transition metal dissolution from cathodes, which can migrate to the anode and disrupt SEI integrity. Therefore, achieving stable operation requires multiscale coupling of electrolyte design, interphase chemistry, and mechanical regulation, bridging preparation strategies with interfacial transport and long-term cycling stability.

5.1.2.2 | Cathode/Electrolyte Interphase Engineering Under High-Voltage Conditions. At elevated voltages, CEI formation becomes highly sensitive to cathode surface chemistry and electrolyte oxidation pathways, both of which are strongly governed by material synthesis, surface modification, and electrolyte design. The CEI concept, first evidenced on $LiCoO_2$ surfaces (Figure 20a) [302], has been understood as a product of electrolyte oxidation. Shortly thereafter, Takehara employed FTIR to identify carboxylate groups within the CEI in Figure 20b [303]. Despite differing mechanistic views, it is widely accepted that a stable CEI arises from the synergistic assembly of inorganic and organic components, which collectively determine the interfacial stability and electrochemical performance (Figure 20c) [304, 305].

Under high-voltage operation (>4.5 V), CEI evolution is further complicated by cathode phase transitions, oxygen release, and transition-metal dissolution, which accelerate electrolyte decomposition and lead to heterogeneous, unstable interphases. These coupled degradation processes significantly increase interfacial resistance and limit long-term cycling stability, making CEI engineering a critical requirement for high-voltage batteries. Current strategies primarily focus on artificial CEI construction

16146840, 2026, 26, Downloaded from https://advanced.onlinelibrary.wiley.com/doi/10.1002/aenm.71073 by Jilin University, Wiley Online Library on [07/11/2026]. See the Terms and Conditions (https://onlinelibrary.wiley.com/terms-and-conditions) on Wiley Online Library for rules of use; OA articles are governed by the applicable Creative Commons License

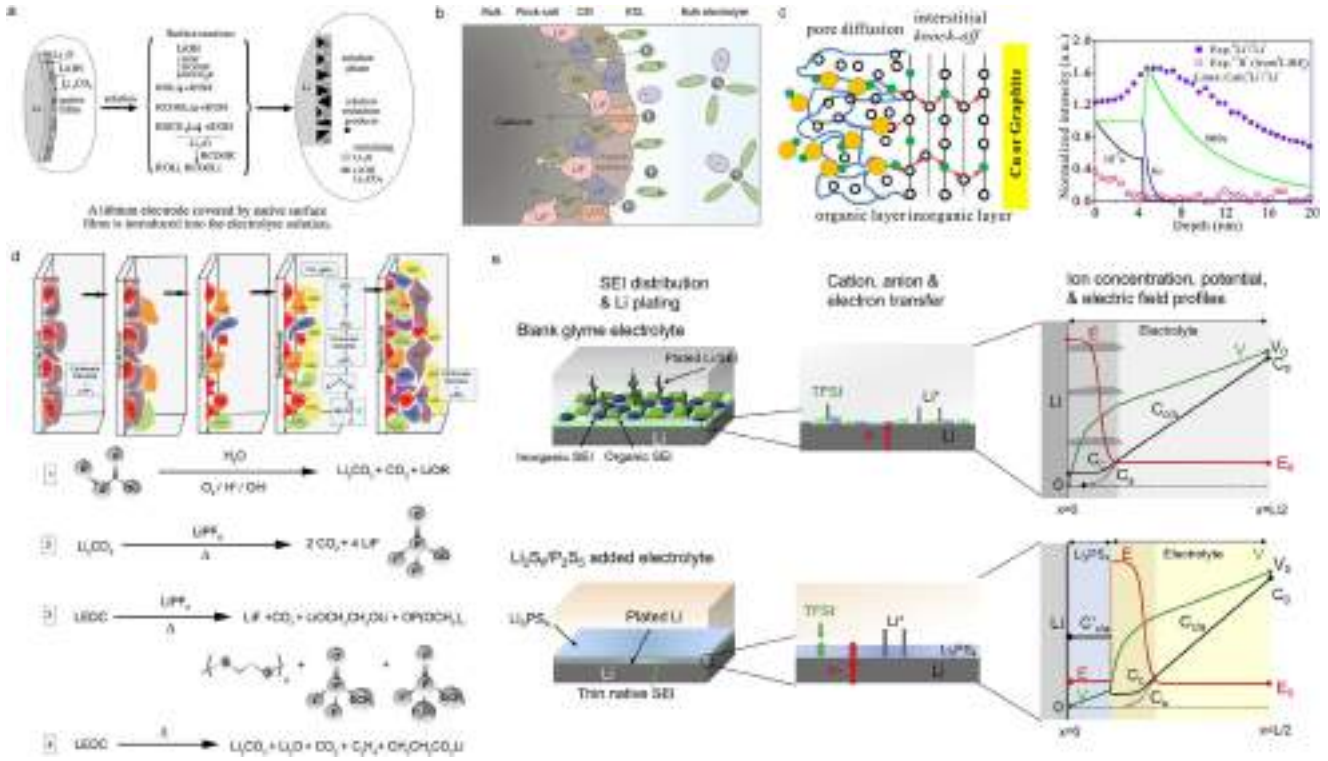


FIGURE 19 | (a) The surface films on the lithium anode after exposure to the electrolyte [277]. Copyright, American Chemical Society. (b) CEI structure and composition during the charging process [106]. Copyright, John Wiley & Sons, Ltd. (c) Pore diffusion in the porous organic layer of the SEI and knock-off diffusion in the dense inorganic layer of the SEI [278]. Copyright, American Chemical Society. (d) Initial SEI evolution on graphite showing the structure, thickening, and subsequent decomposition [279]. Copyright, John Wiley & Sons, Ltd. (e) SEI formation and the ion/electron transfer process during Li plating in glyme electrolyte and glyme with added Li_2S_6/P_2S_5 [280]. Copyright, Elsevier.

and electrolyte-driven in situ regulation. Artificial coatings (e.g., oxides, fluorides, phosphates) can effectively suppress parasitic reactions and stabilize cathode surfaces. For instance, amorphous oxide layers and Li^+-conductive artificial CEIs improve mechanical robustness and mitigate irreversible phase transitions at high voltages. However, such coatings often suffer from nonuniformity and limited mechanistic generality, restricting their scalability in Figure 20d [213, 307, 309, 310].

Beyond conventional oxides and fluorides, more sophisticated artificial CEIs have been explored. Ai and coworkers demonstrated an artificial Li^+-conducting CEI (ALCEI) formed on NCM811 through a nucleophilic reaction between polysulfide ions (Li_xS_8) and VC (Figure 20e) [308]. This ALCEI layer exhibited excellent mechanical flexibility, high ionic conductivity, and effective suppression of interfacial side reactions, thereby preventing irreversible phase transitions and enhancing reversibility at 4.5 V. Conductive polymers also provide a dual benefit: improving electronic conductivity while stabilizing cathode surfaces. In addition, the Wang group deposited polypyrene on LNMO, which improved coulombic efficiency and suppressed Mn^{4+} and Ni^{2+} dissolution while mitigating electrolyte oxidation [311]. Although artificial CEIs can stabilize cathodes even under extreme voltages (~4.9 V), simpler and more effective coating strategies are still highly desirable compared with electrolyte-driven in situ CEI formation.

In parallel, electrolyte engineering provides a more adaptable route by tuning Li^+ solvation structures and oxidation pathways. High-concentration and weakly solvating electrolytes can regulate interfacial reactions, although issues such as high viscosity and cost remain [312]. In practice, carbonate-based electrolytes with functional additives are more viable. Additives containing fluorine, boron, phosphorus, silicon, and nitrogen preferentially oxidize to form protective CEIs. Among them, fluorinated additives are particularly effective in generating LiF-rich interphases with high mechanical strength and oxidative stability [66, 313–316]. Boron- and phosphorus-containing species further enhance CEI robustness while offering additional functionalities such as flame retardancy, whereas nitrogen-containing molecules can extend voltage stability toward 5 V [317–322].

Taken together, CEI chemistry could be viewed as a preparation-dependent interfacial outcome governed by the interplay between electrolyte composition, solvation structure, and cathode surface engineering. The rational design of these factors enables the stabilization of interfacial reactions under extreme oxidative conditions, thereby bridging atomic-scale interphase chemistry with macroscopic voltage tolerance and long-term cycling stability in high-voltage lithium batteries.

5.2 | Microscale Electrode–Electrolyte Structural Optimization Bridging Interfaces and Device-Level Energy Density

While atomic and nanoscale interfacial chemistry governs local reaction kinetics, achieving high energy density at the device

16146840, 2026, 26, Downloaded from https://advanced.onlinelibrary.wiley.com/doi/10.1002/aenm.71073 by Jilin University, Wiley Online Library on [07/11/2026]. See the Terms and Conditions (https://onlinelibrary.wiley.com/terms-and-conditions) on Wiley Online Library for rules of use; OA articles are governed by the applicable Creative Commons License

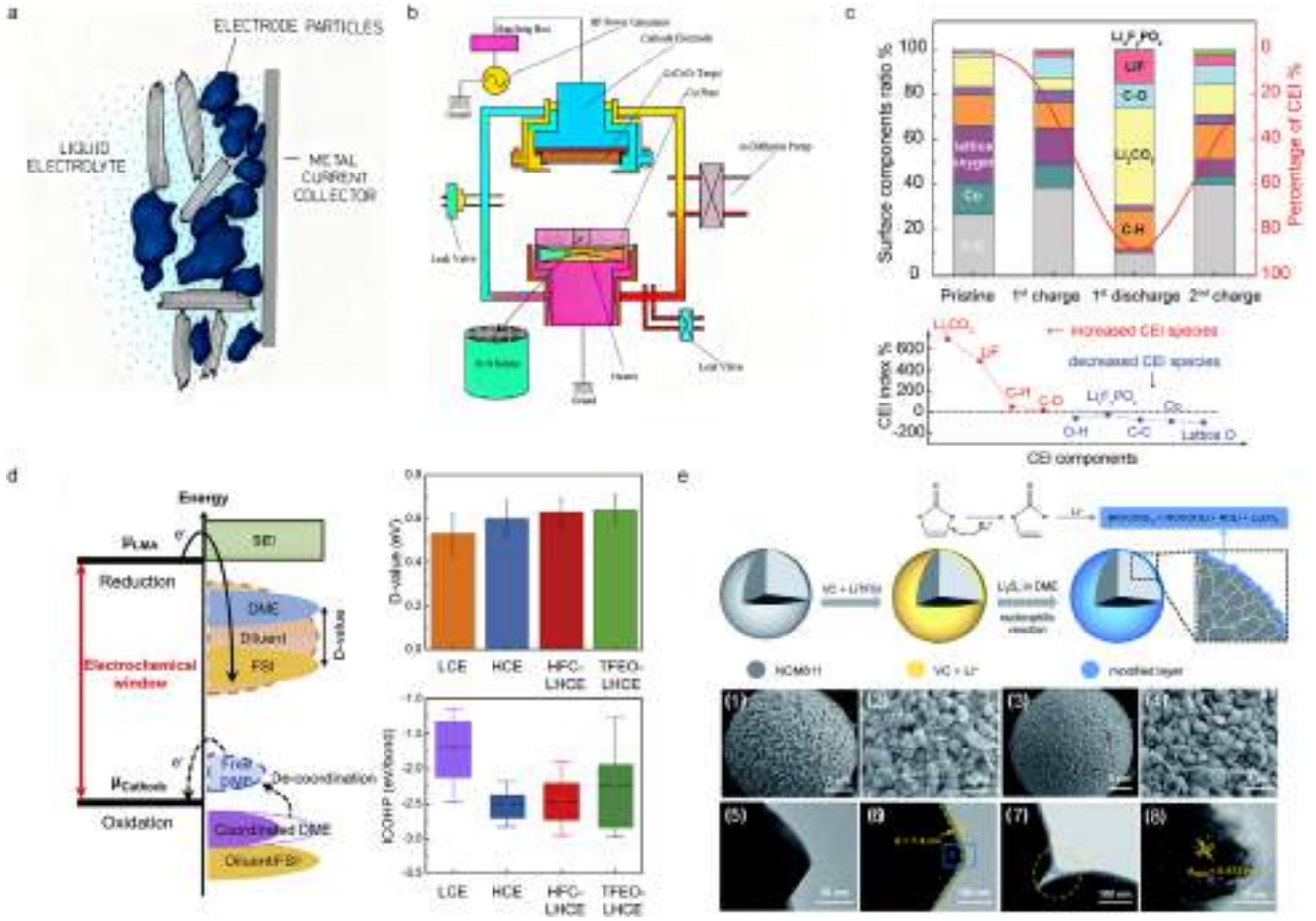


FIGURE 20 | (a) The surface films on $LiCoO_2$ after exposure to electrolyte [302]. Copyright, Electrochemical Society, Inc. (b) Sputtering equipment for the preparation of $LiCoO_2$ thin film [303]. Copyright, Elsevier. (c) The chemical composition of the interface layer on the $LiCoO_2$ cathode probed by XPS at different charge and discharge states and CEI components for different CEI indices [306]. Copyright, Elsevier. (d) Modulating the electrochemical window by anodic and cathodic descriptors [307]. Copyright, Elsevier. (e) Schematic illustration of the fabrication process of the ALCEI-modified NCM811 material and corresponding SEM images of ALCEI-modified NCM811 [308]. Copyright, Royal Society of Chemistry.

level critically depends on microscale electrode architectures, which regulate ion/electron transport over extended length scales. In this context, thick electrode design serves as a key strategy to translate interfacial advantages into practical areal and volumetric energy density.

5.2.1 | Thick Electrode Structure Optimization

Electrodes fundamentally determine the upper limit of energy density by controlling the amount of active material [323]. Beyond material selection, electrode architecture, dictated by fabrication processes, plays a decisive role in balancing energy density and transport kinetics. Strategies such as nanostructuring [324, 325] and surface engineering [326] can enhance interfacial reactivity and electrode/electrolyte interactions. However, their benefits are often diminished when transitioning to thick electrodes.

As the electrode thickness increases, microscale transport limitations dominate, leading to sluggish ion diffusion, increased polarization, and reduced mechanical stability [327]. These limitations originate from fabrication-induced structures, where randomly packed particles create high tortuosity and restricted ion pathways. According to the effective ionic conductivity relationship:

$$D_{\text{eff}} = \frac{\varepsilon}{\tau} D \tag{1}$$

where ε and τ represent the porosity and tortuosity of the electrode, respectively, and D denotes the intrinsic ionic conductivity. It is evident that the effective ionic conductivity is strongly governed by both porosity and tortuosity. Consequently, thick electrodes with porous architectures and low tortuosity can simultaneously sustain efficient ion/electron transport and elevate the volumetric energy-density limit (Figure 21a,b) [328–330].

Importantly, these challenges are not intrinsic to materials but arise from electrode fabrication routes, motivating the development of advanced processing strategies [332]. Techniques such as 3D printing (Figure 21c), solvent-induced phase separation (Figure 21d), and directional freezing (Figure 21e) enable the construction of ordered, hierarchical structures with optimized porosity and integrated conductive networks. These engineered architectures effectively shorten transport pathways, enhance

16146840, 2026, 26, Downloaded from https://advanced.onlinelibrary.wiley.com/doi/10.1002/aenm.71073 by Jilin University, Wiley Online Library on [07/11/2026]. See the Terms and Conditions (https://onlinelibrary.wiley.com/terms-and-conditions) on Wiley Online Library for rules of use; OA articles are governed by the applicable Creative Commons License

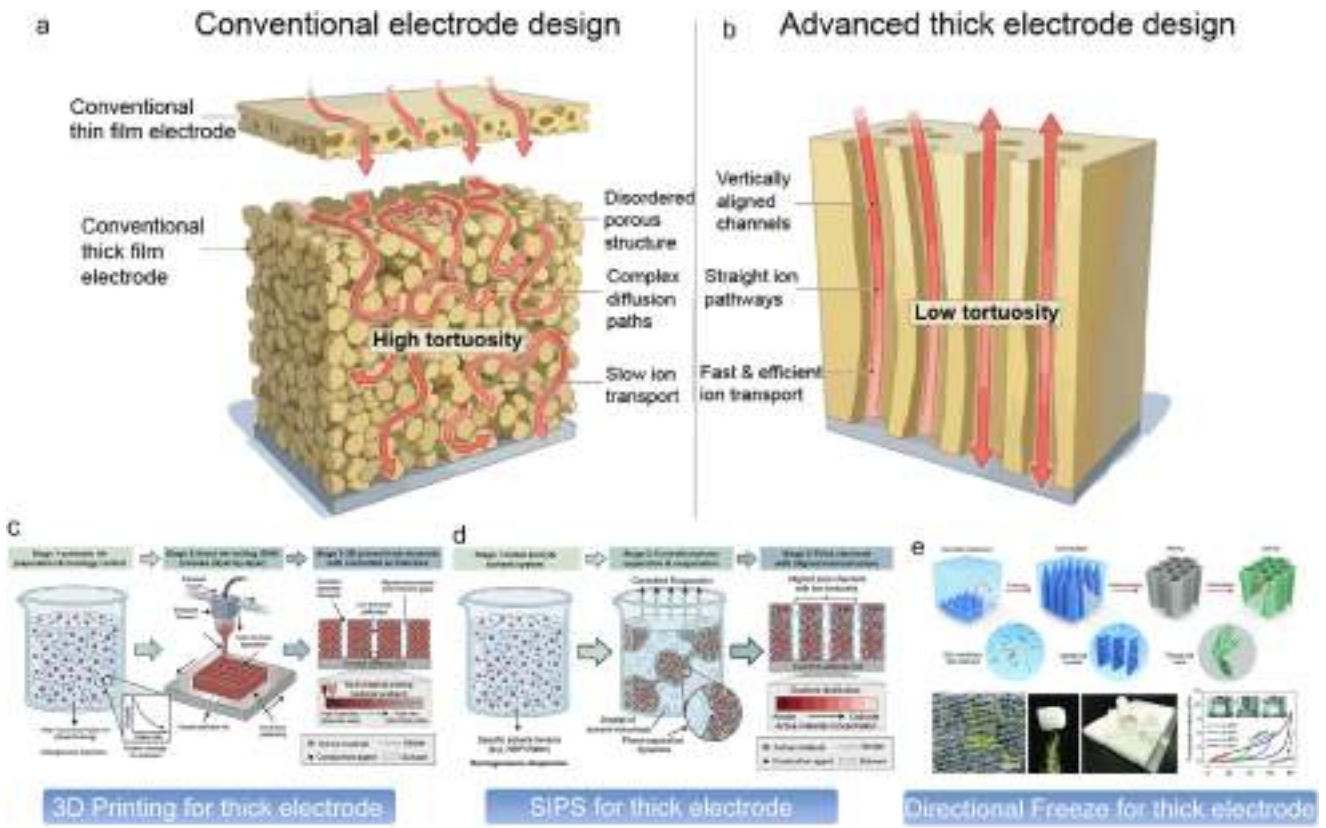


FIGURE 21 | Schematics illustrating the ion transfer pathways in (a) conventional electrode and (b) novel thick electrode [330]. (c) 3D printing of thick electrodes. (d) Solvent-induced phase separation for a thick electrode. (e) Directional freeze for thick electrode [331]. Copyright, American Association for the Advancement of Science.

mechanical integrity, and mitigate polarization, thereby enabling thick electrodes to achieve both high energy density and stable electrochemical performance.

5.2.1.1 | 3D printing-Enabled Microscale Architecture Control. 3D printing provides a direct route to program microscale electrode architectures during fabrication, enabling the decoupling of electrode thickness from transport tortuosity. Constructing ordered, low-tortuosity pathways facilitates efficient ion/electron transport in high-mass-loading electrodes. Techniques such as direct ink writing and inkjet printing allow precise control over microstructure, improving electrochemical kinetics and energy density. Representative studies demonstrate that 3D-printed electrodes with engineered microchannels and hierarchical networks can significantly enhance ion diffusion and maintain high areal capacities even at large thicknesses [333–336]. The integration of conductive frameworks (e.g., CNTs, MXene) further improves mechanical flexibility and charge transport, enabling high energy density without sacrificing rate capability [337, 338].

However, practical limitations remain, including limited printable materials, wettability challenges, and high cost, which constrain large-scale applications. Overall, 3D printing highlights how direct structural encoding during fabrication translates into improved transport kinetics and device-level performance, although further advances in materials and scalability are needed.

5.2.1.2 | Phase Separation-Driven Microscale Pore Engineering. Solvent-induced phase separation (SIPS) offers a scalable strategy to construct low-tortuosity, aligned pore networks through thermodynamically driven microstructure evolution [339, 340]. By controlling solvent/nonsolvent interactions and evaporation dynamics, electrodes with tailored porosity and directional channels can be fabricated. Compared with conventional electrodes, which exhibit high tortuosity and limited ion transport, phase-separation-engineered structures significantly shorten diffusion pathways and reduce polarization [341, 342]. For example, vertically aligned or finger-like pore architectures can reduce tortuosity to ~1.9, enabling substantial increases in areal capacity (14 mAh cm^{-2}) at high mass loadings of 60 mg cm^{-2} [343], which is three to four times higher than conventional electrodes.

Nonsolvent-induced phase separation (NIPS) represents a related approach in which the incompatibility between solvents and nonsolvents drives the formation of well-defined microstructures [344]. By controlling the exchange kinetics of solvent and nonsolvent, phase separation in polymer-based slurries can be tailored to generate architectures ranging from low tortuosity finger-like channels to high tortuosity sponge-like networks. For instance, Li and coworkers applied NIPS to sodium vanadium phosphate cathodes by dispersing slurries in DMF and immersing them in nonsolvents, followed by carbonization to yield self-supporting NVP@C thick electrodes [345]. Finite element simulations confirmed that finger-like, low-tortuosity structures ensured

16146840, 2026, 26, Downloaded from https://advanced.onlinelibrary.wiley.com/doi/10.1002/aenm.71073 by Jilin University, Wiley Online Library on [07/11/2026]. See the Terms and Conditions (https://onlinelibrary.wiley.com/terms-and-conditions) on Wiley Online Library for rules of use; OA articles are governed by the applicable Creative Commons License

uniform sodium-ion distributions with minimal concentration gradients, while sponge-like morphologies produced pronounced ion accumulation and polarization. Consequently, low-tortuosity electrodes exhibited homogeneous current distributions and superior electrochemical kinetics, underscoring the pivotal role of phase separation control in thick-electrode design. These studies collectively demonstrate that phase separation-controlled microscale architectures can effectively convert increased electrode thickness into practical gains in areal energy density without sacrificing transport kinetics.

5.2.1.3 | Directional Freeze-Casting for Aligned Ion-Transport Architectures. Directional freeze-casting enables precise control over pore orientation by templating electrode structures through ice crystallization. This process produces anisotropic, aligned channels that significantly reduce tortuosity and enhance ion transport across thick electrodes [346–350].

Freeze-cast electrodes exhibit hierarchical and gradient pore structures, which balance ion transport and mechanical stability [351, 352]. Such architectures enable high areal capacities (>10 mAh cm^{-2}) and stable cycling even under high current densities and high-voltage conditions [353]. The aligned channels effectively suppress concentration polarization and promote uniform electrochemical reactions. Moreover, Yu et al. engineered a bioinspired carbon scaffold with tunnelable vertical microchannels [354]. Freeze-casting allowed precise pore-size control by adjusting the initial freezing temperatures. The microchannels, decorated with Sn/Ni nanoparticles, served as preferential nucleation sites for lithium metal deposition. The optimized scaffold with ~14 μm pores exhibited ultralow overpotential (~18 mV) and stable cycling for 500 cycles in symmetric Li cells.

Despite these advantages, challenges such as structural inhomogeneity, processing complexity, and scalability remain. Nevertheless, freeze-casting demonstrates a powerful route to synchronizing electrode thickness with transport efficiency, enabling stable operation under high-loading and high-voltage conditions.

5.2.2 | Electrode and Electrolyte Wetting and Ion-Electron Transport

Beyond solid-phase architecture, the performance of thick electrodes in HVLIBs critically depends on electrolyte infiltration, interfacial wetting, and coupled ion/electron transport [355, 356]. At the microscale, the electrical double layer (EDL) bridges nanoscale interfacial chemistry with macroscopic transport behavior, governing Li^+ desolvation, interfacial reactions, and SEI/CEI formation. Under high-voltage conditions, strong electric fields and oxidative environments significantly alter the EDL structure, ion distribution, and coordination chemistry, thereby amplifying side reactions and interfacial instability.

A typical EDL comprises the inner Helmholtz plane (IHP), consisting of adsorbed ions, and the outer Helmholtz plane (OHP), formed by solvated ions (Figure 22a) [357]. This structure not only governs Li^+ desolvation kinetics but also dictates interfacial reaction pathways, SEI nucleation, and nanoscale morphology [358]. Under high-concentration electrolytes, functional additives, or elevated voltages, the EDL potential gradient, spatial configuration, and ionic coordination environment are substantially altered, thereby influencing side reactions and SEI stability [359–361]. Recent studies highlight that deliberate modulation of EDL architecture promotes the formation of dense, uniform, and stable SEI films, optimizes interfacial electric fields and Li^+ transport, suppresses dendrite growth, alleviates electrode expansion, and capacity fades [362–364].

The electrolyte itself, as both an ion-conduction medium and a chemical participant in SEI formation, exerts a decisive influence on the interfacial composition, ionic conductivity, and mechanical robustness. Current commercial and research LIB electrolytes are typically classified by salts, solvents, and additives. Among these, LiFSI and LiTFSI have demonstrated superior conductivity and stability, particularly under high-voltage and high-energy-density conditions. For example, Qian and coworkers employed a neural evolution potential model coupled with molecular dynamics simulations to probe the molecular structure and transport behavior of LiTFSI/G3 electrolytes at electrode interfaces [365]. As shown in Figure 22b, strong interactions between Li^+ and solvent oxygen atoms intensify with increasing LiTFSI concentration, leading to higher viscosity and reduced Li^+ diffusivity, which ultimately impacts interfacial ion transport and overall battery performance. Controlled tuning of the LiTFSI concentration was shown to lower interfacial migration barriers, suppress dendrite formation, and stabilize cathode materials, thereby improving cycling stability. Similarly, Santosh et al. [366] reported that full-atom molecular dynamics simulations reveal that enhanced Li^+ pectin interactions restructure the coordination environment, promote small-ion aggregate formation, and reduce Li^+ anion coordination numbers (Figure 22c). These changes significantly alter viscosity, diffusivity, and conductivity, thereby tailoring interfacial transport properties. They found that pectin not only reinforces mechanical stability but also suppresses dendrite propagation and retards interfacial impedance accumulation at the cathode. As illustrated in Figure 22d, the modulation of viscosity and ion mobility reshapes the ion distribution within the EDL, thus impacting charge-transfer kinetics. At low concentrations, ion diffusion remains comparable to that of the pristine electrolyte, preserving the EDL structure; at higher concentrations, Li^+ immobilization and anion-dominated transport collectively govern charge transfer. Moreover, as shown in Figure 22e, the Zheng group proposed a dual-additive, nonflammable ether electrolyte containing FEC and LiDFOB [367]. They demonstrated superior interfacial stability with a thin and F, B-rich cathode electrolyte interface. These findings indicate that electrolyte composition and additive chemistry reshape not only molecular solvation but also the spatial ion distribution and transport efficiency across microscale electrode architectures.

For high-voltage LMBs, interfacial asymmetry remains a central challenge: an unstable SEI at the anode induces dendrite growth, while a fragile CEI at the cathode accelerates electrolyte oxidation and transition-metal dissolution [369–373]. Conventional solvation-structure regulation alone is insufficient to stabilize both interfaces simultaneously [374–377]. Recent strategies, such as microemulsion electrolytes (Figure 22f) [368], introduce mesoscale interfacial organization to decouple SEI and CEI formation. These systems leverage interfacial tension to form LiF-rich protective layers on both electrodes, enabling stable cycling even at 4.5 V. Meanwhile, electrode surface engineering,

16146840, 2026, 26, Downloaded from https://advanced.onlinelibrary.wiley.com/doi/10.1002/aenm.71073 by Jilin University, Wiley Online Library on [07/11/2026]. See the Terms and Conditions (https://onlinelibrary.wiley.com/terms-and-conditions) on Wiley Online Library for rules of use; OA articles are governed by the applicable Creative Commons License

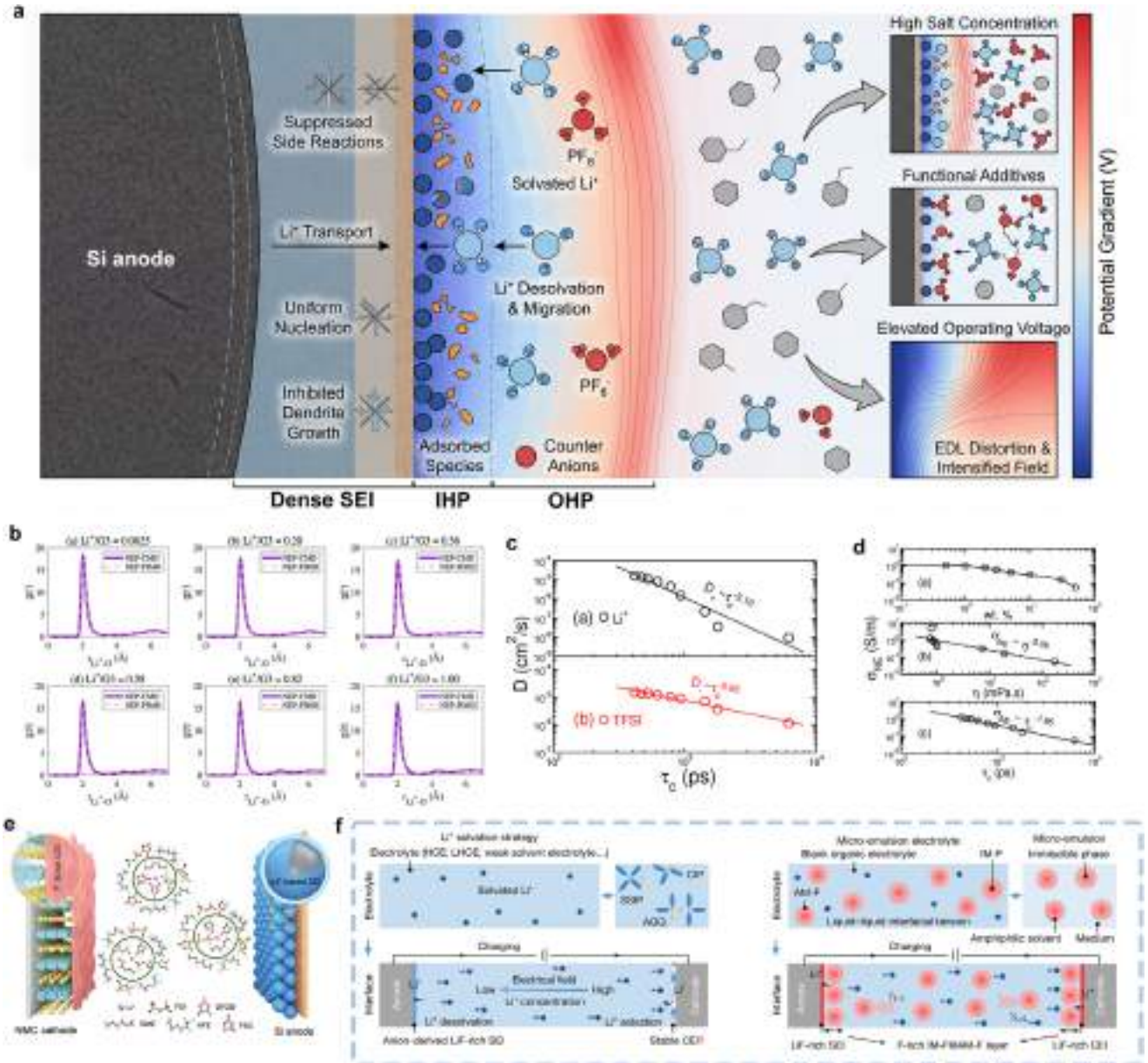


FIGURE 22 | (a) Schematic of the electrical double layer between the electrode and electrolyte. (b) Pair correlation function $g(r)$ for Li–O interactions in LiTFSI/G_3 at 300 K [365]. Copyright, American Chemical Society. (c) Correlations between the diffusion coefficient of Li^+ ions and ion-pair relaxation timescales [366]. (d) Relationship between viscosity and relaxation time [366]. Copyright, Royal Society of Chemistry. (e) F, B-rich cathode electrolyte interface induced by ether electrolyte containing FEC and LiDFOB [367]. Copyright, John Wiley & Sons, Ltd. (f) Li^+ transport behaviors and the consequent cathode and anode interphase evolution during charging with electrolyte based on the Li^+ solvation strategy [368]. Copyright, Springer Nature.

including coating and heterostructure design, further regulates wetting behavior, ion flux distribution, and interfacial reactions, reinforcing electrolyte-driven stabilization mechanisms [378–384]. As summarized in Table 5, comparative analyses of different high-voltage LMBs highlight their anode/electrolyte and electrochemical performances, offering insights into rational design principles for next-generation high-performance HVLMBs.

Collectively, microscale control of electrolyte wetting, EDL structure, and ion–electron transport establishes the critical link between interfacial chemistry and device-level performance. Under high-voltage conditions, the synergistic regulation of electrolyte composition and electrode surface structure is essential to suppress interfacial degradation, enabling stable, high-energy-density lithium-based batteries.

5.3 | Macroscale Battery Structure and System Design

While microscale regulation governs interfacial chemistry, the safety and reliability of high-voltage lithium batteries are ultimately determined at the macroscale, where electrochemical, thermal, and mechanical processes are strongly coupled and

16146840, 2026, 26, Downloaded from https://advanced.onlinelibrary.wiley.com/doi/10.1002/aenm.71073 by Jilin University, Wiley Online Library on [07/11/2026]. See the Terms and Conditions (https://onlinelibrary.wiley.com/terms-and-conditions) on Wiley Online Library for rules of use; OA articles are governed by the applicable Creative Commons License

TABLE 5 | Advanced anode and electrolyte applied in high-voltage LIBs.

Anode	Electrolyte	Cell voltage window	Cycle performance	Refs.
Cu@Si-PAN anode-free	1 M LiFSI + Py13FSI	3.2–4.7 V	80.5%@120 cycles	[385]
Cu anode-free	DME + LiFSI + HFE + LiDFOB	2.7–4.4 V	80.3%@50 cycles	[386]
Li3V2O5	1 M LiPF6 + EC + EMC	1.5–3.9 V	86.9%@1000 cycles	[387]
Cl-cHBC	1 M LiPF6 + EC + DEC	2.4–4.3 V	93.2%@150 cycles	[388]
Silicon	1 M LiPF6 + EC + DEC + DME	3.3–4.5 V	64.2%@50 cycles	[389]
Lithium	1 M LiPF6 + EC + EMC	2.5–4.8 V	80.6%@300 cycles	[390]
Lithium	0.5 M LiPF6 + 0.5 M LiDFOB + DME + TTE	3.0–4.3 V	70.2%@300 cycles	[391]
Cu anode-free	7 M LiFSI + FEC	3.3–5.0 V	88.7%@50 cycles	[392]
Lithium	Gel polymer electrolyte	3.0–4.5 V	67.4%@500 cycles	[393]
Micro-Silicon	1 M LiPF6 + FEC + SL + TTE	2.8–4.3 V	81.5%@200 cycles	[394]
Li-Sn	1 M LiPF6 + EC + DMC + EMC	2.8–4.3 V	91.5%@100 cycles	[395]

dynamically evolving. Under high-voltage operation, intensified heat generation, parasitic reactions, and mechanical stress accumulation significantly increase the risk of thermal runaway and catastrophic failure. However, conventional battery management systems (BMSs), relying on external measurements of voltage, current, and surface temperature, fail to capture these internal evolutions, leading to inaccurate state estimation and delayed safety warnings. To address this limitation, structural-functional integration has emerged as a key strategy, embedding sensing and diagnostic capabilities directly into battery architectures, thereby enabling real-time internal monitoring and intelligent safety management.

5.3.1 | Battery Sensors

Battery-integrated sensors establish a direct link between internal multiphysics processes and external control systems, which is particularly critical under high-voltage conditions where localized failure often initiates internally and propagates rapidly. Accordingly, sensing technologies have evolved from external, point-based detection toward embedded and distributed diagnostics (Figure 23a).

5.3.1.1 | Temperature Sensors. Thermal runaway in high-voltage batteries is typically initiated by localized internal heat accumulation rather than surface temperature rise. As a result, external temperature monitoring often underestimates internal hotspots, leading to delayed warning [404, 405]. In situ temperature sensing, based on thermocouples or resistance temperature detectors (RTDs) [406], enables direct monitoring of internal thermal evolution with significantly improved response speed and accuracy. Advanced designs, including thin-film and distributed sensor arrays, further allow spatially resolved temperature mapping, revealing internal thermal heterogeneity that is inaccessible to surface measurements (Figure 23b) [397, 398, 407, 408]. Nevertheless, high sensor density introduces challenges such as structural disruption and ion transport interference. Recent efforts therefore focus on optimized sensor layouts and wireless sensing strategies, which eliminate complex wiring and reduce risks associated with cell sealing, offering a scalable solution for large-format high-voltage systems [409, 410].

5.3.1.2 | Stress–Strain Sensors. Mechanical degradation is a critical yet often overlooked factor in high-voltage battery failure [411–413]. Elevated potentials accelerate volume changes, gas evolution, and interfacial instability, leading to stress accumulation, electrode cracking, and structural deformation. Embedded flexible stress–strain sensors enable direct measurement of internal mechanical evolution, revealing that internal stress is often significantly higher than external estimates [400]. Such in situ diagnostics provide early indicators of structural failure, complementing thermal monitoring and improving the accuracy of safety prediction under high-voltage operation (Figure 23c) [396, 399, 400].

5.3.1.3 | Optical Sensors. Optical sensing offers a powerful alternative for high-resolution and distributed diagnostics, particularly suited for high-voltage systems where electromagnetic interference and wiring complexity become critical concerns [414]. Fiber-based sensors, including fiber Bragg gratings (FBGs) and distributed optical fiber sensing (DOFS), enable multipoint or continuous monitoring of temperature and strain with high spatial resolution. These systems can capture internal gradients and dynamic evolution across the entire cell, overcoming the limitations of conventional point sensors. Importantly, advanced optical architectures demonstrate strong resistance to extreme conditions, enabling real-time monitoring even during thermal runaway (Figure 23d) [401, 402, 415]. This robustness provides a foundation for next-generation intelligent battery systems capable of both surviving and diagnosing failure events under high-voltage operation [403, 416–420].

Importantly, beyond the sensing capability itself, a critical yet underexplored challenge lies in the manufacturability and integration of these sensors within high-voltage battery systems. Unlike conventional configurations, high-voltage electrodes are highly sensitive to microstructural and interfacial perturbations,

16146840, 2026, 26, Downloaded from https://advanced.onlinelibrary.wiley.com/doi/10.1002/aenm.71073 by Jilin University, Wiley Online Library on [07/11/2026]. See the Terms and Conditions (https://onlinelibrary.wiley.com/terms-and-conditions) on Wiley Online Library for rules of use; OA articles are governed by the applicable Creative Commons License

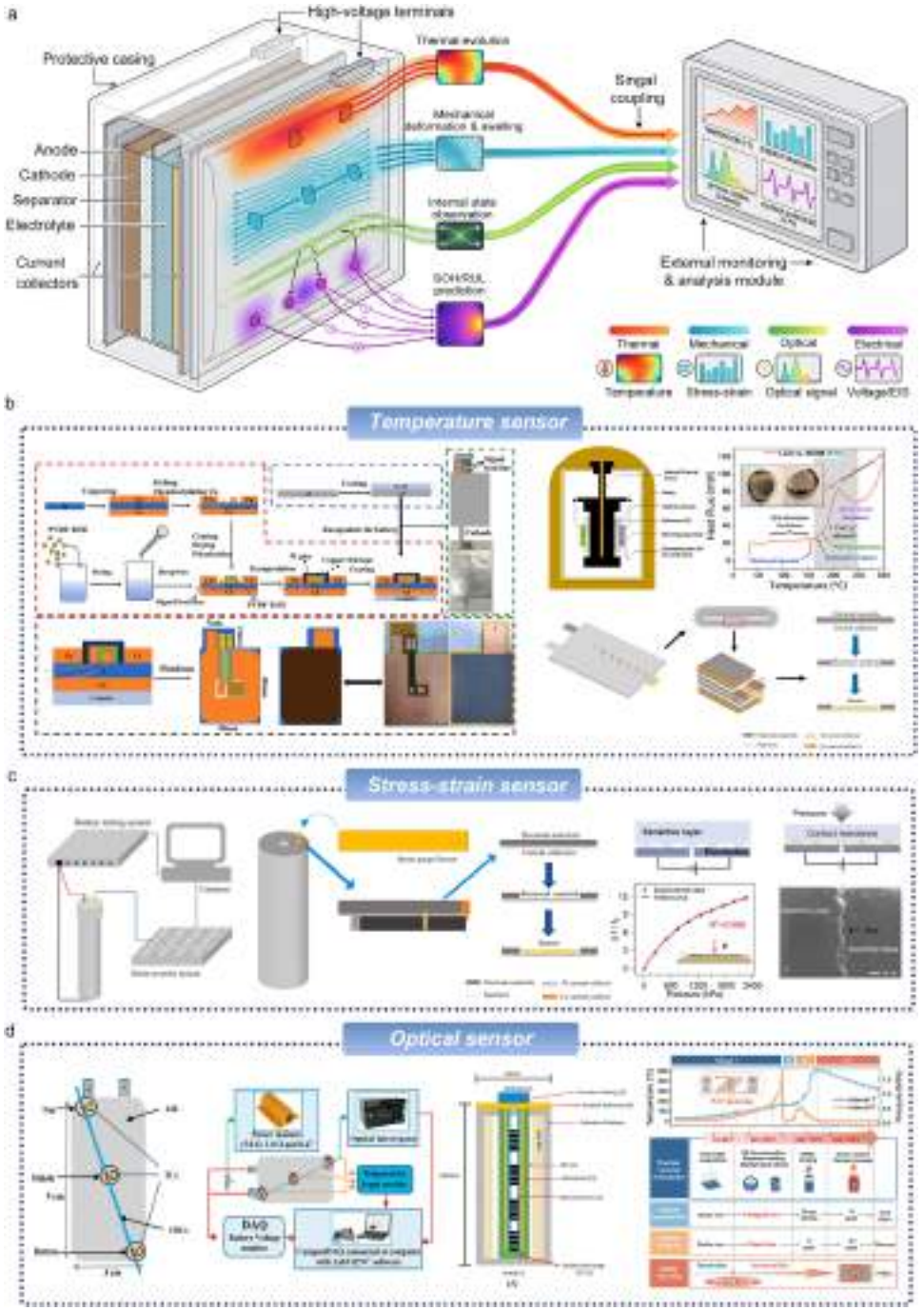


FIGURE 23 | (a) Schematic diagram of multiscale sensors for HVLIBs. (b) Different temperature sensors with polymer-based operation [396], implanted operation [397], and distributed array operation [398]. Copyright, Elsevier. (c) Stress–strain sensor with 18650 LIB [399] and the operating mechanism between pressures and current output [400], Copyright, Elsevier. (d) Different optical sensors with locations of TCs and FBGs [401], instrumented cells [402], and elucidation of thermal-runaway pathways for HVLIBs [403]. Copyright, Elsevier.

where even minor disruption to particle/electrolyte contact or ion transport pathways can accelerate degradation under elevated potentials. Therefore, the integration of sensors must be carefully aligned with advanced fabrication processes to avoid compromising electrochemical performance. For example, emerging dry electrode processing and calendaring techniques provide opportunities to embed ultrathin, flexible sensors directly into electrode architectures without introducing solvent-induced defects or interfacial inhomogeneity. Similarly, in high-voltage-compatible, nondestructive packaging processes, sensor incorporation must preserve electrode integrity, maintain uniform pressure distribution, and avoid creating localized electronic or ionic discontinuities. These considerations highlight that sensor integration is not merely a functional addition but a process-dependent design challenge that must balance sensing fidelity with interfacial stability and energy density retention.

16146840, 2026, 26, Downloaded from https://advanced.onlinelibrary.wiley.com/doi/10.1002/aenm.71073 by Jilin University, Wiley Online Library on [07/11/2026]. See the Terms and Conditions (https://onlinelibrary.wiley.com/terms-and-conditions) on Wiley Online Library for rules of use; OA articles are governed by the applicable Creative Commons License

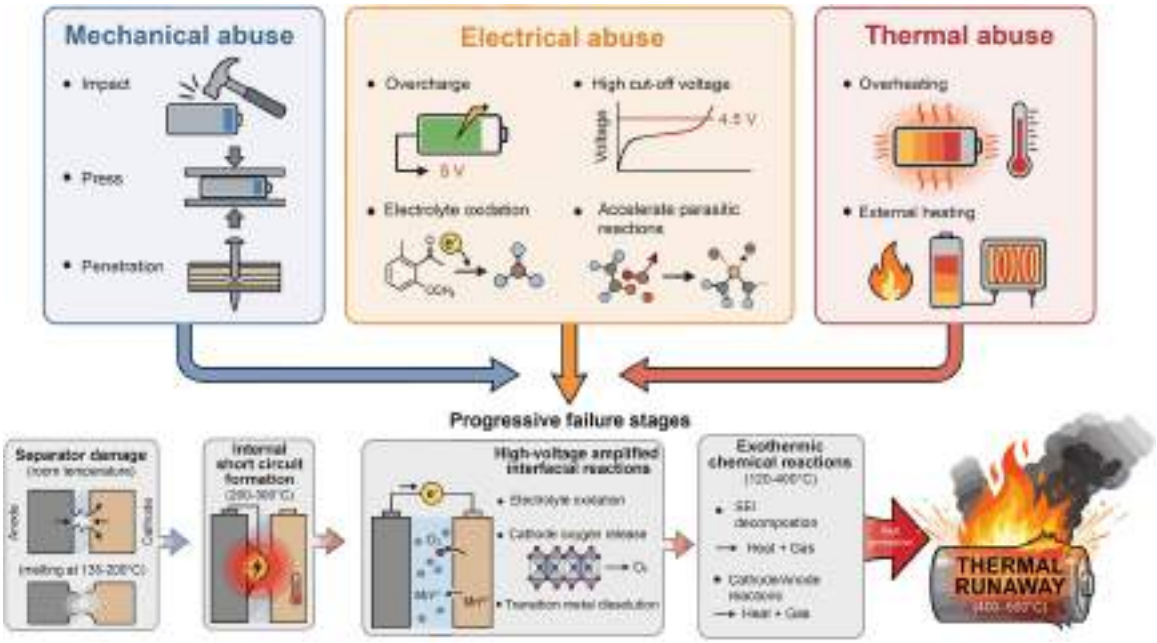


FIGURE 24 | Schematic of the thermal runaway mechanism for the energy storage system.

5.3.2 | Intelligent Management Systems for Thermal Runaways

Under high-voltage operation, thermal runaway is no longer a purely thermal or mechanical failure but is fundamentally initiated by electrochemical instability at highly delithiated states. Specifically, deep delithiation of high-nickel cathodes at elevated voltages triggers lattice oxygen release, while severe electrolyte oxidation at high potentials generates heat, gas, and reactive intermediates. These processes collectively accelerate interfacial degradation, gas evolution, and internal pressure buildup, ultimately initiating chain reactions that lead to thermal runaway (Figure 24) [421].

Conventional BMSs, relying on voltage, current, and surface temperature, cannot capture these early-stage internal electrochemical failures, rendering high-voltage batteries particularly vulnerable to delayed warning. To address this limitation, embedded multiphysics sensing has emerged as a key strategy for the early detection of high-voltage-induced instability [422]. For example, distributed potential sensing enables spatial mapping of internal electrochemical heterogeneity, allowing early identification of localized overpotential and degradation sites. In parallel, gas sensing provides direct evidence of high-voltage interfacial reactions: CO_2 evolution is closely associated with cathode oxidation, while H_2 and hydrocarbon species reflect electrolyte decomposition and SEI breakdown. Notably, gas generation often precedes a detectable temperature rise, making it a highly sensitive indicator of high-voltage failure initiation [423, 424]. Based on this, Lee et al. fabricated an ultrathin (50 nm) MEMS-based H_2 sensor on a flexible polyimide substrate. The device detects internal hydrogen leakage through rapid resistance shifts.

Mechanical sensing further complements this framework. High-voltage cycling intensifies volume fluctuation, gas accumulation, and internal stress evolution, which are strongly coupled with interfacial degradation. Embedded strain sensors, therefore, provide early warning signals of structural failure that are inaccessible to external measurements. Collectively, these sensing strategies transform safety management from passive monitoring to proactive diagnosis, enabling early identification of high-voltage triggered interfacial failure and extending the intervention window before thermal runaway.

5.3.3 | Battery Protection for Thermal Runaway

Given that high-voltage operation accelerates heat generation and gas evolution, effective structural protection must be designed to mitigate both thermal propagation and pressure-driven failure. The thermal runaway behavior of batteries is strongly dependent on the cell configuration, which governs heat dissipation, mechanical confinement, and gas release pathways.

Cylindrical cells, featuring metallic casings and radially symmetric heat distribution, show superior thermal conductivity per unit volume. However, their dense packing can hinder lateral thermal isolation and accelerate intercell heat transfer. Prismatic cells offer a compact geometry and high integration density but suffer from nonuniform internal pressure and localized heat concentration, which can intensify hotspot formation and thermal diffusion. In contrast, pouch cells constructed with laminated aluminum-polymer films possess favorable heat dissipation yet poor mechanical robustness, making them prone to rupture and jet-like venting once internal pressure surges during thermal runaway.

To address these challenges, integrated porous heat-dissipation channels have been introduced in advanced cell designs. By introducing microventilation layers, these architectures enhance longitudinal heat conduction while suppressing lateral thermal

16146840, 2026, 26, Downloaded from https://advanced.onlinelibrary.wiley.com/doi/10.1002/aenm.71073 by Jilin University, Wiley Online Library on [07/11/2026]. See the Terms and Conditions (https://onlinelibrary.wiley.com/terms-and-conditions) on Wiley Online Library for rules of use; OA articles are governed by the applicable Creative Commons License

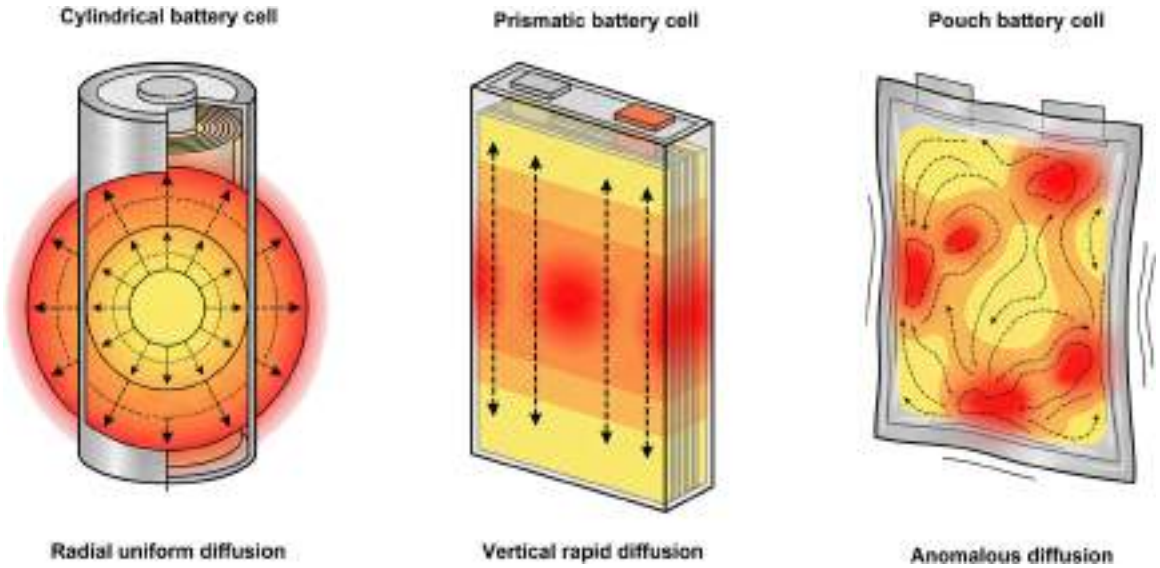


FIGURE 25 | Schematic of thermal diffusion pathways of three types of cells under runaway conditions.

propagation. Figure 25 compares the thermal diffusion pathways of different cell formats under runaway conditions. Thermal isolation barriers represent another cornerstone of battery safety engineering, aiming to physically decouple heat and reactive materials. Conventional approaches insert low-conductivity, high heat-capacity layers, such as ceramic fiber mats, silicone-based pads, or inorganic mineral composites, between cells or along module boundaries to delay heat transfer and block propagation. Crucially, high-voltage operation demands simultaneous management of heat and gas. Therefore, optimized designs incorporate pressure relief and gas venting channels to safely release high-temperature gaseous products generated from electrolyte oxidation and cathode decomposition.

When integrated with intelligent sensing systems, these structural strategies establish a multilayer safety framework that directly targets high-voltage-induced failure mechanisms, enabling early detection, localized suppression, and controlled propagation of thermal runaway.

6 | Summary and Outlook

In this review, we comprehensively examine the critical challenges, fabrication technologies, and multiscale coupling mechanisms governing the performance of HVLIBs. Particular emphasis has been placed on the intricate interplay between structural instability, interfacial chemistry, and electrochemical dynamics, which jointly determine the safety and efficiency of high-energy systems.

At the material level, the development of robust high-voltage cathodes and compatible electrolytes remains a central priority. Despite significant advances in composition tuning, surface modification, and interface engineering, balancing high-voltage stability with ionic conductivity and mechanical integrity persists as an enduring challenge. At the mesoscale, the optimization of electrode–electrolyte architectures, specifically through graded porosity, enhanced wettability, and interconnected ion or electron transport pathways, has proven critical for enabling fast charge transfer and mitigating localized polarization. Furthermore, the emergence of solid-state batteries further highlights the importance of intimate interfacial contact and chemically stable interphases, as mechanical and electrochemical mismatches at solid–solid boundaries often dominate failure pathways. To overcome these issues, hybrid electrolytes, buffer interlayers, and molecularly engineered interfaces have been demonstrated to promote uniform ion flux and suppress dendrite growth, representing promising routes toward durable and safe high-voltage operation.

On the device and system levels, the fabrication and packaging technologies for high-voltage cells have evolved toward lightweight, modular, and eco-friendly designs. Advanced sealing materials and thermal management architectures have been integrated to improve the energy density and cycling reliability. The increasing complexity of large-scale battery packs introduces new challenges in real-time monitoring and fault diagnosis. To tackle these complexities, the integration of structural-functional intelligent management systems represents a transformative approach. By embedding multidimensional sensors (thermal, mechanical, and optical) within the battery structure, such systems enable in situ monitoring of internal temperature, stress, and chemical evolution. Coupled with advanced signal-processing and data-fusion algorithms, these intelligent management systems allow for the accurate estimation of key operational states, including SOC, SOH, and SOP, while offering early warnings against thermal runaway and mechanical failure. The convergence of sensor technology, data analytics, and materials design marks a pivotal step toward the autonomous operation of energy storage systems with enhanced safety and resilience. To further highlight the central concept of preparation-dependent multiscale coupling, the relationships between fabrication strategies, structural descriptors, and their corresponding physicochemical mechanisms and electrochemical performance are summarized in Table 6.

16146840, 2026, 26, Downloaded from https://advanced.onlinelibrary.wiley.com/doi/10.1002/aenm.71073 by Jilin University, Wiley Online Library on [07/11/2026]. See the Terms and Conditions (https://onlinelibrary.wiley.com/terms-and-conditions) on Wiley Online Library for rules of use; OA articles are governed by the applicable Creative Commons License

TABLE 6 | Preparation-dependent multiscale coupling in high-voltage lithium-ion batteries.

Preparation strategy	Multiscale structural descriptors	Dominant physicochemical mechanisms	Impact on electrochemical performance	Representative systems
Slurry casting and calendaring	Random particle packing; high tortuosity (micro); weak interparticle contact (nano)	Nonuniform ion transport; stress concentration; unstable SEI/CEI	Limited rate capability; accelerated degradation	Conventional thick electrodes
Advanced binders and conductive networks	Strong interparticle adhesion (nano); elastic/conductive network (micro)	Stress buffering; continuous electron pathways; stabilized interfaces	Improved cycling stability and capacity retention	Si-based anodes with functional binders
Surface coating	Conformal protective layers; regulated surface chemistry (nano)	Suppressed parasitic reactions; stabilized CEI/SEI; reduced TM dissolution	Enhanced high-voltage stability and lifespan	Oxide/fluoride/phosphate coatings on NCM/LCO cathode
In situ polymerization	Conformal interfacial polymer network; intimate electrode–electrolyte contact (nano–micro)	Reduced interfacial resistance; uniform Li^+ flux; stabilized interphase formation	Improved interfacial compatibility and cycling stability	In situ formed polymer electrolytes
3D printing	Ordered architectures; low tortuosity channels (micro–macro)	Accelerated ion/electron transport; reduced polarization	High areal capacity; improved rate performance	3D-printed LFP/LTO electrodes
Phase separation	Aligned pore channels; gradient structures (micro)	Homogeneous ion distribution; reduced concentration polarization	Enhanced thick-electrode performance	Vertically aligned LCO electrodes
Freeze-casting	Directional channels; hierarchical porosity (micro–macro)	Fast ion transport; stress redistribution; uniform reaction fronts	High loading capability with stable cycling	Ice-templated LFP/NCM electrodes
Electrolyte engineering	Modified solvation structure; tailored interphase chemistry (nano)	Controlled decomposition pathways; stable SEI/CEI formation	Improved high-voltage stability	HCE/LHCE/WSE electrolytes
Artificial interphase design	Dense, ion-conductive interphase layers (nano)	Suppressed dendrite growth; regulated Li^+ transport	Enhanced safety and cycling life	LiF-rich SEI, ALD coatings
Sensor-integrated systems	Embedded sensing network (macro)	Real-time monitoring of thermal/mechanical/electrochemical states	Improved safety, diagnostics, and reliability	FBG/RTD-based smart batteries

Looking ahead, several research directions merit intensified efforts. First, the atomic-scale design of cathode-electrolyte interfaces guided by ab initio calculations, in situ spectroscopy, and machine-learning-driven material discovery will accelerate the identification of high-voltage-compatible chemistries. Second, multiphysics modeling and digital twins would be further developed to correlate electrochemical, thermal and mechanical processes across scales, enabling predictive optimization from materials to system integration. Third, the synergistic combination of solid-state and liquid-phase hybrid electrolytes, coupled with scalable manufacturing technologies, offers a viable pathway to balance ionic conductivity, safety, and cost. Finally, data-driven intelligent management leveraging machine learning and real-time sensing will redefine battery diagnostics, transitioning from passive monitoring to active control and self-adaptive optimization (Figure 26).

16146840, 2026, 26, Downloaded from https://advanced.onlinelibrary.wiley.com/doi/10.1002/aenm.71073 by Jilin University, Wiley Online Library on [07/11/2026]. See the Terms and Conditions (https://onlinelibrary.wiley.com/terms-and-conditions) on Wiley Online Library for rules of use; OA articles are governed by the applicable Creative Commons License

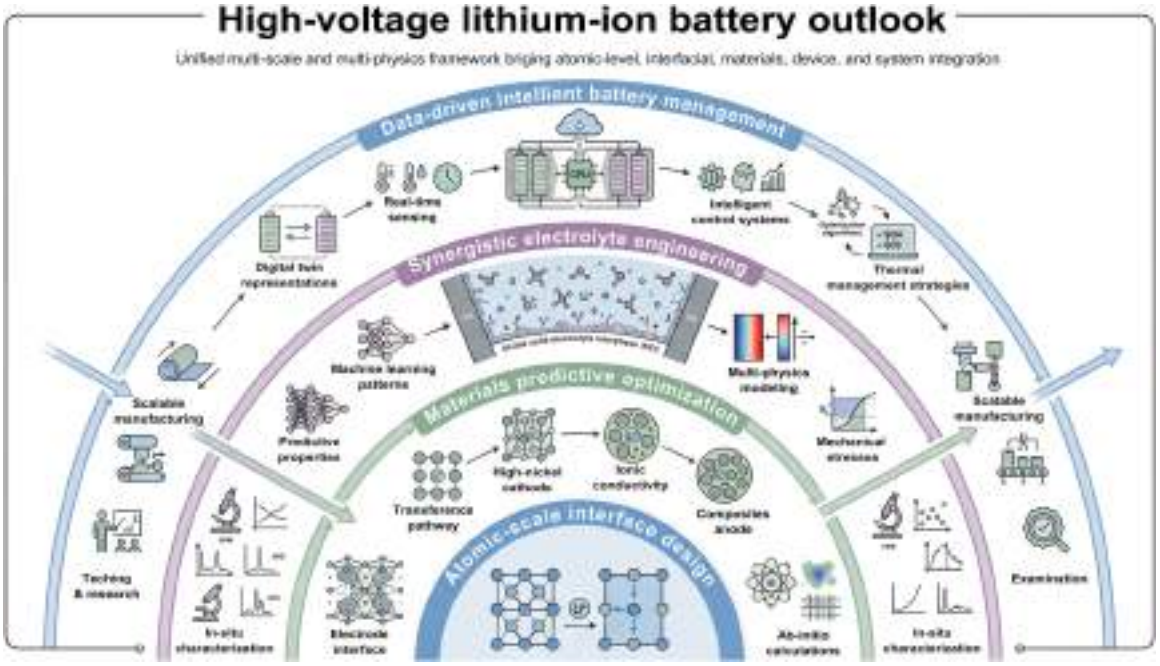


FIGURE 26 | Outlook for next-generation high-voltage lithium-ion batteries.

In conclusion, the development of next-generation high-voltage lithium-ion batteries demands a paradigm that transcends conventional trade-offs between energy density, safety, and intelligence. Through the coordinated progress of materials innovation, structural engineering, and system-level intelligence, the future of high-voltage energy storage is expected to shift from "high-energy" to "high-performance", delivering safer, smarter, and more sustainable batteries for the electrified world.

Acknowledgements

This work was supported by the National Science Foundation of China (No. 52372228), Yibin Science and Technology Innovation Seeding Project (No. 2025MZ009), and Fundamental Research Funds for the Central Universities (No. 2682026CX250).

Conflicts of Interest

The authors declare no conflicts of interest.

Data Availability Statement

The data that support the findings of this study are available from the corresponding author upon reasonable request.

References

1. J. Liu, Z. Bao, Y. Cui, et al., "Pathways for Practical High-energy Long-cycling Lithium Metal Batteries," *Nature Energy* 4 (2019): 180–186, https://doi.org/10.1038/s41560-019-0338-x.

2. F. Wu, S. Fang, M. Kuenzel, et al., "Dual-anion Ionic Liquid Electrolyte Enables Stable Ni-rich Cathodes in Lithium-metal Batteries," *Joule* 5 (2021): 2177–2194, https://doi.org/10.1016/j.joule.2021.06.014.

3. Q. Li, D. Zhou, M. Chu, et al., "A Comprehensive Understanding on the Anionic Redox Chemistry of High-voltage Cathode Materials for High-energy-density Lithium-ion Batteries," *Chemical Society Reviews* 54 (2025): 3441–3474, https://doi.org/10.1039/D4CS00797B.

4. L. Wang, Y. Qiu, W. Yuan, Y. Tian, and Z. Zhou, "Next-generation Battery Safety Management: Machine Learning Assisted Life-time Prediction and Performance Enhancement," *Journal of Energy Chemistry* 109 (2025): 726–739, https://doi.org/10.1016/j.jechem.2025.05.065.

5. K. Yang, L. Zhang, W. Wang, et al., "Multiscale Modeling for Enhanced Battery Health Analysis: Pathways to Longevity," *Carbon Neutralization* 3 (2024): 348–385, https://doi.org/10.1002/cnl2.124.

6. W. Liu, J. Li, W. Li, H. Xu, C. Zhang, and X. Qiu, "Inhibition of Transition Metals Dissolution in Cobalt-free Cathode with Ultrathin Robust Interphase in Concentrated Electrolyte," *Nature Communications* 11 (2020): 3629, https://doi.org/10.1038/s41467-020-17396-x.

7. R. Sim, L. Su, A. Dolocan, and A. Manthiram, "Delineating the Impact of Transition-Metal Crossover on Solid-Electrolyte Interphase Formation with Ion Mass Spectrometry," *Advanced Materials* 36 (2024): 2311573, https://doi.org/10.1002/adma.202311573.

8. M. Mao, L. Gong, X. Wang, et al., "Electrolyte Design Combining Fluoro- with Cyano-substitution Solvents for Anode-free Li Metal Batteries," *Proceedings of the National Academy of Sciences* 121 (2024): 2316212121, https://doi.org/10.1073/pnas.2316212121.

9. S. Wiemers-Meyer, S. Jeremias, M. Winter, and S. Nowak, "Influence of Battery Cell Components and Water on the Thermal and Chemical Stability of LiPF6 Based Lithium Ion Battery Electrolytes," *Electrochimica Acta* 222 (2016): 1267–1271, https://doi.org/10.1016/j.electacta.2016.11.100.

10. Y. Yu, P. Karayaylali, Y. Katayama, et al., "Coupled LiPF 6 Decomposition and Carbonate Dehydrogenation Enhanced by Highly Covalent Metal Oxides in High-Energy Li-Ion Batteries," *The Journal of Physical Chemistry C* 122 (2018): 27368–27382, https://doi.org/10.1021/acs.jpcc.8b07848.

11. S. Tan, Z. Shadike, J. Li, et al., "Additive Engineering for Robust Interphases to Stabilize High-Ni Layered Structures at ultrahIgh Voltage of 4.8 V," *Nature Energy* 7 (2022): 484–494, https://doi.org/10.1038/s41560-022-01020-x.

12. K. Mizushima, P. C. Jones, P. J. Wiseman, and J. B. Goodenough, "LixCoO2 (0<x<-1): A New Cathode Material for Batteries of High Energy Density," *Materials Research Bulletin* 15 (1980): 783–789, https://doi.org/10.1016/0025-5408(80)90012-4.

16146840, 2026, 26, Downloaded from https://advanced.onlinelibrary.wiley.com/doi/10.1002/aenm.71073 by Jilin University, Wiley Online Library on [07/11/2026]. See the Terms and Conditions (https://onlinelibrary.wiley.com/terms-and-conditions) on Wiley Online Library for rules of use; OA articles are governed by the applicable Creative Commons License

13. J. N. Reimers and J. R. Dahn, "Electrochemical and in Situ X-Ray Diffraction Studies of Lithium Intercalation in Li_x CoO_2," *Journal of The Electrochemical Society* 139 (1992): 2091, https://doi.org/10.1149/1.2221184.

14. X. Lu, Y. Sun, Z. Jian, et al., "New Insight into the Atomic Structure of Electrochemically Delithiated O3-$Li_{(1-x)}$ CoO_2 ($0 \leq x \leq 0.5$) Nanoparticles," *Nano Letters* 12 (2012): 6192–6197, https://doi.org/10.1021/nl303036e.

15. X. Hou, X. Liu, H. Wang, X. Zhang, J. Zhou, and M. Wang, "Specific Countermeasures to Intrinsic Capacity Decline Issues and Future Direction of $LiMn_2O_4$ Cathode," *Energy Storage Materials* 57 (2023): 577–606, https://doi.org/10.1016/j.ensm.2023.02.015.

16. J. Zheng, G. Teng, C. Xin, et al., "Role of Superexchange Interaction on Tuning of Ni/Li Disordering in Layered $Li(Ni_xMn_yCo_z)O_2$," *The Journal of Physical Chemistry Letters* 8 (2017): 5537–5542, https://doi.org/10.1021/acs.jpclett.7b02498.

17. C. Xu, P. J. Reeves, Q. Jacquet, and C. P. Gray, "Phase Behavior during Electrochemical Cycling of Ni-Rich Cathode Materials for Li-Ion Batteries," *Advanced Energy Materials* 11 (2021): 2003404, https://doi.org/10.1002/aenm.202003404.

18. M. M. Thackeray, W. I. F. David, P. G. Bruce, and J. B. Goodenough, "Lithium Insertion into Manganese Spinels," *Materials Research Bulletin* 18 (1983): 461–472, https://doi.org/10.1016/0025-5408(83)90138-1.

19. S. Liu, B. Wang, X. Zhang, S. Zhao, Z. Zhang, and H. Yu, "Reviving the Lithium-manganese-based Layered Oxide Cathodes for Lithium-ion Batteries," *Matter* 4 (2021): 1511–1527, https://doi.org/10.1016/j.matt.2021.02.023.

20. C. Zhan, T. Wu, J. Lu, and K. Amine, "Dissolution, Migration, and Deposition of Transition Metal Ions in Li-ion Batteries Exemplified by Mn-based Cathodes—A Critical Review," *Energy & Environmental Science* 11 (2018): 243–257, https://doi.org/10.1039/C7EE03122J.

21. A. Banerjee, Y. Shilina, B. Ziv, et al., "On the Oxidation State of Manganese Ions in Li-Ion Battery Electrolyte Solutions," *Journal of the American Chemical Society* 139 (2017): 1738–1741, https://doi.org/10.1021/jacs.6b10781.

22. X. Gao, Y. H. Ikuhara, C. A. J. Fisher, et al., "Oxygen Loss and Surface Degradation during Electrochemical Cycling of Lithium-ion Battery Cathode Material LiMn 2° 4," *Journal of Materials Chemistry A* 7 (2019): 8845–8854, https://doi.org/10.1039/C8TA08083F.

23. A. Boulineau, L. Simonin, J.-F. Colin, C. Bourbon, and S. Patoux, "First Evidence of Manganese–Nickel Segregation and Densification Upon Cycling in Li-Rich Layered Oxides for Lithium Batteries," *Nano Letters* 13 (2013): 3857–3863, https://doi.org/10.1021/nl4019275.

24. J. Sun, C. Sheng, X. Cao, et al., "Restraining Oxygen Release and Suppressing Structure Distortion in Single-Crystal Li-Rich Layered Cathode Materials," *Advanced Functional Materials* 32 (2022): 2110295, https://doi.org/10.1002/adfm.202110295.

25. X. Wang, Y.-L. Ding, Y.-P. Deng, and Z. Chen, "Ni-Rich/Co-Poor Layered Cathode for Automotive Li-Ion Batteries: Promises and Challenges," *Advanced Energy Materials* 10 (2020): 1903864, https://doi.org/10.1002/aenm.201903864.

26. P. Y. Liao, J. G. Duh, and S. R. Sheen, "Effect of Mn Content on the Microstructure and Electrochemical Performance of $LiNi_{0.75-x}$ $Co_{0.25}Mnx$ O_2 Cathode Materials," *Journal of The Electrochemical Society* 152 (2005): A1695, https://doi.org/10.1149/1.1952687.

27. H.-H. Sun and A. Manthiram, "Impact of Microcrack Generation and Surface Degradation on a Nickel-Rich Layered $Li[Ni_{0.9}$ $Co_{0.05}$ $Mn_{0.05}]O_2$ Cathode for Lithium-Ion Batteries," *Chemistry of Materials* 29 (2017): 8486–8493, https://doi.org/10.1021/acs.chemmater.7b03268.

28. J. Lee, A. Urban, X. Li, D. Su, G. Hautier, and G. Ceder, "Unlocking the Potential of Cation-Disordered Oxides for Rechargeable Lithium Batteries," *Science* 343 (2014): 519–522, https://doi.org/10.1126/science.1246432.

29. C. Delmas, J. P. Pérès, A. Rougier, et al., "On the Behavior of the $LixNiO_2$ System: an Electrochemical and Structural Overview," *Journal of Power Sources* 68 (1997): 120–125, https://doi.org/10.1016/S0378-7753(97)02664-5.

30. C. Delmas, C. Fouassier, and P. Hagenmuller, "Structural Classification and Properties of the Layered Oxides," *Physica B+C* 99 (1980): 81–85, https://doi.org/10.1016/0378-4363(80)90214-4.

31. A. Van der Ven, M. K. Aydinol, and G. Ceder, "First-Principles Evidence for Stage Ordering in Li_x CoO_2," *Journal of The Electrochemical Society* 145 (1998): 2149–2155, https://doi.org/10.1149/1.1838610.

32. Z. Chen, Z. Lu, and J. R. Dahn, "Staging Phase Transitions in Li_x CoO_2," *Journal of The Electrochemical Society* 149 (2002): A1604, https://doi.org/10.1149/1.1519850.

33. K. Märker, P. J. Reeves, C. Xu, K. J. Griffith, and C. P. Gray, "Evolution of Structure and Lithium Dynamics in $LiNi_{0.8}$ $Mn_{0.1}$ $Co_{0.1}$ O_2 (NMC811) Cathodes during Electrochemical Cycling," *Chemistry of Materials* 31 (2019): 2545–2554, https://doi.org/10.1021/acs.chemmater.9b00140.

34. H.-H. Ryu, K.-J. Park, C. S. Yoon, and Y.-K. Sun, "Capacity Fading of Ni-Rich $Li[Ni_x$ Co_y $Mn_{1-x-y}]O_2$ ($0.6 \leq x \leq 0.95$) Cathodes for High-Energy-Density Lithium-Ion Batteries: Bulk or Surface Degradation?," *Chemistry of Materials* 30 (2018): 1155–1163, https://doi.org/10.1021/acs.chemmater.7b05269.

35. U.-H. Kim, N.-Y. Park, G.-T. Park, H. Kim, C. S. Yoon, and Y.-K. Sun, "High-Energy W-Doped $Li[Ni_{0.95}Co_{0.04}Al_{0.01}]O_2$ Cathodes for Next-Generation Electric Vehicles," *Energy Storage Materials* 33 (2020): 399–407, https://doi.org/10.1016/j.ensm.2020.08.013.

36. H. Li, A. Liu, N. Zhang, et al., "An Unavoidable Challenge for Ni-Rich Positive Electrode Materials for Lithium-Ion Batteries," *Chemistry of Materials* 31 (2019): 7574–7583, https://doi.org/10.1021/acs.chemmater.9b02372.

37. Z. Yang, Y. Jia, Y. Liu, et al., "Interfacial Modulation for Anti-Disproportionation in Zr-Nb-Fe-Ni Based Hydrogen Isotope Storage Alloys Driven by Product Destabilization Strategy," *Advanced Materials* 38 (2026): 23063, https://doi.org/10.1002/adma.202523063.

38. K. Xu, "Interfaces and Interphases in Batteries," *Journal of Power Sources* 559 (2023): 232652, https://doi.org/10.1016/j.jpowsour.2023.232652.

39. J. B. Goodenough and K.-S. Park, "The Li-Ion Rechargeable Battery: a Perspective," *Journal of the American Chemical Society* 135 (2013): 1167–1176, https://doi.org/10.1021/ja3091438.

40. Z. C. Zhang, L. B. Hu, H. M. Wu, et al., "Fluorinated Electrolytes for 5 V Lithium-ion Battery Chemistry," *Energy & Environmental Science* 6 (2013): 1806–1810, https://doi.org/10.1039/c3ee24414h.

41. L. Xing, O. Borodin, G. D. Smith, and W. Li, "Density Functional Theory Study of the Role of Anions on the Oxidative Decomposition Reaction of Propylene Carbonate," *The Journal of Physical Chemistry A* 115 (2011): 13896–13905, https://doi.org/10.1021/jp206153n.

42. B. L. D. Rinkel, J. P. Vivek, N. Garcia-Araez, and C. P. Gray, "Two Electrolyte Decomposition Pathways at Nickel-rich Cathode Surfaces in Lithium-ion Batteries," *Energy & Environmental Science* 15 (2022): 3416–3438, https://doi.org/10.1039/d1ee04053g.

43. J. Wandt, A. T. S. Freiberg, A. Ogrodnik, and H. A. Gasteiger, "Singlet Oxygen Evolution from Layered Transition Metal Oxide Cathode Materials and Its Implications for Lithium-ion Batteries," *Materials Today* 21 (2018): 825–833, https://doi.org/10.1016/j.mattod.2018.03.037.

44. C. Wang, L. Xing, J. Vatamanu, et al., "Overlooked Electrolyte Destabilization by Manganese (II) in Lithium-ion Batteries," *Nature Communications* 10 (2019): 3423, https://doi.org/10.1038/s41467-019-11439-8.

45. R. Sahore, D. C. O'Hanlon, A. Tornheim, et al., "Revisiting the Mechanism behind Transition-Metal Dissolution from Delithiated $LiNi_x$ Mn_y Co_z O_2 (NMC) Cathodes," *Journal of The Electrochemical Society* 167 (2020): 020513, https://doi.org/10.1149/1945-7111/ab6826.

16146840, 2026, 26, Downloaded from https://advanced.onlinelibrary.wiley.com/doi/10.1002/aenm.71073 by Jilin University, Wiley Online Library on [07/11/2026]. See the Terms and Conditions (https://onlinelibrary.wiley.com/terms-and-conditions) on Wiley Online Library for rules of use; OA articles are governed by the applicable Creative Commons License

46. R. C. McNulty, K. D. Jones, B. M. G. Denison, et al., "Singlet Oxygen Is Not the Source of Ethylene Carbonate Degradation in Nickel-rich Li-ion Cells," *Energy & Environmental Science* 18 (2025): 7603–7609, https://doi.org/10.1039/D5EE00956A.

47. J. L. Tebbe, T. F. Fuerst, and C. B. Musgrave, "Degradation of Ethylene Carbonate Electrolytes of Lithium Ion Batteries via Ring Opening Activated by $LiCoO_2$ Cathode Surfaces and Electrolyte Species," *ACS Applied Materials & Interfaces* 8 (2016): 26664–26674, https://doi.org/10.1021/acsami.6b06157.

48. R. Jung, M. Metzger, F. Maglia, C. Stinner, and H. A. Gasteiger, "Oxygen Release and Its Effect on the Cycling Stability of $LiNi_xMn_yCo_zO_2$ (NMC) Cathode Materials for Li-Ion Batteries," *Journal of The Electrochemical Society* 164 (2017): A1361, https://doi.org/10.1149/2.0021707jes.

49. F. Lin, I. M. Markus, D. Nordlund, et al., "Surface Reconstruction and Chemical Evolution of Stoichiometric Layered Cathode Materials for Lithium-ion Batteries," *Nature Communications* 5 (2014): 3529, https://doi.org/10.1038/ncomms4529.

50. L. Yao, Y. Li, X. Gao, et al., "Microstructure Boosting the Cycling Stability of $LiNi_{0.6}Co_{0.2}Mn_{0.2}O_2$ Cathode through Zr-based Dual Modification," *Energy Storage Materials* 36 (2021): 179–185, https://doi.org/10.1016/j.ensm.2020.12.026.

51. S.-K. Jung, H. Gwon, J. Hong, et al., "Understanding the Degradation Mechanisms of $LiNi_{0.5}Co_{0.2}Mn_{0.3}O_2$ Cathode Material in Lithium Ion Batteries," *Advanced Energy Materials* 4 (2014): 1300787, https://doi.org/10.1002/aenm.201300787.

52. L. Wang, G. Liu, R. Xu, et al., "Enabling an Intrinsically Safe and High-Energy-Density 4.5 V-Class Lithium-Ion Battery with Synergistically Incorporated Fast Ion Conductors," *Advanced Energy Materials* 13 (2023): 2203999, https://doi.org/10.1002/aenm.202203999.

53. A. Manthiram, B. Song, and W. Li, "A Perspective on Nickel-rich Layered Oxide Cathodes for Lithium-ion Batteries," *Energy Storage Materials* 6 (2017): 125–139, https://doi.org/10.1016/j.ensm.2016.10.007.

54. W. Zuo, J. Gim, T. Li, et al., "Microstrain Screening Toward Defectless Layered Transition Metal Oxide Cathodes," *Nature Nanotechnology* 19 (2024): 1644–1653, https://doi.org/10.1038/s41565-024-01734-x.

55. W. Liu, P. Oh, X. Liu, et al., "Nickel-Rich Layered Lithium Transition-Metal Oxide for High-Energy Lithium-Ion Batteries," *Angewandte Chemie International Edition* 54 (2015): 4440–4457, https://doi.org/10.1002/anie.201409262.

56. M. Song, D. Lee, J. Kim, et al., "Gas Evolution Kinetics in Overlithiated Positive Electrodes and Its Impact on Electrode Design," *Advanced Science* 11 (2024): 2400568, https://doi.org/10.1002/advs.202400568.

57. J. Dong, F. Wu, J. Zhao, et al., "Multifunctional Self-reconstructive Cathode/Electrolyte Interphase Layer for Cobalt-free Li-rich Layered Oxide Cathode," *Energy Storage Materials* 60 (2023): 102798, https://doi.org/10.1016/j.ensm.2023.102798.

58. B. Jagger and M. Pasta, "Solid Electrolyte Interphases in Lithium Metal Batteries," *Joule* 7 (2023): 2228–2244, https://doi.org/10.1016/j.joule.2023.08.007.

59. C.-C. Chang, N. Scarr, and P. N. Kumta, "Synthesis and Electrochemical Characterization of $LiMO_2$ (M=Ni, $Ni_{0.75}Co_{0.25}$) for Rechargeable lithium-ion battEries," *Solid State Ionics* 112 (1998): 329–344, https://doi.org/10.1016/S0167-2738(98)00183-0.

60. D.-H. Cho, C.-H. Jo, W. Cho, et al., "Effect of Residual Lithium Compounds on Layer Ni-Rich $Li[Ni_{0.7}Mn_{0.3}]O_2$," *Journal of The Electrochemical Society* 161 (2014): A920, https://doi.org/10.1149/2.042406jes.

61. K. Shizuka, C. Kiyohara, K. Shima, and Y. Takeda, "Effect of CO_2 on Layered $Li_{1+z}Ni_{1-x-y}Co_xM_yO_2$ (M=Al, Mn) Cathode Materials for lithium-ion battEries," *Journal of Power Sources* 166 (2007): 233–238, https://doi.org/10.1016/j.jpowsour.2007.01.013.

62. K. Edström, T. Gustafsson, and J. O. Thomas, "The Cathode–electrolyte Interface in the Li-ion Battery," *Electrochimica Acta* 50 (2004): 397–403, https://doi.org/10.1016/j.electacta.2004.03.049.

63. Z. Wang, Y. Sun, L. Chen, and X. Huang, "Electrochemical Characterization of Positive Electrode Material $LiNi_{1/3}Co_{1/3}Mn_{1/3}O_2$ and Compatibility with Electrolyte for Lithium-Ion Batteries," *Journal of The Electrochemical Society* 151 (2004): A914, https://doi.org/10.1149/1.1740781.

64. N. Mahne, B. Schafzahl, C. Leypold, et al., "Singlet Oxygen Generation as a Major Cause for Parasitic Reactions during Cycling of Aprotic Lithium–oxygen Batteries," *Nature Energy* 2 (2017): 17036, https://doi.org/10.1038/nenergy.2017.36.

65. X. Q. Mu, S. L. Liu, M. Y. Zhang, et al., "Symmetry-Broken Ru Nanoparticles with Parasitic Ru-Co Dual-Single Atoms Overcome the Volmer Step of Alkaline Hydrogen Oxidation," *Angewandte Chemie International Edition* 63 (2024): 202319618, https://doi.org/10.1002/anie.202319618.

66. Z. Wang, C. Zhu, J. Liu, et al., "Catalytically Induced Robust Inorganic-Rich Cathode Electrolyte Interphase for 4.5 V Li||NCM622 Batteries," *Advanced Functional Materials* 33 (2023): 2212150, https://doi.org/10.1002/adfm.202212150.

67. Q. Li, Y. Wang, X. Wang, et al., "Investigations on the Fundamental Process of Cathode Electrolyte Interphase Formation and Evolution of High-Voltage Cathodes," *ACS Applied Materials & Interfaces* 12 (2020): 2319–2326, https://doi.org/10.1021/acsami.9b16727.

68. A. Ahuja, A. Kumar, K. Alam, et al., "Enhancing High-Voltage LNMO Cathode Performance in Li-Metal Batteries via Anionic Electrolyte Additive-Integrated CEI Engineering," *Advanced Functional Materials* 35 (2024): 2416634, https://doi.org/10.1002/adfm.202416634.

69. S. R. Li, C. H. Chen, X. Xia, and J. R. Dahn, "The Impact of Electrolyte Oxidation Products in $LiNi_{0.5}Mn_{1.5}O_4/Li_4Ti_5O_{12}$ Cells," *Journal of The Electrochemical Society* 160 (2013): A1524–A1528, https://doi.org/10.1149/2.051309jes.

70. A. J. Smith, J. C. Burns, X. Zhao, D. Xiong, and J. R. Dahn, "A High Precision Coulometry Study of the SEI Growth in Li/Graphite Cells," *Journal of The Electrochemical Society* 158 (2011): A447, https://doi.org/10.1149/1.3557892.

71. S. Jiao, X. Ren, R. Cao, et al., "Stable Cycling of High-voltage Lithium Metal Batteries in Ether Electrolytes," *Nature Energy* 3 (2018): 739–746, https://doi.org/10.1038/s41560-018-0199-8.

72. J. Chen, H. Zhang, M. Fang, C. Ke, S. Liu, and J. Wang, "Design of Localized High-Concentration Electrolytes via Donor Number," *ACS Energy Letters* 8 (2023): 1723–1734, https://doi.org/10.1021/acsenergylett.3c00004.

73. J. Zheng, G. Ji, X. Fan, et al., "High-Fluorinated Electrolytes for Li–S Batteries," *Advanced Energy Materials* 9 (2019): 1803774, https://doi.org/10.1002/aenm.201803774.

74. F. Pei, L. Wu, Y. Zhang, et al., "Interfacial Self-healing Polymer Electrolytes for Long-cycle Solid-state Lithium-sulfur Batteries," *Nature Communications* 15 (2024): 351, https://doi.org/10.1038/s41467-023-43467-w.

75. Z. Wang, J. Xia, X. Ji, et al., "Lithium Anode Interlayer Design for all-solid-state Lithium-metal Batteries," *Nature Energy* 9 (2024): 251–262, https://doi.org/10.1038/s41560-023-01426-1.

76. K. Liu, H. Cheng, Z. Wang, et al., "A 3 Mm-Ultrathin Hybrid Electrolyte Membrane with Integrative Architecture for all-Solid-State Lithium Metal Batteries," *Advanced Energy Materials* 14 (2024): 2303940, https://doi.org/10.1002/aenm.202303940.

77. X. Zhan, M. Li, X. Zhao, et al., "Self-assembled Hydrated Copper Coordination Compounds as Ionic Conductors for Room Temperature Solid-state Batteries," *Nature Communications* 15 (2024): 1056, https://doi.org/10.1038/s41467-024-45372-2.

16146840, 2026, 26, Downloaded from https://advanced.onlinelibrary.wiley.com/doi/10.1002/aenm.71073 by Jilin University, Wiley Online Library on [07/11/2026]. See the Terms and Conditions (https://onlinelibrary.wiley.com/terms-and-conditions) on Wiley Online Library for rules of use; OA articles are governed by the applicable Creative Commons License

78. L. Cui, S. Zhang, J. Ju, et al., "A Cathode Homogenization Strategy for Enabling Long-cycle-life All-solid-state Lithium Batteries," *Nature Energy* 9 (2024): 1084–1094, https://doi.org/10.1038/s41560-024-01596-6.

79. P. Lu, Z. Zhou, Z. Xiao, et al., "Materials and Chemistry Design for Low-temperature all-solid-state Batteries," *Joule* 8 (2024): 635–657, https://doi.org/10.1016/j.joule.2024.01.027.

80. X. Lu, Y. Wang, X. Xu, B. Yan, T. Wu, and L. Lu, "Polymer-Based Solid-State Electrolytes for High-Energy-Density Lithium-Ion Batteries – Review," *Advanced Energy Materials* 13 (2023): 2301746, https://doi.org/10.1002/aenm.202301746.

81. Y. Wang, Y. Lv, Y. Su, L. Chen, H. Li, and F. Wu, "5 V-class Sulfurized Spinel Cathode Stable in Sulfide all-solid-state Batteries," *Nano Energy* 90 (2021): 106589, https://doi.org/10.1016/j.nanoen.2021.106589.

82. L. Zhou, T.-T. Zuo, C. Y. Kwok, et al., "High Areal Capacity, Long Cycle Life 4 V Ceramic all-solid-state Li-ion Batteries Enabled by Chloride Solid Electrolytes," *Nature Energy* 7 (2022): 83–93, https://doi.org/10.1038/s41560-021-00952-0.

83. J. Janek and W. G. Zeier, "Challenges in Speeding up Solid-state Battery Development," *Nature Energy* 8 (2023): 230–240, https://doi.org/10.1038/s41560-023-01208-9.

84. Z. Song, T. Wang, H. Yang, et al., "Promoting High-voltage Stability through Local Lattice Distortion of Halide Solid Electrolytes," *Nature Communications* 15 (2024): 1481, https://doi.org/10.1038/s41467-024-45864-1.

85. Y. Ye, Z. Gu, J. Geng, et al., "Advanced High-Entropy Halide Solid Electrolytes Enabling High-Voltage, Long-Cycling all-Solid-State Batteries," *Nano Letters* 25 (2025): 3747–3755, https://doi.org/10.1021/acs.nanolett.4c05460.

86. G. Xiao, K. Yang, Y. Qiu, et al., "Dielectric-Tailored Space Charge Layer and Ion Coordination Structure for High-Voltage Polymer all-Solid-State Lithium Batteries," *Advanced Materials* 37 (2025): 2415411, https://doi.org/10.1002/adma.202415411.

87. B. Qiu, F. Xu, J. Qiu, et al., "Electrode-electrolyte Interface Mediation via Molecular Anchoring for 4.7 V iQuassolid-state Lithium Metal Batteries," *Energy Storage Materials* 60 (2023): 102832, https://doi.org/10.1016/j.ensm.2023.102832.

88. J. Zhu, R. Zhao, J. Zhang, et al., "Long-cycling and High-voltage Solid State Lithium Metal Batteries Enabled by Fluorinated and Crosslinked Polyether Electrolytes," *Angewandte Chemie International Edition* 63 (2024): 202400303, https://doi.org/10.1002/anie.202400303.

89. Y. Hou, Y. Q. Wang, Z. Q. Wei, et al., "A Solid Polymer Electrolyte with Inorganic-Enriched Cathode Electrolyte Interphases Enabling 5.1 V Solid-State Lithium-Ion Batteries," *Angew Chem Int Edit* 64 (2025): 202505147, https://doi.org/10.1002/anie.202505147.

90. L. Shen, J.-L. Li, W.-J. Kong, et al., "Anion-Engineering toward High-Voltage-Stable Halide Superionic Conductors for all-Solid-State Lithium Batteries," *Advanced Functional Materials* 34 (2024): 2408571, https://doi.org/10.1002/adfm.202408571.

91. Y. N. Yang, Z. Q. Hou, D. Z. Yang, et al., "Coordination-Induced Plastic Ceramic-Ether Coupling Electrolyte for High-Voltage Lithium Metal Batteries," *Advanced Functional Materials* 35 (2025): 2506241, https://doi.org/10.1002/adfm.202506241.

92. C. Li, Y. Zhong, R. Liao, et al., "Robust and Antioxidative Quasi-Solid-State Polymer Electrolytes for Long-Cycling 4.6 V Lithium Metal Batteries," *Advanced Materials* 37 (2025): 2500142, https://doi.org/10.1002/adma.202500142.

93. H. An, M. Li, Q. Liu, et al., "Strong Lewis-acid Coordinated PEO Electrolyte Achieves 4.8 V-class all-solid-state Batteries over 580 Wh Kg−1," *Nature Communications* 15 (2024): 9150, https://doi.org/10.1038/s41467-024-53094-8.

94. W. Zhang, V. Koverga, S. Liu, et al., "Single-phase Local-high-concentration Solid Polymer Electrolytes for Lithium-metal Batteries," *Nature Energy* 9 (2024): 386–400, https://doi.org/10.1038/s41560-023-01443-0.

95. W. D. Richards, L. J. Miara, Y. Wang, J. C. Kim, and G. Ceder, "Interface Stability in Solid-State Batteries," *Chemistry of Materials* 28 (2016): 266–273, https://doi.org/10.1021/acs.chemmater.5b04082.

96. A. A. Delluva, J. Kulberg-Savercool, and A. Holewinski, "Decomposition of Trace Li_2 CO_3 during Charging Leads to Cathode Interface Degradation with the Solid Electrolyte LLZO," *Advanced Functional Materials* 31 (2021): 2103716, https://doi.org/10.1002/adfm.202103716.

97. Q. Zhang, D. Cao, Y. Ma, A. Natan, P. Aurora, and H. Zhu, "Sulfide-Based Solid-State Electrolytes: Synthesis, Stability, and Potential for all-Solid-State Batteries," *Advanced Materials* 31 (2019): 1901131, https://doi.org/10.1002/adma.201901131.

98. S. Y. Kim, K. Kaup, K.-H. Park, et al., "Lithium Ytterbium-Based Halide Solid Electrolytes for High Voltage All-Solid-State Batteries," *ACS Materials Letters* 3 (2021): 930–938, https://doi.org/10.1021/acsmaterialslett.1c00142.

99. X. Zheng, E.-D. Fu, P. Chen, S. Liu, G.-R. Li, and X.-P. Gao, "Li3InCl6-coated LiCoO2 for High-performance all Solid-state Batteries," *Applied Physics Letters* 121 (2022): 033902, https://doi.org/10.1063/5.0097432.

100. I. Kochetkov, T.-T. Zuo, R. Ruess, et al., "Different Interfacial Reactivity of Lithium Metal Chloride Electrolytes with High Voltage Cathodes Determines Solid-state Battery Performance," *Energy & Environmental Science* 15 (2022): 3933–3944, https://doi.org/10.1039/D2EE00803C.

101. S. Wang, J. Liu, X. Song, et al., "Artificial Intelligence Empowers Solid-State Batteries for Material Screening and Performance Evaluation," *Nano-Micro Letters* 17 (2025): 287, https://doi.org/10.1007/s40820-025-01797-y.

102. X. J. Tang, M. Q. Feng, W. H. Lv, and S. Lv, "Applications of all-Solid-State Lithium-Ion Batteries across Wide Temperature Ranges: Challenges, Progress, and Perspectives," *Advanced Energy Materials* 15 (2025): 2500479, https://doi.org/10.1002/aenm.202500479.

103. R. Xiao, Z. Y. Qu, J. X. Ren, G. X. Wang, Z. H. Sun, and F. Li, "Current Status and Future Prospects of Solid-State Lithium–Sulfur Batteries: a Focus on Reaction and Interface Engineering," *Advanced Energy Materials* 16 (2026): 2501926, https://doi.org/10.1002/aenm.202501926.

104. H. Wang, N. Deng, Y. Wang, et al., "Research Progress and Challenges of High-Performance Solid-State Lithium Sulfur Batteries: Cathodes, Electrolytes, and Anodes," *Small* 21 (2025): 2411452, https://doi.org/10.1002/smll.202411452.

105. C. Li and Y. Du, "Building a Better All-Solid-State Lithium-Ion Battery with Halide Solid-State Electrolyte," *ACS Nano* 19 (2025): 4121–4155, https://doi.org/10.1021/acsnano.4c15005.

106. W. Li, Z. He, Y. Jie, et al., "Understanding and Design of Cathode–Electrolyte Interphase in High-Voltage Lithium–Metal Batteries," *Advanced Functional Materials* 34 (2024): 2406770, https://doi.org/10.1002/adfm.202406770.

107. J. W. Wang, K. He, S. J. Li, et al., "Charge Delocalization Electrolyte Design to Construct Fast Dynamic Interface for High-Voltage Lithium Metal Batteries," *Advanced Functional Materials* 36 (2026): 31823, https://doi.org/10.1002/adfm.202531823.

108. X. Luo, Z. Chen, X. Qiu, and Y. Qian, "Structure and Interfacial-Stable Binder Engineering Enables High-Rate Capability of NCM811 Cathodes at 4.6 V," *Advanced Energy Materials* (2026): 70842, https://doi.org/10.1002/aenm.70842.

109. Y. Bi, J. Tao, Y. Wu, et al., "Reversible Planar Gliding and Microcracking in a Single-crystalline Ni-rich Cathode," *Science* 370 (2020): 1313–1317, https://doi.org/10.1126/science.abc3167.

110. Z. Zhang, J. Yang, W. Huang, et al., *Matter* 4 (2021): 302–312, https://doi.org/10.1016/j.matt.2020.10.021.

16146840, 2026, 26, Downloaded from https://advanced.onlinelibrary.wiley.com/doi/10.1002/aenm.71073 by Jilin University, Wiley Online Library on [07/11/2026]. See the Terms and Conditions (https://onlinelibrary.wiley.com/terms-and-conditions) on Wiley Online Library for rules of use; OA articles are governed by the applicable Creative Commons License

111. Q. Wang, C. Zhao, J. Wang, et al., "High Entropy Liquid Electrolytes for Lithium Batteries," *Nature Communications* 14 (2023): 440, https://doi.org/10.1038/s41467-023-36075-1.

112. Q. Wang, C. Zhao, Z. Yao, et al., "Entropy-Driven Liquid Electrolytes for Lithium Batteries," *Advanced Materials* 35 (2023): 2210677, https://doi.org/10.1002/adma.202210677.

113. J. Alvarado, M. A. Schroeder, M. Zhang, et al., "A Carbonate-free, Sulfone-based Electrolyte for High-voltage Li-ion Batteries," *Materials Today* 21 (2018): 341–353, https://doi.org/10.1016/j.mattod.2018.02.005.

114. J. Liu, J. Wang, Y. Ni, et al., "Tuning Interphase Chemistry to Stabilize High-Voltage LiCoO2 Cathode Material via Spinel Coating," *Angewandte Chemie International Edition* 61 (2022): 202207000, https://doi.org/10.1002/anie.202207000.

115. Y. Yang, H. Wang, C. Zhu, and J. Ma, "Armor-like Inorganic-rich Cathode Electrolyte Interphase Enabled by the Pentafluorophenylboronic Acid Additive for High-voltage Li||NCM622 Batteries," *Angewandte Chemie International Edition* 62 (2023): 202300057, https://doi.org/10.1002/anie.202300057.

116. D. Wu, C. Zhu, H. Wang, et al., "Mechanically and Thermally Stable Cathode Electrolyte Interphase Enables High-temperature, High-voltage Li||$LiCoO_2$ Batteries," *Angewandte Chemie International Edition* 63 (2024): 202315608, https://doi.org/10.1002/anie.202315608.

117. W. Lu, J. Zhang, J. Xu, X. Wu, and L. Chen, "In Situ Visualized Cathode Electrolyte Interphase on $LiCoO_2$ in High Voltage Cycling," *ACS Applied Materials & Interfaces* 9 (2017): 19313–19318, https://doi.org/10.1021/acsami.7b03024.

118. J. Yang, X. Li, K. Qu, et al., "Concentrated Ternary Ether Electrolyte Allows for Stable Cycling of a Lithium Metal Battery with Commercial Mass Loading High-nickel NMC and Thin Anodes," *Carbon Energy* 5 (2023): 275, https://doi.org/10.1002/cey2.275.

119. X. Deng, J. Li, P. Lai, et al., "Tailored Interface Composition Improves the Integrity of Electrode/Electrolyte Interphases for High-voltage Ni-rich Lithium Metal Batteries in a Sulfolane-based Electrolyte," *Chemical Engineering Journal* 465 (2023): 142907, https://doi.org/10.1016/j.cej.2023.142907.

120. H. A. Ishfaq, C. C. Cardona, E. Tchernychova, P. Johansson, R. Dominko, and S. Drvarič Talian, "Enhanced Performance of Lithium Metal Batteries via Cyclic Fluorinated Ether Based Electrolytes," *Energy Storage Materials* 69 (2024): 103375, https://doi.org/10.1016/j.ensm.2024.103375.

121. W. Li, A. Dolocan, P. Oh, et al., "Dynamic oBehavir of Interphases and Its Implication on High-energy-density Cathode Materials in Lithium-ion Batteries," *Nature Communications* 8 (2017): 14589, https://doi.org/10.1038/ncomms14589.

122. S. Wen, Y. Han, P. Wang, et al., "An Interfacial Mechanism of Chelate-Borate Electrolyte Additives in Ni-Rich $LiNi_{0.8}$ $Mn_{0.1}$ $Co_{0.1}$ O_2 Cathodes," *ACS Applied Energy Materials* 4 (2021): 12525–12534, https://doi.org/10.1021/acsaem.1c02331.

123. J. Liu, X. Li, J. Huang, G. Yang, and J. Ma, "Additive-Guided Solvation-Regulated Flame-Retardant Electrolyte Enables High-Voltage Lithium Metal Batteries with Robust Electrode Electrolyte Interphases," *Advanced Functional Materials* 34 (2024): 2312762, https://doi.org/10.1002/adfm.202312762.

124. B. Zhang, H. Zhang, H. Luo, et al., "Manipulated Fluoro-Ether Derived Nucleophilic Decomposition Products for Mitigating Polarization-Induced Capacity Loss in Li-Rich Layered Cathode," *Angewandte Chemie International Edition* 63 (2024): 202316790, https://doi.org/10.1002/anie.202316790.

125. S. Wang, K. Liang, H. Zhao, et al., "Multipoint Adsorption Constructs Stable Interface Chemistry for High-nickel Cathode Material," *Energy Storage Materials* 63 (2023): 103027, https://doi.org/10.1016/j.ensm.2023.103027.

126. M. J. Zuba, A. Grenier, Z. Lebens-Higgins, et al., "Whither Mn Oxidation in Mn-Rich Alkali-Excess Cathodes?," *ACS Energy Letters* 6 (2021): 1055–1064, https://doi.org/10.1021/acsenergylett.0c02418.

127. L. An, J. E. N. Swallow, P. Cong, et al., "Distinguishing Bulk Redox from near-surface Degradation in Lithium Nickel Oxide Cathodes," *Energy & Environmental Science* 17 (2024): 8379–8391, https://doi.org/10.1039/D4EE02398F.

128. Y. Wang, Y. Li, Z. Li, et al., "Monitoring the Local Coordination Evolutions in Li-Rich Cathode Materials via in Situ Raman Spectroscopy," *ACS Energy Letters* 8 (2023): 4888–4894, https://doi.org/10.1021/acsenergylett.3c02109.

129. R. Baddour-Hadjean and J.-P. Pereira-Ramos, "Raman Microspectrometry Applied to the Study of Electrode Materials for Lithium Batteries," *Chemical Reviews* 110 (2010): 1278–1319, https://doi.org/10.1021/cr800344k.

130. D. Liu, Z. Shadike, R. Lin, et al., "Review of Recent Development of in Situ/Operando Characterization Techniques for Lithium Battery Research," *Advanced Materials* 31 (2019): 1806620, https://doi.org/10.1002/adma.201806620.

131. B. Zhang, L. Wang, X. Wang, et al., "Sustained Releasing Superoxo Scavenger for Tailoring the Electrode-electrolyte Interface on Li-rich Cathode," *Energy Storage Materials* 53 (2022): 492–504, https://doi.org/10.1016/j.ensm.2022.09.032.

132. Y. Chen, Q. He, Y. Mo, et al., "Engineering an Insoluble Cathode Electrolyte Interphase Enabling High Performance NCM811//Graphite Pouch Cell at 60°C," *Advanced Energy Materials* 12 (2022): 2201631, https://doi.org/10.1002/aenm.202201631.

133. S. Kim, H.-S. Kim, B. Kim, Y.-J. Kim, J.-W. Jung, and W.-H. Ryu, "In Situ Gas Analysis by Differential Electrochemical Mass Spectrometry for Advanced Rechargeable Batteries: a Review," *Advanced Energy Materials* 13 (2023): 2301983, https://doi.org/10.1002/aenm.202301983.

134. K. Zhao, X. Jiang, X. Wu, et al., "Recent Development and Applications of Differential Electrochemical Mass Spectrometry in Emerging Energy Conversion and Storage Solutions," *Chemical Society Reviews* 53 (2024): 6917–6959, https://doi.org/10.1039/D3CS00840A.

135. G. Tang, J. Zhang, S. Ma, J. Li, Z. Peng, and W. Chen, "Unveiling Gas Production in Rechargeable Batteries via in Situ Differential Electrochemical Mass Spectrometry," *Chemical Society Reviews* 54 (2025): 7216–7251, https://doi.org/10.1039/D5CS00276A.

136. T. Liu, J. Liu, L. Li, et al., "Origin of Structural Degradation in Li-rich Layered Oxide Cathode," *Nature* 606 (2022): 305–312, https://doi.org/10.1038/s41586-022-04689-y.

137. M. H. Han, E. Gonzalo, G. Singh, and T. Rojo, "A Comprehensive Review of Sodium Layered Oxides: Powerful Cathodes for Na-ion Batteries," *Energy & Environmental Science* 8 (2015): 81–102, https://doi.org/10.1039/C4EE03192J.

138. Y. Kato, S. Hori, T. Saito, et al., "High-power all-solid-state Batteries Using Sulfide Superionic Conductors," *Nature Energy* 1 (2016): 16030, https://doi.org/10.1038/nenergy.2016.30.

139. M. L. Holekevi Chandrappa, J. Qi, C. Chen, S. Banerjee, and S. P. Ong, "Thermodynamics and Kinetics of the Cathode–Electrolyte Interface in all-Solid-State Li–S Batteries," *Journal of the American Chemical Society* 144 (2022): 18009–18022, https://doi.org/10.1021/jacs.2c07482.

140. A. Banerjee, X. Wang, C. Fang, E. A. Wu, and Y. S. Meng, "Interfaces and Interphases in all-Solid-State Batteries with Inorganic Solid Electrolytes," *Chemical Reviews* 120 (2020): 6878–6933, https://doi.org/10.1021/acs.chemrev.0c00101.

141. Y. Xiao, Y. Wang, S.-H. Bo, J. C. Kim, L. J. Miara, and G. Ceder, "Understanding Interface Stability in Solid-state Batteries," *Nature Reviews Materials* 5 (2020): 105–126, https://doi.org/10.1038/s41578-019-0157-5.

16146840, 2026, 26, Downloaded from https://advanced.onlinelibrary.wiley.com/doi/10.1002/aenm.71073 by Jilin University, Wiley Online Library on [07/11/2026]. See the Terms and Conditions (https://onlinelibrary.wiley.com/terms-and-conditions) on Wiley Online Library for rules of use; OA articles are governed by the applicable Creative Commons License

142. K. Leung, "DFT modelIng of Explicit Solid–solid Interfaces in Batteries: Methods and Challenges," *Physical Chemistry Chemical Physics* 22 (2020): 10412–10425, https://doi.org/10.1039/C9CP06485K.

143. C. Wang, M. Aykol, and T. Mueller, "Nature of the Amorphous–Amorphous Interfaces in Solid-State Batteries Revealed Using Machine-Learned Interatomic Potentials," *Chemistry of Materials* 35 (2023): 6346–6356, https://doi.org/10.1021/acs.chemmater.3c00993.

144. Z. Wu, X. Li, C. Zheng, et al., "Interfaces in Sulfide Solid Electrolyte-Based all-Solid-State Lithium Batteries: Characterization, Mechanism and Strategy," *Electrochemical Energy Reviews* 6 (2023): 10, https://doi.org/10.1007/s41918-022-00176-0.

145. L.-Q. Chen, "Phase-Field Models for Microstructure Evolution," *Annual Review of Materials Research* 32 (2002): 113–140, https://doi.org/10.1146/annurev.matsci.32.112001.132041.

146. J. Xu, C. Li, S. Yang, L. Xin, and Z. Wang, "Pulsed Charging Strategies for Lithium Dendrite Suppression:Phase-Field Insights into Duty Cycle and Stack Pressure Effects," *Journal of The Electrochemical Society* 172 (2025): 050533, https://doi.org/10.1149/1945-7111/add8c2.

147. S. Dargaville and T. W. Farrell, "A Comparison of Mathematical Models for Phase-change in High-rate $LiFePO_4$ Cathodes," *Electrochimica Acta* 111 (2013): 474–490, https://doi.org/10.1016/j.electacta.2013.08.014.

148. A. Azizpour, D. Duranti, M. Giuliano, L. Belforte, E. Rossi, and G. Gramse, "Understanding Fracture Mechanisms in NMC811 Particles via Stochastic Anisotropic Phase-field modelIng," *Journal of Power Sources* 666 (2026): 239125, https://doi.org/10.1016/j.jpowsour.2025.239125.

149. K. T. Butler, D. W. Davies, H. Cartwright, O. Isayev, and A. Walsh, "Machine Learning for Molecular and Materials Science," *Nature* 559 (2018): 547–555, https://doi.org/10.1038/s41586-018-0337-2.

150. F. Wang, Y.-H. Tang, Z.-B. Ma, Y.-C. Jin, and J. Cheng, "Domain Oriented Universal Machine Learning Potential Enables Fast Exploration of Chemical Space of Battery Electrolytes," *Nature Communications* 17 (2025): 1226, https://doi.org/10.1038/s41467-025-67982-0.

151. Z. Yi, Y. Zhou, H. Liu, et al., "Predicting Practical Reduction Potential of Electrolyte Solvents via Computational Hydrogen Electrode and Interpretable Machine-learning Models," *npj Computational Materials* 11 (2025): 135, https://doi.org/10.1038/s41524-025-01582-w.

152. Z. Qiu, Y. Zhang, P. Dong, D. Wang, and S. Xia, "A Ternary Oxide Precursor with Trigonal Structure for Synthesis of $LiNi_{0.80}Co_{0.15}Al_{0.05}O_2$ Cathode Material," *Journal of Solid State Electrochemistry* 21 (2017): 3037–3046, https://doi.org/10.1007/s10008-017-3643-y.

153. S. Xia, F. Li, F. Cheng, et al., "Synthesis of Spherical Fluorine Modified Gradient Li-Ion Battery Cathode Material $LiNi_{0.80}Co_{0.15}Al_{0.05}O_2$ by Simple Solid Phase Method," *Journal of The Electrochemical Society* 165 (2018): A1019, https://doi.org/10.1149/2.1021805jes.

154. H. Zhang, X. Zhang, T. Zeng, et al., "Conversion of Residual Lithium into Fast Ionic Conductor Coating to Achieve One-step Double Modification Strategy in $LiNi_{0.8}Co_{0.15}Al_{0.05}O_2$," *Journal of Alloys and Compounds* 931 (2023): 167638, https://doi.org/10.1016/j.jallcom.2022.167638.

155. X. Wu, J. Lu, Y. Han, et al., "Template-assisted Synthesis of $LiNi_{0.8}Co_{0.15}Al_{0.05}O_2$ Hollow Nanospheres as Cathode Material for lithium-ion battEries," *Journal of Materials Science* 55 (2020): 9493–9503, https://doi.org/10.1007/s10853-020-04627-1.

156. M. Zhang, J. Shen, J. Li, et al., "Effect of Micron Sized Particle on the Electrochemical Properties of Nickel-rich $LiNi_{0.8}Co_{0.1}Mn_{0.1}O_2$ Cathode Materials," *Ceramics International* 46 (2020): 4643–4651, https://doi.org/10.1016/j.ceramint.2019.10.195.

157. J. Zheng, Y. Ye, T. Liu, et al., "Ni/Li Disordering in Layered Transition Metal Oxide: Electrochemical Impact, Origin, and Control," *Accounts of Chemical Research* 52 (2019): 2201–2209, https://doi.org/10.1021/acs.accounts.9b00033.

158. D. Wang, R. Kou, Y. Ren, et al., "Synthetic Control of Kinetic Reaction Pathway and Cationic Ordering in High-Ni Layered Oxide Cathodes," *Advanced Materials* 29 (2017): 1606715, https://doi.org/10.1002/adma.201606715.

159. J. Cao, S. Guo, R. Yan, C. Zhang, J. Guo, and P. Zheng, "Carbon-coated Single-crystalline $LiMn_2O_4$ Nanowires Synthesized by High-temperature Solid-state Reaction with High Capacity for Li-ion Battery," *Journal of Alloys and Compounds* 741 (2018): 1–6, https://doi.org/10.1016/j.jallcom.2018.01.107.

160. A. Stein, S. W. Keller, and T. E. Mallouk, "Turning down the Heat: Design and Mechanism in Solid-State Synthesis," *Science* 259 (1993): 1558–1564, https://doi.org/10.1126/science.259.5101.1558.

161. Y. Xuanye, Y. Hongge, C. Jihua, et al., "Solid-state synthesis of Ultrafine-$LiCoO_2$ by Enhanced Thermal Decomposition of Carbonate Precursors Followed by Double-calcining," *Solid State Ionics* 289 (2016): 159–167, https://doi.org/10.1016/j.ssi.2016.03.005.

162. H. Qiu, D. Jin, C. Wang, et al., "Design of Li_2FeSiO_4 Cathode Material for Enhanced Lithium-ion Storage Performance," *Chemical Engineering Journal* 379 (2020): 122329, https://doi.org/10.1016/j.cej.2019.122329.

163. D. Wang, I. Belharouak, L. H. Ortega, et al., "Synthesis of High Capacity Cathodes for Lithium-ion Batteries by Morphology-tailored Hydroxide coPrecipitation," *Journal of Power Sources* 274 (2015): 451–457, https://doi.org/10.1016/j.jpowsour.2014.10.016.

164. S. Zhang, C. Deng, S. Y. Yang, and H. Niu, "An Improved Carbonate coPrecipitation Method for the Preparation of Spherical $Li[Ni_{1/3}Co_{1/3}Mn_{1/3}]O_2$ Cathode Material," *Journal of Alloys and Compounds* 484 (2009): 519–523, https://doi.org/10.1016/j.jallcom.2009.04.149.

165. K. Heo, J.-S. Lee, H.-S. Kim, et al., "Ionic Conductor-$LiNi_{0.8}Co_{0.1}Mn_{0.1}O_2$ Composite Synthesized by Simultaneous Co-Precipitation for Use in Lithium Ion Batteries," *Journal of The Electrochemical Society* 165 (2018): A2955, https://doi.org/10.1149/2.0201813jes.

166. B. Huang, L. Cheng, X. Li, et al., "Layered Cathode Materials: Precursors, Synthesis, Microstructure, Electrochemical Properties, and Battery Performance," *Small* 18 (2022): 2107697, https://doi.org/10.1002/smll.202107697.

167. C.-K. Yang, L.-Y. Qi, Z. Zuo, et al., "Insights into the Inner Structure of High-nickel Agglomerate as High-performance Lithium-ion Cathodes," *Journal of Power Sources* 331 (2016): 487–494, https://doi.org/10.1016/j.jpowsour.2016.09.068.

168. Q. Zhu, H. Xiao, R. Zhang, S. Geng, and Q. Huang, "Effect of Impeller Type on Preparing Spherical and Dense $Ni_{1-x-y}Co_x$ Mn_y $(OH)_2$ Precursor via Continuous coPrecipitation in Pilot Scale: a Case of $Ni_{0.6}Co_{0.2}Mn_{0.2}(OH)_2$," *Electrochimica Acta* 318 (2019): 1–13, https://doi.org/10.1016/j.electacta.2019.06.008.

169. M. Noh and J. Cho, "Optimized Synthetic Conditions of $LiNi_{0.5}Co_{0.2}Mn_{0.3}O_2$ Cathode Materials for High Rate Lithium Batteries via Co-Precipitation Method," *Journal of The Electrochemical Society* 160 (2013): A105, https://doi.org/10.1149/2.004302jes.

170. B. Wang, C. Zhu, H. Lei, et al., "Regeneration of Spent NCM622: Reconstructing the Rich Lattice Oxygen Surface for Enhanced Stability," *Journal of Materials Chemistry A* 13 (2025): 12998–13009, https://doi.org/10.1039/D5TA00776C.

171. F. Guo, Y. Xie, and Y. Zhang, "Tuning Li-excess to Optimize Ni/Li Exchange and Improve Stability of Structure in $LiNi_{0.8}Co_{0.1}Mn_{0.1}O_2$ Cathode Material for Lithium-ion Batteries," *Nano Research* 15 (2022): 8962–8971, https://doi.org/10.1007/s12274-022-4532-y.

172. B. Wang, C. Zhu, H. Lei, et al., "Regeneration of spent NCM622: reconstructing the rich lattice oxygen surface for enhanced stability," *Journal of Materials Chemistry A*, 13 (18) (2025) 12998, https://doi.org/10.1039/d5ta00776c.

173. Z. Ahsan, Z. Cai, S. Wang, et al., "Structural and Electrochemical Characterization of Vanadium-excess $Li_3V_2(PO_4)_3$-$LiVOPO_4$/C Composite Cathode Material Synthesized by Sol–gel Method," *Journal of Solid State Electrochemistry* 25 (2021): 2127–2137, https://doi.org/10.1007/s10008-021-04986-y.

16146840, 2026, 26, Downloaded from https://advanced.onlinelibrary.wiley.com/doi/10.1002/aenm.71073 by Jilin University, Wiley Online Library on [07/11/2026]. See the Terms and Conditions (https://onlinelibrary.wiley.com/terms-and-conditions) on Wiley Online Library for rules of use; OA articles are governed by the applicable Creative Commons License

174. N. Kızıltaş-Yavuz, M. Herklotz, A. M. Hashem, et al., "Synthesis, Structural, Magnetic and Electrochemical Properties of $LiNi_{1/3}Mn_{1/3}Co_{1/3}O_2$ Prepared by a Sol–gel Method Using Table Sugar as Chelating Agent," *Electrochimica Acta* 113 (2013): 313–321, https://doi.org/10.1016/j.electacta.2013.09.065.

175. Q. Liu, L. Yang, Z. Mei, et al., "Constructing Host–guest Recognition Electrolytes Promotes the Li^+ Kinetics in Solid-state Batteries," *Energy & Environmental Science* 17 (2024): 780–790, https://doi.org/10.1039/D3EE03283C.

176. J. Zhang, X. Xiao, J. Chen, et al., "All Wet-coating Process for Chemical Stable Antimony and Selenium Dual-doped Argyrodite Electrolyte Based all-solid-state Lithium Batteries," *Materials Science and Engineering: R: Reports* 164 (2025): 100972, https://doi.org/10.1016/j.mser.2025.100972.

177. W. Cao, "Research Progress on Electrode Coating Technology for Lithium-ion Batteries," *Energy Storage Science and Technology* 14 (2025): 90–103, https://doi.org/10.19799/j.cnki.2095-4239.2024.0574.

178. J. Choi, S. Moon, D. Lee, et al., "Dry Electrode Technology: a New Processing Paradigm for Enhancing Performance and Sustainability in Lithium-based Batteries," *Chemical Engineering Journal* 519 (2025): 165044, https://doi.org/10.1016/j.cej.2025.165044.

179. M. Al-Shroofy, Q. Zhang, J. Xu, T. Chen, A. P. Kaur, and Y.-T. Cheng, "Solvent-free Dry Powder Coating Process for Low-cost Manufacturing of LiNi1/3Mn1/3Co1/3O2 Cathodes in Lithium-ion Batteries," *Journal of Power Sources* 352 (2017): 187–193, https://doi.org/10.1016/j.jpowsour.2017.03.131.

180. Y. Zhang, S. Lu, F. Lou, and Z. Yu, "Leveraging Synergies by Combining Polytetrafluorethylene with Polyvinylidene Fluoride for Solvent-Free Graphite Anode Fabrication," *Energy Technology* 10 (2022): 2200732, https://doi.org/10.1002/ente.202200732.

181. M. Ryu, Y.-K. Hong, S.-Y. Lee, and J. H. Park, "Ultrahigh Loading Dry-process for Solvent-free Lithium-ion Battery Electrode Fabrication," *Nature Communications* 14 (2023): 1316, https://doi.org/10.1038/s41467-023-37009-7.

182. A. Ponrouch, A. R. Goñi, M. T. Sougrati, et al., "A New Room Temperature and Solvent Free Carbon Coating Procedure for Battery Electrode Materials," *Energy & Environmental Science* 6 (2013): 3363–3371, https://doi.org/10.1039/C3EE41243A.

183. M. Wang, K. Uzun, B. R. Frieberg, et al., "Influence of Mixing Process on the Performance of Electrodes Made by a Dry Coating Method," *Journal of The Electrochemical Society* 170 (2023): 010541, https://doi.org/10.1149/1945-7111/acb389.

184. M. Horst, F. Beverborg, L. Bahlmann, et al., "Effect of Active Material Morphology on PTFE-fibrillation, Powder Characteristics and Electrode Properties in Dry Electrode Coating Processes," *Powder Technology* 451 (2025): 120451, https://doi.org/10.1016/j.powtec.2024.120451.

185. L. Froboese, J. F. V. D. Sichel, T. Loellhoeffel, L. Helmers, and A. Kwade, "Effect of Microstructure on the Ionic Conductivity of an all Solid-State Battery Electrode," *Journal of The Electrochemical Society* 166 (2019): A318, https://doi.org/10.1149/2.0601902jes.

186. M. Stein, A. Mistry, and P. P. Mukherjee, "Mechanistic Understanding of the Role of Evaporation in Electrode Processing," *Journal of The Electrochemical Society* 164 (2017): A1616, https://doi.org/10.1149/2.1271707jes.

187. K. Rollag, D. Juarez-Robles, Z. Du, D. L. Wood, and P. P. Mukherjee, "Drying Temperature and Capillarity-Driven Crack Formation in Aqueous Processing of Li-Ion Battery Electrodes," *ACS Applied Energy Materials* 2 (2019): 4464–4476, https://doi.org/10.1021/acsaem.9b00704.

188. F. Hippauf, B. Schumm, S. Doerfler, et al., "Overcoming Binder Limitations of Sheet-type Solid-state Cathodes Using a Solvent-free Dry-film Approach," *Energy Storage Materials* 21 (2019): 390–398, https://doi.org/10.1016/j.ensm.2019.05.033.

189. C. de la Torre-Gamarra, M. E. Sotomayor, J.-Y. Sanchez, et al., "High Mass Loading Additive-free LiFePO4 Cathodes with 500 Mm Thickness for High Areal Capacity Li-ion Batteries," *Journal of Power Sources* 458 (2020): 228033, https://doi.org/10.1016/j.jpowsour.2020.228033.

190. B. Ludwig, Z. Zheng, W. Shou, Y. Wang, and H. Pan, "Solvent-Free Manufacturing of Electrodes for Lithium-ion Batteries," *Scientific Reports* 6 (2016): 23150, https://doi.org/10.1038/srep23150.

191. Y. Li, Y. Wu, T. Ma, et al., "Long-Life Sulfide all-Solid-State Battery Enabled by Substrate-Modulated Dry-Process Binder," *Advanced Energy Materials* 12 (2022): 2201732, https://doi.org/10.1002/aenm.202201732.

192. Z. Chen, J. Hou, M. Yang, J. Zhu, and X. Zhuang, "Sulfide-based Solid Electrolyte and Electrode Membranes for all-solid-state Lithium Batteries," *Chemical Engineering Journal* 502 (2024): 158136, https://doi.org/10.1016/j.cej.2024.158136.

193. D. Lee and A. Manthiram, "Boosting the Electrochemical Performance with Functionalized Dry Electrodes for Practical all-solid-state Batteries," *Journal of Materials Chemistry A* 12 (2024): 3323–3330, https://doi.org/10.1039/D3TA05631G.

194. W. Yao, M. Chouchane, W. Li, et al., "A 5 V-class Cobalt-free Battery Cathode with High Loading Enabled by Dry Coating," *Energy & Environmental Science* 16 (2023): 1620–1630, https://doi.org/10.1039/D2EE03840D.

195. H. Oh, G.-S. Kim, J. Bang, S. Kim, and K.-M. Jeong, "Dry-processed Thick Electrode Design with a Porous Conductive Agent Enabling 20 mA h cm −2 for High-energy-density Lithium-ion Batteries," *Energy & Environmental Science* 18 (2025): 645–658, https://doi.org/10.1039/D4EE04106B.

196. W. M. Seong, Y. Kim, and A. Manthiram, "Impact of Residual Lithium on the Adoption of High-Nickel Layered Oxide Cathodes for Lithium-Ion Batteries," *Chemistry of Materials* 32 (2020): 9479–9489, https://doi.org/10.1021/acs.chemmater.0c02808.

197. S. Zhao, W. Jiang, X. Zhu, M. Ling, and C. Liang, "Understanding the Synthesis of Inorganic Solid-state Electrolytes for Li Ion Batteries: Features and Progress," *Sustainable Materials and Technologies* 33 (2022): e00491, https://doi.org/10.1016/j.susmat.2022.e00491.

198. Z. Wang, Y. Jiang, J. Wu, et al., "Reaction Mechanism of Li2S-P2S5 System in Acetonitrile Based on Wet Chemical Synthesis of Li7P3S11 Solid Electrolyte," *Chemical Engineering Journal* 393 (2020): 124706, https://doi.org/10.1016/j.cej.2020.124706.

199. Y. Liang, C. Peng, Y. Kamiike, K. Kuroda, and M. Okido, "Gallium Doped NASICON Type $LiTi_2(PO_4)_3$ Thin-film Grown on Graphite Anode as Solid Electrolyte for all solid-state Lithium Batteries," *Journal of Alloys and Compounds* 775 (2019): 1147–1155, https://doi.org/10.1016/j.jallcom.2018.10.226.

200. H. Jin, X. Wang, S. Zhang, et al., "Boosting Ionic Conductivity of Fluoride Electrolytes by Polyanion Coordination Chemistry Enabling 5 V-Class all-solid-state Batteries," *Joule* 10 (2026): 102233, https://doi.org/10.1016/j.joule.2025.102233.

201. N. Hamao and J. Akimoto, "Synthesis of Garnet-type $Li_7La_3Zr_2O_{12}$ by Coprecipitation Method," *Chemistry Letters* 44 (2015): 970–972, https://doi.org/10.1246/cl.150295.

202. F. Ji, S. Xiao, J. Cheng, et al., "Low-cost and Facile Synthesis of LAGP solid-state Electrolyte via a coPrecipitation Method," *Applied Physics Letters* 121 (2022): 023904, https://doi.org/10.1063/5.0098362.

203. I. Stenina, A. Pyrkova, and A. Yaroslavtsev, "NASICON-Type $Li_{1+x}Al_xZr_yTi_{2-x-y}(PO_4)_3$ Solid Electrolytes: Effect of Al, Zr Co-Doping and Synthesis Method," *Batteries* 9 (2023): 59, https://doi.org/10.3390/batteries9010059.

204. M. Kim, G. Kim, and H. Lee, "Tri-Doping of Sol–Gel Synthesized Garnet-Type Oxide Solid-State Electrolyte," *Micromachines* 12 (2021): 134, https://doi.org/10.3390/mi12020134.

205. D. S. Aleksandrov, A. A. Popovich, W. Qingsheng, and P. A. Novikov, "Synthesis of Tetragonal Solid-state Electrolyte $Li_7La_3Zr_2O_{12}$," *Materials Today: Proceedings* 30 (2020): 587–591, https://doi.org/10.1016/j.matpr.2020.01.142.

16146840, 2026, 26, Downloaded from https://advanced.onlinelibrary.wiley.com/doi/10.1002/aenm.71073 by Jilin University, Wiley Online Library on [07/11/2026]. See the Terms and Conditions (https://onlinelibrary.wiley.com/terms-and-conditions) on Wiley Online Library for rules of use; OA articles are governed by the applicable Creative Commons License

206. C. Shen, W. Feng, Y. Yu, et al., "In Situ Polymerization Inhibiting Electron Localization in Hybrid Electrolyte for Room-Temperature Solid-State Lithium Metal Batteries," *Advanced Energy Materials* 14 (2024): 2304511, https://doi.org/10.1002/aenm.202304511.

207. B. Shen, L. Li, X. Yao, and B. Huang, "Interfacial Engineering of $LiCoO_2/Li_{10}GeP_2S_{12}$ with Electron-ion Mixed Conductor $Li_{7.5}La_3Zr_{1.5}Co_{0.5}O_{12}$ for High Stable all-solid-state Batteries," *Ceramics International* 50 (2024): 7150–7155, https://doi.org/10.1016/j.ceramint.2023.12.082.

208. J. B. Bates, N. J. Dudney, G. R. Gruzalski, et al., "Electrical Properties of Amorphous Lithium Electrolyte Thin Films," *Solid State Ionics* 53-56, no. 53-56 (1992): 647–654, https://doi.org/10.1016/0167-2738(92)90442-R.

209. Y. Wu, K. Wang, K. Liu, et al., "Rapid Processing of Uniform, Thin, Robust, and Large-Area Garnet Solid Electrolyte by Atmospheric Plasma Spraying," *Advanced Energy Materials* 13 (2023): 2300809, https://doi.org/10.1002/aenm.202300809.

210. L. Luo, Z. Sun, H. Gao, et al., "Insights into the Enhanced Interfacial Stability Enabled by Electronic Conductor Layers in Solid-State Li Batteries," *Advanced Energy Materials* 13 (2023): 2203517, https://doi.org/10.1002/aenm.202203517.

211. A. C. Kozen, A. J. Pearse, C.-F. Lin, M. Noked, and G. W. Rubloff, "Atomic Layer Deposition of the Solid Electrolyte LiPON," *Chemistry of Materials* 27 (2015): 5324–5331, https://doi.org/10.1021/acs.chemmater.5b01654.

212. K. Ahuja, V. Sallaz, R. B. Nuwayhid, et al., "Ultrathin on-chip ALD LiPON Capacitors for High Frequency Application," *Journal of Power Sources* 575 (2023): 233056, https://doi.org/10.1016/j.jpowsour.2023.233056.

213. L. Zhao, G. Chen, Y. Weng, et al., "Precise Al_2O_3 Coating on $LiNi_{0.5}Co_{0.2}Mn_{0.3}O_2$ by Atomic Layer Deposition Restrains the Shuttle Effect of Transition Metals in Li-Ion Capacitors," *Chemical Engineering Journal* 401 (2020): 126138, https://doi.org/10.1016/j.cej.2020.126138.

214. S. Xu, R. M. Jacobs, H. M. Nguyen, et al., "Lithium Transport through Lithium-ion Battery Cathode Coatings," *Journal of Materials Chemistry A* 3 (2015): 17248–17272, https://doi.org/10.1039/C5TA01664A.

215. Y. Zhao, L. Zhang, J. Liu, et al., "Atomic/Molecular Layer Deposition for Energy Storage and Conversion," *Chemical Society Reviews* 50 (2021): 3889–3956, https://doi.org/10.1039/D0CS00156B.

216. V. Vijayakumar, B. Anothumakkool, S. Kurungot, M. Winter, and J. R. Nair, "In Situ Polymerization Process: an Essential Design Tool for Lithium Polymer Batteries," *Energy & Environmental Science* 14 (2021): 2708–2788, https://doi.org/10.1039/D0EE03527K.

217. Q. Liu, L. Wang, and X. He, "Toward Practical Solid-State Polymer Lithium Batteries by in Situ Polymerization Process: a Review," *Advanced Energy Materials* 13 (2023): 2300798, https://doi.org/10.1002/aenm.202300798.

218. F. Liu, Y. Zeng, Z. Li, et al., "A Gel Polymer Electrolyte with Multiple Hydrogen Bonding for Pressure-free Ah Silicon-based Pouch Cells," *Nature Communications* 16 (2025): 11708, https://doi.org/10.1038/s41467-025-66757-x.

219. S. Qin, Y. Yu, J. Zhang, et al., "Separator-Free in Situ Dual-Curing Solid Polymer Electrolytes with Enhanced Interfacial Contact for Achieving Ultrastable Lithium-Metal Batteries," *Advanced Energy Materials* 13 (2023): 2301470, https://doi.org/10.1002/aenm.202301470.

220. A. Zheng, C. Shen, K. Yan, et al., "In Situ Polymerization of Ultra-Thin and Defect-Free Polyamide Layer for Effectively Impeding the Polysulfides Shuttle," *Small* 20 (2024): 2405159, https://doi.org/10.1002/smll.202405159.

221. T. Shen, Q. Yu, J. Wei, et al., "Electrolyte Anion-Initiated in Situ Polymerization of Dioxolane-Derived Gel Electrolytes for Dendrite-Resistant and Separator-Free Lithium Metal Batteries," *Nano Letters* 25 (2025): 10102–10113, https://doi.org/10.1021/acs.nanolett.5c01953.

222. M. Wang, H. Yang, Y. Li, Z. Ding, and R. Liu, "Sequential Kinetic Control of in situ Polymerization Enables a Graded Solid Electrolyte Interphase for ultrasTable Separator-free Solid-state Lithium Metal Batteries," *Nano Energy* 149 (2026): 111743, https://doi.org/10.1016/j.nanoen.2026.111743.

223. B. Yuan, B. Zhao, Q. Wang, et al., "A Thin Composite Polymer Electrolyte with High Room-temperature Conductivity Enables Mass Production for Solid-state Lithium-metal Batteries," *Energy Storage Materials* 47 (2022): 288–296, https://doi.org/10.1016/j.ensm.2022.01.052.

224. A. Hu, W. Chen, F. Li, et al., "Nonflammable Polyfluorides-Anchored Quasi-Solid Electrolytes for Ultra-Safe Anode-Free Lithium Pouch Cells without Thermal Runaway," *Advanced Materials* 35 (2023): 2304762, https://doi.org/10.1002/adma.202304762.

225. T. Zhang, Y. Wang, X. Wang, et al., "In situ construction of Solid Polymer Electrolyte with Regulated Li-polymer Interaction for High-performance Solid-state Li Metal Batteries," *Nano Energy* 139 (2025): 110915, https://doi.org/10.1016/j.nanoen.2025.110915.

226. X. Wang, P. Huang, Y. Zhong, et al., "3D crosslinked Semi-interpenetrating Single-ion Hybrid Electrolytes for Dendrite-free and High-voltage Lithium Metal Batteries," *Chemical Engineering Journal* 522 (2025): 168099, https://doi.org/10.1016/j.cej.2025.168099.

227. Ö. Simsek, P. Zimmer, S. Muench, and U. S. Schubert, "Photopolymerized Gel Polymer Electrolytes with Cyclic Carbonate Side Chains for Li-organic Batteries at Room Temperature," *Journal of Power Sources Advances* 33 (2025): 100176, https://doi.org/10.1016/j.powera.2025.100176.

228. J. R. Nair, I. Shaji, N. Ehteshami, et al., "Solid Polymer Electrolytes for Lithium Metal Battery via Thermally Induced Cationic Ring-Opening Polymerization (CROP) with an Insight into the Reaction Mechanism," *Chemistry of Materials* 31 (2019): 3118–3133, https://doi.org/10.1021/acs.chemmater.8b04172.

229. Y. Wang, R. Xu, B. Xiao, et al., "A Poly(1,3-dioxolane) Based Deep-eutectic Polymer Electrolyte for High Performance Ambient Polymer Lithium Battery," *Materials Today, Physics* 22 (2022): 100620, https://doi.org/10.1016/j.mtphys.2022.100620.

230. W. Zhang, T. Ryu, S. Yoon, et al., "Synthesis and Characterization of Gel Polymer Electrolyte Based on Epoxy Group via Cationic Ring-Open Polymerization for Lithium-Ion Battery," *Membranes* 12 (2022): 439, https://doi.org/10.3390/membranes12040439.

231. Y. Chen, Y. Zhang, J. Niu, et al., "Poly(Ether-Ester)-Based Solid Polymer Electrolytes with High Li-Ion Transference Number for High Voltage All-Solid-State Lithium Metal Batteries," *ACS Applied Energy Materials* 6 (2023): 3113–3125, https://doi.org/10.1021/acsaem.3c00061.

232. R. He, K. Deng, T. Guan, et al., "Initiator-free in situ Synthesized Polymer Electrolytes with High Ionic Conductivity for Dendrite-free Lithium Metal Batteries," *Journal of Colloid and Interface Science* 644 (2023): 230–237, https://doi.org/10.1016/j.jcis.2023.04.084.

233. X. Ye, J. N. Liang, B. R. Du, et al., "Lithium Salt Combining Fluoroethylene Carbonate Initiates Methyl Methacrylate Polymerization Enabling Dendrite-Free Solid-State Lithium Metal Battery," *Energy & Environmental Materials* 7 (2024): 12751, https://doi.org/10.1002/eem2.12751.

234. J. Meng, M. Yin, K. Guo, X. Zhou, and Z. Xue, "In Situ Polymerization in COF Boosts Li-Ion Conduction in Solid Polymer Electrolytes for Li Metal Batteries," *Nano-Micro Letters* 17 (2025): 248, https://doi.org/10.1007/s40820-025-01768-3.

235. T. Cheng, W. Min, M. Wang, et al., "A Deep Eutectic Solvent-based Semi-interpenetrating Polymer Electrolyte for High-voltage Stable Lithium-metal Batteries," *Journal of Materials Chemistry A* 13 (2025): 14392–14400, https://doi.org/10.1039/D5TA00020C.

236. P. Li, X. Liu, Y. Luo, and Z. Rao, "In Situ-polymerized Electrolytes via Molecular Engineering: Synergistic Anion Trapping and Interfacial Stabilization for Long-cycle Lithium Metal Batteries," *Journal of Colloid*

16146840, 2026, 26, Downloaded from https://advanced.onlinelibrary.wiley.com/doi/10.1002/aenm.71073 by Jilin University, Wiley Online Library on [07/11/2026]. See the Terms and Conditions (https://onlinelibrary.wiley.com/terms-and-conditions) on Wiley Online Library for rules of use; OA articles are governed by the applicable Creative Commons License

and Interface Science 700 (2025): 138329, https://doi.org/10.1016/j.jcis.2025.138329.

237. G. Zeng, S. Dai, X. Chen, et al., "Solid-State Graft Polymer Electrolytes with Conductive Backbones and Side Chains for Lithium Batteries," *Macromolecules* 57 (2024): 1258–1265, https://doi.org/10.1021/acs.macromol.3c02150.

238. G.-D. Zhang, L. Fan, L. Bai, M.-H. He, L. Zhai, and S. Mo, "Mesoscopic Simulation Assistant Design of Immiscible Polyimide/BN Blend Films with Enhanced Thermal Conductivity," *Chinese Journal of Polymer Science* 36 (2018): 1394–1402, https://doi.org/10.1007/s10118-018-2155-2.

239. J. Li, F. Peng, H. Li, Z. Ru, J. Fu, and W. Zhu, "Material Evaluation and Dynamic Powder Deposition Modeling of PEEK/CF Composite for Laser Powder Bed Fusion Process," *Polymers* 15 (2023): 2863, https://doi.org/10.3390/polym15132863.

240. C. Wang and Z. Li, "Molecular Conformation and Packing: Their Critical Roles in the Emission Performance of Mechanochromic Fluorescence Materials," *Materials Chemistry Frontiers* 1 (2017): 2174–2194, https://doi.org/10.1039/C7QM00201G.

241. S. Arora, "Selection of Thermal Management System for Modular Battery Packs of Electric Vehicles: a Review of Existing and Emerging Technologies," *Journal of Power Sources* 400 (2018): 621–640, https://doi.org/10.1016/j.jpowsour.2018.08.020.

242. P. Cicconi, P. Kumar, and P. Varshney, "A Support Approach for the Modular Design of Li-ion Batteries: A Test Case with PCM," *Journal of Energy Storage* 31 (2020): 101684, https://doi.org/10.1016/j.est.2020.101684.

243. H. Wang, T. Tao, J. Xu, X. Mei, X. Liu, and P. Gou, "Cooling Capacity of a Novel Modular Liquid-cooled Battery Thermal Management System for Cylindrical lithium-ion battEries," *Applied Thermal Engineering* 178 (2020): 115591, https://doi.org/10.1016/j.applthermaleng.2020.115591.

244. A. M. Divakaran, D. Hamilton, K. N. Manjunatha, and M. Minakshi, "Design, Development and Thermal Analysis of Reusable Li-Ion Battery Module for Future Mobile and Stationary Applications," *Energies* 13 (2020): 1477, https://doi.org/10.3390/en13061477.

245. Z. Li, S. Li, and X. Luo, "An Overview of Calibration Technology of Industrial Robots," *IEEE/CAA Journal of Automatica Sinica* 8 (2021): 23–36, https://doi.org/10.1109/JAS.2020.1003381.

246. F. Ning and W. Cong, "Ultrasonic Vibration-assisted (UV-A) Manufacturing Processes: State of the Art and Future Perspectives," *Journal of Manufacturing Processes* 51 (2020): 174–190, https://doi.org/10.1016/j.jmapro.2020.01.028.

247. G. Gonzalez, I. Roppolo, C. F. Pirri, and A. Chiappone, "Current and Emerging Trends in Polymeric 3D Printed Microfluidic Devices," *Additive Manufacturing* 55 (2022): 102867, https://doi.org/10.1016/j.addma.2022.102867.

248. F. Zou and A. Manthiram, "A Review of the Design of Advanced Binders for High-Performance Batteries," *Advanced Energy Materials* 10 (2020): 2002508, https://doi.org/10.1002/aenm.202002508.

249. J. Yoon, J. Lee, H. Kim, J. Kim, and H.-J. Jin, "Polymeric Binder Design for Sustainable Lithium-Ion Battery Chemistry," *Polymers* 16 (2024): 254, https://doi.org/10.3390/polym16020254.

250. H. Chen, Z. Wu, Z. Su, et al., "A Mechanically Robust Self-healing Binder for Silicon Anode in lithium-ion battEries," *Nano Energy* 81 (2021): 105654, https://doi.org/10.1016/j.nanoen.2020.105654.

251. S. Choi, T.-W. Kwon, A. Coskun, and J. W. Choi, "Highly Elastic Binders Integrating Polyrotaxanes for Silicon Microparticle Anodes in lithium-ion battEries," *Science* 357 (2017): 279–283, https://doi.org/10.1126/science.aal4373.

252. Z. Li, G. Wu, Y. Yang, et al., "An Ion-Conductive Grafted Polymeric Binder with Practical Loading for Silicon Anode with High Interfacial Stability in Lithium-Ion Batteries," *Advanced Energy Materials* 12 (2022): 2201197, https://doi.org/10.1002/aenm.202201197.

253. D. Liu, Y. Zhao, R. Tan, et al., "Novel Conductive Binder for High-performance Silicon Anodes in lithium-ion battEries," *Nano Energy* 36 (2017): 206–212, https://doi.org/10.1016/j.nanoen.2017.04.043.

254. K. G. Araño, B. L. Armstrong, G. Yang, et al., "Elucidating the Role of Carbon Conductive Additive in the Processing and Electrochemical Behavior of Surface-Modified Si Anodes," *Energy & Fuels* 38 (2024): 6446–6458, https://doi.org/10.1021/acs.energyfuels.4c00039.

255. T. M. Higgins, S.-H. Park, P. J. King, et al., "A Commercial Conducting Polymer as both Binder and Conductive Additive for Silicon Nanoparticle-Based Lithium-Ion Battery Negative Electrodes," *ACS Nano* 10 (2016): 3702–3713, https://doi.org/10.1021/acsnano.6b00218.

256. X. Bai, H. Zhang, J. Lin, and G. Zhang, "Durable Silicon-carbon Composites Self-assembled from Double-protected Heterostructure for Lithium-ion Batteries," *Journal of Colloid and Interface Science* 615 (2022): 375–385, https://doi.org/10.1016/j.jcis.2022.01.191.

257. S. Hiwase, N. Kumar, and M. Furquan, "Exceptional Fabrication of Dead-weight-free Silicon and Graphitic Heterostructures Anodes for the next Advancement of Li-ion Batteries," *Chemical Engineering Journal* 498 (2024): 155085, https://doi.org/10.1016/j.cej.2024.155085.

258. R. You, X. Han, Z. Zhang, et al., "An Environmental Friendly Cross-linked Polysaccharide Binder for Silicon Anode in Lithium-ion Batteries," *Ionics* 25 (2019): 4109–4118, https://doi.org/10.1007/s11581-019-02972-z.

259. C. Wang, H. Wu, Z. Chen, M. T. McDowell, Y. Cui, and Z. Bao, "Self-healing Chemistry Enables the Stable Operation of Silicon Microparticle Anodes for High-energy Lithium-ion Batteries," *Nature Chemistry* 5 (2013): 1042–1048, https://doi.org/10.1038/nchem.1802.

260. Y. Wang, H. Xu, X. Chen, H. Jin, and J. Wang, "Novel Constructive Self-healing Binder for Silicon Anodes with High Mass Loading in Lithium-ion Batteries," *Energy Storage Materials* 38 (2021): 121–129, https://doi.org/10.1016/j.ensm.2021.03.003.

261. C. Luo, X. Wu, T. Zhang, et al., "A Four-Armed Polyacrylic Acid Homopolymer Binder with Enhanced Performance for SiO_x/Graphite Anode," *Macromolecular Materials and Engineering* 306 (2021): 2000525, https://doi.org/10.1002/mame.202000525.

262. C. Zhang, Q. Chen, X. Ai, et al., "Conductive Polyaniline Doped with Phytic Acid as a Binder and Conductive Additive for a Commercial Silicon Anode with Enhanced Lithium Storage Properties," *Journal of Materials Chemistry An 8* (2020): 16323–16331, https://doi.org/10.1039/D0TA04389C.

263. S. Zhang, H. Gu, H. Pan, et al., "A Novel Strategy to Suppress Capacity and Voltage Fading of Li- and Mn-Rich Layered Oxide Cathode Material for Lithium-Ion Batteries," *Advanced Energy Materials* 7 (2017): 1601066, https://doi.org/10.1002/aenm.201601066.

264. T. Zhao, Y. Meng, R. Ji, F. Wu, L. Li, and R. Chen, "Maintaining Structure and Voltage Stability of Li-rich Cathode Materials by Green Water-soluble Binders Containing Na_+ Ions," *Journal of Alloys and Compounds* 811 (2019): 152060, https://doi.org/10.1016/j.jallcom.2019.152060.

265. M. Kuenzel, R. Porhiel, D. Bresser, et al., "Deriving Structure-Performance Relations of Chemically Modified Chitosan Binders for Sustainable High-Voltage $LiNi_{0.5}$ $Mn_{1.5}$ O_4 Cathodes," *Batteries & Supercaps* 3 (2020): 155–164, https://doi.org/10.1002/batt.201900140.

266. S. Tanaka, T. Narutomi, S. Suzuki, A. Nakao, H. Oji, and N. Yabuuchi, "Acrylonitrile-grafted Poly(vinyl alcohol) Copolymer as Effective Binder for High-voltage Spinel Positive Electrode," *Journal of Power Sources* 358 (2017): 121–127, https://doi.org/10.1016/j.jpowsour.2017.05.032.

267. S. Lee, E.-Y. Kim, H. Lee, and E.-S. Oh, "Effects of Polymeric Binders on Electrochemical Performances of Spinel Lithium Manganese Oxide Cathodes in lithium-ion battEries," *Journal of Power Sources* 269 (2014): 418–423, https://doi.org/10.1016/j.jpowsour.2014.06.167.

268. G. Li, Y. Liao, Z. He, et al., "A New Strategy to Improve the Cyclic Stability of High Voltage Lithium Nickel Manganese Oxide Cathode by

16146840, 2026, 26, Downloaded from https://advanced.onlinelibrary.wiley.com/doi/10.1002/aenm.71073 by Jilin University, Wiley Online Library on [07/11/2026]. See the Terms and Conditions (https://onlinelibrary.wiley.com/terms-and-conditions) on Wiley Online Library for rules of use; OA articles are governed by the applicable Creative Commons License

Poly(butyl methacrylate-acrylonitrile-styrene) Terpolymer as coBinder in lithium-ion battEries," *Electrochimica Acta* 319 (2019): 527–540, https://doi.org/10.1016/j.electacta.2019.07.011.

269. A. Su, Q. Pang, X. Chen, et al., "Lithium Poly-acrylic Acid as a Fast Li^+ Transport media and a Highly Stable Aqueous Binder for Li_3 V_2 $(PO_4)_3$ Cathode Electrodes," *Journal of Materials Chemistry A* 6 (2018): 23357–23365, https://doi.org/10.1039/C8TA08663J.

270. O. S. Taskin, D. Hubble, T. Zhu, and G. Liu, "Biomass-derived Polymeric Binders in Silicon Anodes for Battery Energy Storage Applications," *Green Chemistry* 23 (2021): 7890–7901, https://doi.org/10.1039/D1GC01814K.

271. A. Wang, S. Kadam, H. Li, S. Shi, and Y. Qi, "Review on Modeling of the Anode Solid Electrolyte Interphase (SEI) for Lithium-ion Batteries," *npj Computational Materials* 4 (2018): 15, https://doi.org/10.1038/s41524-018-0064-0.

272. D. Aurbach, Y. Talyosef, B. Markovsky, et al., "Design of Electrolyte Solutions for Li and Li-ion Batteries: a Review," *Electrochimica Acta* 50 (2004): 247–254, https://doi.org/10.1016/j.electacta.2004.01.090.

273. V. R. Rikka, S. R. Sahu, A. Chatterjee, et al., "In Situ/Ex Situ Investigations on the Formation of the Mosaic Solid Electrolyte Interface Layer on Graphite Anode for Lithium-Ion Batteries," *The Journal of Physical Chemistry C* 122 (2018): 28717–28726, https://doi.org/10.1021/acs.jpcc.8b09210.

274. E. Peled, "The Electrochemical Behavior of Alkali and Alkaline Earth Metals in Nonaqueous Battery Systems—The Solid Electrolyte Interphase Model," *Journal of The Electrochemical Society* 126 (1979): 2047–2051, https://doi.org/10.1149/1.2128859.

275. J. B. Goodenough and Y. Kim, "Challenges for Rechargeable Li Batteries," *Chemistry of Materials* 22 (2010): 587–603, https://doi.org/10.1021/cm901452z.

276. F. A. Soto, Y. Ma, J. M. Martinez de la Hoz, J. M. Seminario, and P. B. Balbuena, "Formation and Growth Mechanisms of Solid-Electrolyte Interphase Layers in Rechargeable Batteries," *Chemistry of Materials* 27 (2015): 7990–8000, https://doi.org/10.1021/acs.chemmater.5b03358.

277. Y. S. Cohen, Y. Cohen, and D. Aurbach, "Micromorphological Studies of Lithium Electrodes in Alkyl Carbonate Solutions Using in Situ Atomic Force Microscopy," *The Journal of Physical Chemistry B* 104 (2000): 12282–12291, https://doi.org/10.1021/jp002526b.

278. S. Shi, P. Lu, Z. Liu, et al., "Direct Calculation of Li-Ion Transport in the Solid Electrolyte Interphase," *Journal of the American Chemical Society* 134 (2012): 15476–15487, https://doi.org/10.1021/ja305366r.

279. H. Adenusi, G. A. Chass, S. Passerini, K. V. Tian, and G. Chen, "Lithium Batteries and the Solid Electrolyte Interphase (SEI)—Progress and Outlook," *Advanced Energy Materials* 13 (2023): 2203307, https://doi.org/10.1002/aenm.202203307.

280. Q. Pang, X. Liang, A. Shyamsunder, and L. F. Nazar, "An in Vivo Formed Solid Electrolyte Surface Layer Enables Stable Plating of Li Metal," *Joule* 1 (2017): 871–886, https://doi.org/10.1016/j.joule.2017.11.009.

281. Y. Zeng, F. Liu, Q. Zhang, et al., "A Thermoresponsive Electrolyte Additive for High-energy, Long-cycling, and Safe Lithium Batteries," *Joule* 9 (2025): 102100, https://doi.org/10.1016/j.joule.2025.102100.

282. Q. Xiong, R. Wang, D. Li, et al., "Covalent and Polyfluorinated Lithium Salt for Stable $LiCoO_2$ Batteries at High Temperature and High Voltage," *Nature Communications* 16 (2025): 10325, https://doi.org/10.1038/s41467-025-65256-3.

283. S.-T. Hong, J.-S. Kim, S.-J. Lim, and W. Y. Yoon, "Surface Characterization of Emulsified Lithium Powder Electrode," *Electrochimica Acta* 50 (2004): 535–539, https://doi.org/10.1016/j.electacta.2004.03.065.

284. S. Shiraishi, K. Kanamura, and Z. Takehara, "Surface Condition Changes in Lithium Metal Deposited in Nonaqueous Electrolyte Containing HF by Dissolution-Deposition Cycles," *Journal of The Electrochemical Society* 146 (1999): 1633–1639, https://doi.org/10.1149/1.1391818.

285. D. Aurbach, M. L. Daroux, P. W. Faguy, and E. Yeager, "Identification of Surface Films Formed on Lithium in Propylene Carbonate Solutions," *Journal of The Electrochemical Society* 134 (1987): 1611–1620, https://doi.org/10.1149/1.2100722.

286. E. Peled, D. Golodnitsky, and G. Ardel, "Advanced Model for Solid Electrolyte Interphase Electrodes in Liquid and Polymer Electrolytes," *Journal of The Electrochemical Society* 144 (1997): L208, https://doi.org/10.1149/1.1837858.

287. K. Xu, "Electrolytes and Interphases in Li-Ion Batteries and beyond," *Chemical Reviews* 114 (2014): 11503–11618, https://doi.org/10.1021/cr500003w.

288. J. Zheng, Z. Ju, B. Zhang, et al., "Lithium Ion Diffusion Mechanism on the Inorganic Components of the Solid–electrolyte Interphase," *Journal of Materials Chemistry A* 9 (2021): 10251–10259, https://doi.org/10.1039/D0TA11444H.

289. P. Zhai, L. Liu, X. Gu, T. Wang, and Y. Gong, "Interface Engineering for Lithium Metal Anodes in Liquid Electrolyte," *Advanced Energy Materials* 10 (2020): 2001257, https://doi.org/10.1002/aenm.202001257.

290. D. Lu, R. Li, L. Lv, et al., "Tailoring Cathode Interphase Chemistry for High-Voltage Li-ion Batteries," *Angewandte Chemie International Edition* 65 (2026): 18546, https://doi.org/10.1002/anie.202518546.

291. Q. Li, H. Pan, W. Li, et al., "Homogeneous Interface Conductivity for Lithium Dendrite-Free Anode," *ACS Energy Letters* 3 (2018): 2259–2266, https://doi.org/10.1021/acsenergylett.8b01244.

292. X.-Q. Zhang, X. Chen, L.-P. Hou, et al., "Regulating Anions in the Solvation Sheath of Lithium Ions for Stable Lithium Metal Batteries," *ACS Energy Letters* 4 (2019): 411–416, https://doi.org/10.1021/acsenergylett.8b02376.

293. K. Chen, R. Pathak, A. Gurung, et al., "Flower-shaped Lithium Nitride as a Protective Layer via Facile Plasma Activation for Stable Lithium Metal Anodes," *Energy Storage Materials* 18 (2019): 389–396, https://doi.org/10.1016/j.ensm.2019.02.006.

294. X. Fan, X. Ji, F. Han, et al., "Fluorinated Solid Electrolyte Interphase Enables Highly Reversible Solid-state Li Metal Battery," *Science Advances* 4: aau9245, https://doi.org/10.1126/sciadv.aau9245.

295. Y. Gao, Y. Zhao, Y. C. Li, Q. Huang, T. E. Mallouk, and D. Wang, "Interfacial Chemistry Regulation via a Skin-Grafting Strategy Enables High-Performance Lithium-Metal Batteries," *Journal of the American Chemical Society* 139 (2017): 15288–15291, https://doi.org/10.1021/jacs.7b06437.

296. B. Tong, J. Wang, Z. Liu, et al., "$(CH_3)_3$Si-N[(FSO_2)(n-$C_4F_9SO_2$)]: an Additive for Dendrite-free Lithium Metal Anode," *Journal of Power Sources* 400 (2018): 225–231, https://doi.org/10.1016/j.jpowsour.2018.08.007.

297. Y. Liu, Y.-K. Tzeng, D. Lin, et al., "An Ultrastrong Double-Layer Nanodiamond Interface for Stable Lithium Metal Anodes," *Joule* 2 (2018): 1595–1609, https://doi.org/10.1016/j.joule.2018.05.007.

298. G. Zheng, S. W. Lee, Z. Liang, et al., "Interconnected Hollow Carbon Nanospheres for Stable Lithium Metal Anodes," *Nature Nanotechnology* 9 (2014): 618–623, https://doi.org/10.1038/nnano.2014.152.

299. Z. Liang, G. Zheng, C. Liu, et al., "Polymer Nanofiber-Guided Uniform Lithium Deposition for Battery Electrodes," *Nano Letters* 15 (2015): 2910–2916, https://doi.org/10.1021/nl5046318.

300. E. Cha, M. D. Patel, J. Park, et al., "Publisher Correction: 2D MoS2 as an Efficient Protective Layer for Lithium Metal Anodes in High-performance Li–S Batteries," *Nature Nanotechnology* 13 (2018): 521–521, https://doi.org/10.1038/s41565-018-0095-1.

301. W. Zhang, H. L. Zhuang, L. Fan, L. Gao, and Y. Lu, "A "–Cationanion Regulation" Synergistic Anode Host for Dendrite-free Lithium Metal Batteries," *Science Advances* 4: aar4410, https://doi.org/10.1126/sciadv.aar4410.

302. M. G. S. R. Thomas, P. G. Bruce, and J. B. Goodenough, "AC Impedance Analysis of Polycrystalline Insertion Electrodes: Application

16146840, 2026, 26, Downloaded from https://advanced.onlinelibrary.wiley.com/doi/10.1002/aenm.71073 by Jilin University, Wiley Online Library on [07/11/2026]. See the Terms and Conditions (https://onlinelibrary.wiley.com/terms-and-conditions) on Wiley Online Library for rules of use; OA articles are governed by the applicable Creative Commons License

to Li_{1-x} CoO_2," *Journal of The Electrochemical Society* 132 (1985): 1521–1528, https://doi.org/10.1149/1.2114158.

303. K. Kanamura, S. Toriyama, S. Shiraishi, M. Ohashi, and Z.-I. Takehara, "Studies on Electrochemical Oxidation of nonAqueous Electrolyte on the LiCoO2 Thin Film Electrode," *Journal of Electroanalytical Chemistry* 419 (1996): 77–84, https://doi.org/10.1016/S0022-0728(96)04862-0.

304. Q. Zhou, J. Ma, S. Dong, X. Li, and G. Cui, "Intermolecular Chemistry in Solid Polymer Electrolytes for High-Energy-Density Lithium Batteries," *Advanced Materials* 31 (2019): 1902029, https://doi.org/10.1002/adma.201902029.

305. S. Fang, D. Jackson, M. L. Dreibelbis, T. F. Kuech, and R. J. Hamers, "Anode-originated SEI Migration Contributes to Formation of Cathode-electrolyte Interphase Layer," *Journal of Power Sources* 373 (2018): 184–192, https://doi.org/10.1016/j.jpowsour.2017.09.050.

306. J.-N. Zhang, Q. Li, Y. Wang, J. Zheng, X. Yu, and H. Li, "Dynamic Evolution of Cathode Electrolyte Interphase (CEI) on High Voltage $LiCoO_2$ Cathode and Its Interaction with Li Anode," *Energy Storage Materials* 14 (2018): 1–7, https://doi.org/10.1016/j.ensm.2018.02.016.

307. Z. Wu, R. Li, S. Zhang, et al., "Deciphering and Modulating Energetics of Solvation Structure Enables Aggressive High-voltage Chemistry of Li Metal Batteries," *Chem* 9 (2023): 650–664, https://doi.org/10.1016/j.chempr.2022.10.027.

308. S. Wang, A. Dai, Y. Cao, et al., "Enabling Stable and High-rate Cycling of a Ni-rich Layered Oxide Cathode for Lithium-ion Batteries by Modification with an Artificial Li^+ -conducting Cathode-electrolyte Interphase," *Journal of Materials Chemistry A* 9 (2021): 11623–11631, https://doi.org/10.1039/D1TA02563E.

309. Y. Qiao, Z. Zhou, Z. Chen, et al., "Visualizing Ion Diffusion in Battery Systems by Fluorescence Microscopy: a Case Study on the Dissolution of LiMn2O4," *Nano Energy* 45 (2018): 68–74, https://doi.org/10.1016/j.nanoen.2017.12.036.

310. X. Li, K. Zhang, D. Mitlin, et al., "Li-Rich $Li[Li_{1/6}$ $Fe_{1/6}$ $Ni_{1/6}$ $Mn_{1/2}$ $]O_2$ (LFNMO) Cathodes: Atomic Scale Insight on the Mechanisms of Cycling Decay and of the Improvement due to Cobalt Phosphate Surface Modification," *Small* 14 (2018): 1802570, https://doi.org/10.1002/smll.201802570.

311. X.-W. Gao, Y.-F. Deng, D. Wexler, et al., "Improving the Electrochemical Performance of the $LiNi_{0.5}$ $Mn_{1.5}$ O_4 Spinel by Polypyrrole Coating as a Cathode Material for the Lithium-ion Battery," *Journal of Materials Chemistry A* 3 (2015): 404–411, https://doi.org/10.1039/C4TA04018J.

312. J.-F. Ding, R. Xu, N. Yao, et al., "Non-Solvating and Low-Dielectricity Cosolvent for Anion-Derived Solid Electrolyte Interphases in Lithium Metal Batteries," *Angewandte Chemie International Edition* 60 (2021): 11442–11447, https://doi.org/10.1002/anie.202101627.

313. J. Huang, J. Liu, J. He, et al., "Optimizing Electrode/Electrolyte Interphases and Li-Ion Flux/Solvation for Lithium-Metal Batteries with Qua-Functional Heptafluorobutyric Anhydride," *Angewandte Chemie International Edition* 60 (2021): 20717–20722, https://doi.org/10.1002/anie.202107957.

314. G. Jiang, J. Liu, Z. Wang, and J. Ma, "Stable Non-Flammable Phosphate Electrolyte for Lithium Metal Batteries via Solvation Regulation by the Additive," *Advanced Functional Materials* 33 (2023): 2300629, https://doi.org/10.1002/adfm.202300629.

315. P. C. Rath, Y.-W. Wang, J. Patra, et al., "Composition Manipulation of Bis(fluorosulfonyl)Imide-based Ionic Liquid Electrolyte for High-voltage Graphite//$LiNi_{0.5}Mn_{1.5}O_4$ Lithium-ion Batteries," *Chemical Engineering Journal* 415 (2021): 128904, https://doi.org/10.1016/j.cej.2021.128904.

316. J. Xia, R. Petibon, A. Xiao, W. M. Lamanna, and J. R. Dahn, "Some Fluorinated Carbonates as Electrolyte Additives for $Li(Ni_{0.4}Mn_{0.4}Co_{0.2})O_2$/Graphite Pouch Cells," *Journal of The Electrochemical Society* 163 (2016): A1637, https://doi.org/10.1149/2.0831608jes.

317. Y. Song, Q. Mao, Q. Li, et al., "Structure Property and Reaction Mechanism of Boron-Based High-Voltage Electrolyte Additives via First-Principles Calculations," *ACS Applied Energy Materials* 6 (2023): 4271–4282, https://doi.org/10.1021/acsaem.3c00196.

318. M. Xu, Y. Liu, B. Li, W. Li, X. Li, and S. Hu, "Tris (pentafluorophenyl) Phosphine: an Electrolyte Additive for High Voltage Li-ion Batteries," *Electrochemistry Communications* 18 (2012): 123–126, https://doi.org/10.1016/j.elecom.2012.02.037.

319. T. D. Pham, A. Bin Faheem, J. Kim, K. Kwak, and K.-K. Lee, "Nonflammable Electrolytes Based on a Fluorine-free Salt for Safe and High-voltage Lithium Metal Batteries," *Electrochimica Acta* 458 (2023): 142496, https://doi.org/10.1016/j.electacta.2023.142496.

320. E. Winter, M. Briccola, T. J. Schmidt, and S. Trabesinger, "Enabling $LiNO_3$ in Carbonate Electrolytes by Flame-retardant Electrolyte Additive as a Cosolvent for Enhanced Performance of Lithium Metal Batteries," *Applied Research* 3 (2024): 202200096, https://doi.org/10.1002/appl.202200096.

321. Q. Ma, X. Zhang, A. Wang, Y. Xia, X. Liu, and J. Luo, "Stabilizing Solid Electrolyte Interphases on both Anode and Cathode for High Areal Capacity, High-Voltage Lithium Metal Batteries with High Li Utilization and Lean Electrolyte," *Advanced Functional Materials* 30 (2020): 2002824, https://doi.org/10.1002/adfm.202002824.

322. Y.-P. Yang, J.-C. Jiang, A.-C. Huang, et al., "3-(Trifluoromethyl)benzoylacetonitrile: a iMultfunctional Safe Electrolyte Additive for $LiNi_{0.8}Co_{0.1}Mn_{0.1}O_2$ Cathode of High Voltage Lithium-ion Battery," *Process Safety and Environmental Protection* 160 (2022): 80–90, https://doi.org/10.1016/j.psep.2022.02.018.

323. Y. Fei and G. Li, "Unveiling the Pivotal Parameters for Advancing High Energy Density in Lithium-Sulfur Batteries: a Comprehensive Review," *Advanced Functional Materials* 34 (2024): 2312550, https://doi.org/10.1002/adfm.202312550.

324. B. Réty, H.-Y. Yiin, and C. M. Ghimbeu, "Quantification of Activated Carbon Functional Groups and Active Surface Area by TPD-MS and Their Impact on Supercapacitor Performance," *Energy Storage Materials* 74 (2025): 103963, https://doi.org/10.1016/j.ensm.2024.103963.

325. R. Khan, C. Ryu, H. M. Do, and J. B. In, "Fabrication of Functional Laser-induced Graphene Using Gelatin-2,6-diaminoanthraquinone Coating for High-performance oMicrsupercapacitor," *Journal of Power Sources* 621 (2024): 235305, https://doi.org/10.1016/j.jpowsour.2024.235305.

326. W. Yue, Z. Yu, X. Zhang, H. Liu, Z. Chen, and X. Ma, "Natural N/O/S coDoped Defect-rich Functional Carbon Materials for Aqueous Supercapacitors: Effect Mechanism of N-containing Functional Groups on Chemical Activation," *Applied Surface Science* 677 (2024): 161012, https://doi.org/10.1016/j.apsusc.2024.161012.

327. F. Wang, L. Zhang, Q. Zhang, et al., "Electrode Thickness Design toward Bulk Energy Storage Devices with High Areal/Volumetric Energy Density," *Applied Energy* 289 (2021): 116734, https://doi.org/10.1016/j.apenergy.2021.116734.

328. Z. Zhao, M. Sun, W. Chen, et al., "Sandwich, Vertical-Channeled Thick Electrodes with High Rate and Cycle Performance," *Advanced Functional Materials* 29 (2019): 1809196, https://doi.org/10.1002/adfm.201809196.

329. J. Huang, B. Zhao, T. Liu, et al., "Wood-Derived Materials for Advanced Electrochemical Energy Storage Devices," *Advanced Functional Materials* 29 (2019): 1902255, https://doi.org/10.1002/adfm.201902255.

330. Y. Kuang, C. Chen, D. Kirsch, and L. Hu, "Thick Electrode Batteries: Principles, Opportunities, and Challenges," *Advanced Energy Materials* 9 (2019): 1901457, https://doi.org/10.1002/aenm.201901457.

331. Y. Si, X. Wang, L. Dou, J. Yu, and B. Ding, "Ultralight and Fire-resistant Ceramic Nanofibrous Aerogels with Temperature-invariant Superelasticity," *Science Advances* 4 (2018): aas8925, https://doi.org/10.1126/sciadv.aas8925.

16146840, 2026, 26, Downloaded from https://advanced.onlinelibrary.wiley.com/doi/10.1002/aenm.71073 by Jilin University, Wiley Online Library on [07/11/2026]. See the Terms and Conditions (https://onlinelibrary.wiley.com/terms-and-conditions) on Wiley Online Library for rules of use; OA articles are governed by the applicable Creative Commons License

332. J. Wu, X. Zhang, Z. Ju, et al., "From Fundamental Understanding to Engineering Design of High-Performance Thick Electrodes for Scalable Energy-Storage Systems," *Advanced Materials* 33 (2021): 2101275, https://doi.org/10.1002/adma.202101275.

333. N. Shahrubudin, T. C. Lee, and R. Ramlan, "An Overview on 3D Printing Technology: Technological, Materials, and Applications," *Procedia Manufacturing* 35 (2019): 1286–1296, https://doi.org/10.1016/j.promfg.2019.06.089.

334. F. Shen, C. Tang, X. Sun, Y. Song, and J. Cai, "Recent Advances in 3D Printing Technologies for Lithium-Sulfur Batteries," *Small* 21 (2025): 2412182, https://doi.org/10.1002/smll.202412182.

335. X. Gao, M. Zheng, X. Yang, R. Sun, J. Zhang, and X. Sun, "Emerging Application of 3D-printing Techniques in Lithium Batteries: from Liquid to Solid," *Materials Today* 59 (2022): 161–181, https://doi.org/10.1016/j.mattod.2022.07.016.

336. Q. Xu, N. Chu, Y. Wang, et al., "3D Printed Low-Tortuosity and Ultra-Thick Hierarchical Porous Electrodes for High-Performance Wearable Quasi-Solid-State Zn-VOH Batteries," *Advanced Science* 12 (2025): 2401660, https://doi.org/10.1002/advs.202401660.

337. R. Yuan, S. Sun, S. Ling, et al., "Solvent Exchange Assisted 3D Printing of Low Tortuosity Thick Electrode for High Areal Energy Density and Power Density Supercapacitors," *Carbon* 218 (2024): 118737, https://doi.org/10.1016/j.carbon.2023.118737.

338. M. Li, S. Zhou, L. Cheng, et al., "Vertical-channel Hierarchically Porous 3D Printed Electrodes with Ultrahigh Mass Loading and Areal Energy Density for Li-ion Batteries," *Energy Storage Materials* 72 (2024): 103754, https://doi.org/10.1016/j.ensm.2024.103754.

339. M. Li, H. Lu, X. Wang, et al., "Regulable Mixed-Solvent-Induced Phase Separation in Hydrogels for Information Encryption," *Small* 18 (2022): 2205359, https://doi.org/10.1002/smll.202205359.

340. Z. Wang, W. Qiu, and Q. Zhang, "Constructing Phase Separation in Polymer Gels: Strategies, Functions and Applications," *Progress in Polymer Science* 154 (2024): 101847, https://doi.org/10.1016/j.progpolymsci.2024.101847.

341. L. Song and W. Chu, "Electrodes for Li-ion Batteries: from High-voltage $LiCoO_2$ to CoReduced/Co-free Layered Oxides with Potential Anodes," *Nano Research* 16 (2023): 12983–13007, https://doi.org/10.1007/s12274-023-6239-4.

342. J. Wu, Z. Ju, X. Zhang, et al., "Low-Tortuosity Thick Electrodes with Active Materials Gradient Design for Enhanced Energy Storage," *ACS Nano* 16 (2022): 4805–4812, https://doi.org/10.1021/acsnano.2c00129.

343. L. Li, R. M. Erb, J. Wang, J. Wang, and Y.-M. Chiang, "Fabrication of Low-Tortuosity Ultrahigh-Area-Capacity Battery Electrodes through Magnetic Alignment of Emulsion-Based Slurries," *Advanced Energy Materials* 9 (2019): 1802472, https://doi.org/10.1002/aenm.201802472.

344. P. Lu, Y. Yang, B. Luo, et al., "Multiscale Structural Strong yet Tough Triboelectric Materials Enabled by in Situ Microphase Separation," *Advanced Functional Materials* 35 (2025): 2418336, https://doi.org/10.1002/adfm.202418336.

345. Z. Lv, M. Yue, M. Ling, et al., "Controllable Design Coupled with Finite Element Analysis of Low-Tortuosity Electrode Architecture for Advanced Sodium-Ion Batteries with Ultra-High Mass Loading," *Advanced Energy Materials* 11 (2021): 2003725, https://doi.org/10.1002/aenm.202003725.

346. G. Shao, D. A. H. Hanaor, X. Shen, and A. Gurlo, "Freeze Casting: from Low-Dimensional Building Blocks to Aligned Porous Structures—A Review of Novel Materials, Methods, and Applications," *Advanced Materials* 32 (2020): 1907176, https://doi.org/10.1002/adma.201907176.

347. Y.-Z. Zhang, Y. Wang, Q. Jiang, J. K. El-Demellawi, H. Kim, and H. N. Alshareef, "MXene Printing and Patterned Coating for Device Applications," *Advanced Materials* 32 (2020): 1908486, https://doi.org/10.1002/adma.201908486.

348. T. Ma, D. Wu, Z. Wang, et al., "In situ cathode Coating for all-solid-state Batteries by Freeze-drying Technology," *Nano Energy* 124 (2024): 109522, https://doi.org/10.1016/j.nanoen.2024.109522.

349. J. Zhang, K. Wang, P. Lu, et al., "Wood-like Low-Tortuosity Thick Electrode for Micro-Redoxcapacitor with Ultrahigh Areal Energy Density and Steady Power Output," *Advanced Functional Materials* 34 (2024): 2310775, https://doi.org/10.1002/adfm.202310775.

350. W. Ma, H. Wu, T. Long, et al., "Bamboo Inspired Silicon Anodes with Ultrahigh Initial Coulombic Efficiency and High Capacity for the Li-Ion Batteries," *Small* 20 (2024): 2308109, https://doi.org/10.1002/smll.202308109.

351. C. Huang, M. Dontigny, K. Zaghib, and P. S. Grant, "Low-tortuosity and Graded lithium-ion battEry Cathodes by Ice Templating," *Journal of Materials Chemistry A* 7 (2019): 21421–21431, https://doi.org/10.1039/C9TA07269A.

352. Z. Han, S. Li, R. Xiong, et al., "Low Tortuosity and Reinforced Concrete Type Ultra-Thick Electrode for Practical Lithium–Sulfur Batteries," *Advanced Functional Materials* 32 (2022): 2108669, https://doi.org/10.1002/adfm.202108669.

353. S. Li, G. Tian, R. Xiong, et al., "Enhanced Homogeneity of Electrochemical Reaction via Low Tortuosity Enabling High-voltage Nickel-rich Layered Oxide Thick-electrode," *Energy Storage Materials* 46 (2022): 443–451, https://doi.org/10.1016/j.ensm.2022.01.035.

354. Y.-C. Yin, Z.-L. Yu, Z.-Y. Ma, et al., "Bioinspired Low-tortuosity Carbon Host for High-performance Lithium-metal Anode," *National Science Review* 6 (2018): 247–256, https://doi.org/10.1093/nsr/nwy148.

355. H. Wang, D. Yan, H. Y. Liu, et al., "A Non-Concentrated Gradient-Solvation Electrolyte Enables a High-Voltage Lithium Metal Battery with 447.6 Wh kg^{-1}," *Advanced Materials* 37 (2025): 2509760, https://doi.org/10.1002/adma.202509760.

356. P. Ding, H. Yuan, L. Xu, et al., "Coordination Regulation Enabling Deep Eutectic Electrolyte for Fast-Charging High-Voltage Lithium Metal Batteries," *Advanced Materials* 37 (2025): 2413654, https://doi.org/10.1002/adma.202413654.

357. Z. Tian, Y. Zou, G. Liu, et al., "Electrolyte Solvation Structure Design for Sodium Ion Batteries," *Advanced Science* 9 (2022): 2201207, https://doi.org/10.1002/advs.202201207.

358. S. Wang, H. Xu, W. Li, A. Dolocan, and A. Manthiram, "Interfacial Chemistry in Solid-State Batteries: Formation of Interphase and Its Consequences," *Journal of the American Chemical Society* 140 (2018): 250–257, https://doi.org/10.1021/jacs.7b09531.

359. J. Wang, Y. Yamada, K. Sodeyama, C. H. Chiang, Y. Tateyama, and A. Yamada, "Superconcentrated Electrolytes for a High-voltage Lithium-ion Battery," *Nature Communications* 7 (2016): 12032, https://doi.org/10.1038/ncomms12032.

360. Y. Jin, S. Li, A. Kushima, et al., "Self-healing SEI Enables Full-cell Cycling of a Silicon-majority Anode with a Coulombic Efficiency Exceeding 99.9%," *Energy & Environmental Science* 10 (2017): 580–592, https://doi.org/10.1039/C6EE02685K.

361. J. Zheng, M. H. Engelhard, D. Mei, et al., "Electrolyte Additive Enabled Fast Charging and Stable Cycling Lithium Metal Batteries," *Nature Energy* 2 (2017): 17012, https://doi.org/10.1038/nenergy.2017.12.

362. C. Jing, S. Tao, B. Fu, et al., "Layered Double Hydroxide-based Nanomaterials for Supercapacitors and Batteries: Strategies and Mechanisms," *Progress in Materials Science* 150 (2025): 101410, https://doi.org/10.1016/j.pmatsci.2024.101410.

363. S. Sikiru, T. T. Dele-Afolabi, M. Yeganeh Ghotbi, and Z. U. Rehman, "Recent Advancements in Technology Projection on Electric Double Layer Effect in Battery Recycling for Energy Storage," *Journal of Power Sources* 596 (2024): 234056, https://doi.org/10.1016/j.jpowsour.2024.234056.

364. Z. W. Zhao, P. C. Li, Y. X. Wu, Z. W. Chai, H. Zhang, and G. Li, "Fluorinated Interphase Enabled by Lithium Salt-Driven Electrical

16146840, 2026, 26, Downloaded from https://advanced.onlinelibrary.wiley.com/doi/10.1002/aenm.71073 by Jilin University, Wiley Online Library on [07/11/2026]. See the Terms and Conditions (https://onlinelibrary.wiley.com/terms-and-conditions) on Wiley Online Library for rules of use; OA articles are governed by the applicable Creative Commons License

Double-Layer Modulation for Advanced Zinc Metal Batteries," *Advanced Functional Materials* 35 (2025): 2506270, https://doi.org/10.1002/adfm.202506270.

365. C. Cao, L. Bai, S. Cao, et al., "Structural and Transport Properties of LiTFSI/G_3 Electrolyte with Machine-Learned Molecular Dynamics," *The Journal of Physical Chemistry C* 129 (2025): 13030–13039, https://doi.org/10.1021/acs.jpcc.5c02287.

366. S. Mohapatra, H. Teherpuria, S. S. Paul Chowdhury, et al., "Ion Transport Mechanisms in Pectin-containing EC–LiTFSI Electrolytes," *Nanoscale* 16 (2024): 3144–3159, https://doi.org/10.1039/D3NR04029A.

367. Z. Cao, X. Zheng, Q. Qu, Y. Huang, and H. Zheng, "Electrolyte Design Enabling a High-Safety and High-Performance Si Anode with a Tailored Electrode–Electrolyte Interphase," *Advanced Materials* 33 (2021): 2103178, https://doi.org/10.1002/adma.202103178.

368. H. Ji, J. Xiang, Y. Li, et al., "Liquid–liquid Interfacial Tension Stabilized Li-metal Batteries," *Nature* 643 (2025): 1255–1262, https://doi.org/10.1038/s41586-025-09293-4.

369. J. Xiao, Q. Li, Y. Bi, et al., "Understanding and Applying Coulombic Efficiency in Lithium Metal Batteries," *Nature Energy* 5 (2020): 561–568, https://doi.org/10.1038/s41560-020-0648-z.

370. D. Park and D.-W. Kim, "In-Vitro Alloyable Unidimensional Polymeric Interface to Mitigate Pulverization and Dendritic Growth for Long Lifespan Lithium Metal Batteries," *Advanced Energy Materials* 15 (2025): 2403525, https://doi.org/10.1002/aenm.202403525.

371. C.-H. Jo, K.-S. Sohn, and S.-T. Myung, "Feasible Approaches for Anode-free Lithium-metal Batteries as next Generation Energy Storage Systems," *Energy Storage Materials* 57 (2023): 471–496, https://doi.org/10.1016/j.ensm.2023.02.040.

372. J. Pokharel, A. Cresce, B. Pant, et al., "Manipulating the Diffusion Energy Barrier at the Lithium Metal Electrolyte Interface for Dendrite-free Long-life Batteries," *Nature Communications* 15 (2024): 3085, https://doi.org/10.1038/s41467-024-47521-z.

373. X. Fan and C. Wang, "High-voltage Liquid Electrolytes for Li Batteries: Progress and Perspectives," *Chemical Society Reviews* 50 (2021): 10486–10566, https://doi.org/10.1039/D1CS00450F.

374. K. Chen, X. Shen, L. Luo, et al., "Correlating the Solvating Power of Solvents with the Strength of Ion-Dipole Interaction in Electrolytes of Lithium-ion Batteries," *Angewandte Chemie International Edition* 62 (2023): 202312373, https://doi.org/10.1002/anie.202312373.

375. Y. Lu, W. Zhang, S. Liu, et al., "Tuning the Li^+ Solvation Structure by a "Bulky Coordinating" Strategy Enables Nonflammable Electrolyte for Ultrahigh Voltage Lithium Metal Batteries," *ACS Nano* 17 (2023): 9586–9599, https://doi.org/10.1021/acsnano.3c02948.

376. K.-F. Ren, Y.-F. Du, J.-X. Guo, et al., "Multianion Electrolyte Modulates the Interactions in Solvation Structure to Construct Robust Lithium Metal Batteries," *Journal of Energy Chemistry* 104 (2025): 36–43, https://doi.org/10.1016/j.jechem.2024.12.018.

377. S. Chen, W. Zhu, L. Tan, et al., "Strongly Solvating Ether Electrolytes for High-Voltage Lithium Metal Batteries," *ACS Applied Materials & Interfaces* 15 (2023): 13155–13164, https://doi.org/10.1021/acsami.3c00165.

378. W. Chen, S. Guo, L. Qin, et al., "Hydrogen Bond-Functionalized Massive Solvation Modules Stabilizing Bilateral Interfaces," *Advanced Functional Materials* 32 (2022): 2112609, https://doi.org/10.1002/adfm.202112609.

379. F. Chen, S. J. Robertson, X. Xu, et al., "Interface Regulation Strategy in Constructing ZnS@MoS2 Heterostructure with Enhanced Surface Reaction Dynamics for Robust Lithium-ion Storage," *Nano Energy* 123 (2024): 109414, https://doi.org/10.1016/j.nanoen.2024.109414.

380. B. Jiang, C. Zhao, Y. Zhang, S. Gu, and N. Zhang, "Atomic-Scale Interface Engineering to Construct Highly Efficient Electrocatalysts for Advanced Lithium–Sulfur Batteries," *ACS Nano* 19 (2025): 18332–18346, https://doi.org/10.1021/acsnano.5c00855.

381. S. Guo, J. Wang, Y. Sun, L. Peng, and C. Li, "Interface Engineering of Co_3O_4/CeO_2 Heterostructure in situ Embedded in Co/N-Doped Carbon Nanofibers Integrating Oxygen Vacancies as Effective Oxygen Cathode Catalyst for Li-O_2 Battery," *Chemical Engineering Journal* 452 (2023): 139317, https://doi.org/10.1016/j.cej.2022.139317.

382. W. Guo, Y. Zhang, L. Lin, et al., "Regulation of Interfacial Lattice Oxygen Activity by Full-Surface Modification Engineering Toward Long Cycling Stability for Co-Free Li-Rich Mn-Based Cathode," *Small* 19 (2023): 2300175, https://doi.org/10.1002/smll.202300175.

383. H. Ji, C. Xie, R. Zhang, et al., "Sodiophilic Interface and Electrolyte Regulation Boost the Lifespan of Anode-Free Sodium Battery," *SusMat* 5 (2025): 258, https://doi.org/10.1002/sus2.258.

384. H. W. Bi, X. Sun, B. Y. Zhao, et al., "Tailoring Cathode Interfaces in Sodium-Ion Batteries: Advanced Coating Strategies and Electrochemical Interface Regulation," *Advanced Functional Materials* 35 (2025): 07781, https://doi.org/10.1002/adfm.202507781.

385. P. Liang, H. Sun, C.-L. Huang, et al., "A Nonflammable High-Voltage 4.7 V Anode-Free Lithium Battery," *Advanced Materials* 34 (2022): 2207361, https://doi.org/10.1002/adma.202207361.

386. J. Zhang, H. Zhang, L. Deng, et al., "An Additive-enabled Ether-based Electrolyte to Realize Stable Cycling of High-voltage Anode-free Lithium Metal Batteries," *Energy Storage Materials* 54 (2023): 450–460, https://doi.org/10.1016/j.ensm.2022.10.052.

387. H. Liu, Z. Zhu, Q. Yan, et al., "A Disordered Rock Salt Anode for Fast-charging Lithium-ion Batteries," *Nature* 585 (2020): 63–67, https://doi.org/10.1038/s41586-020-2637-6.

388. J. H. Ha, M. Kang, H. Cha, et al., "Highly Crystalline Contorted Coronene Homologous Molecule as Superior Organic Anode Material for Full-Cell Li-Ion Batteries," *ACS Nano* 19 (2025): 2475–2483, https://doi.org/10.1021/acsnano.4c13561.

389. Z. Wu, J. Tao, L. Lin, et al., "Toward High-Performance Lithium-Ion Batteries via Voltage Modulation of Silicon Anodes," *Carbon Neutralization* 4 (2025): 70052, https://doi.org/10.1002/cnl2.70052.

390. W. Yang, Z. Zhang, X. Sun, et al., "Tailoring the Electrode-Electrolyte Interface for Reliable Operation of all-Climate 4.8 V Li||NCM811 Batteries," *Angewandte Chemie International Edition* 63 (2024): 202410893, https://doi.org/10.1002/anie.202410893.

391. Y. Zhang, L. Zeng, Z. Ding, W. Wu, L. Deng, and L. Yao, "Stable Electrode/Electrolyte Interfaces Regulated by Dual-salt and Localized High-concentration Strategies for High-voltage Lithium Metal Batteries," *Chemical Communications* 59 (2023): 12593–12596, https://doi.org/10.1039/D3CC02705H.

392. L. Lin, K. Qin, M. Li, et al., "Spinel-related Li2Ni0.5Mn1.5O4 Cathode for 5-V Anode-free Lithium Metal Batteries," *Energy Storage Materials* 45 (2022): 821–827, https://doi.org/10.1016/j.ensm.2021.12.036.

393. Q. Wang, B. Hong, M. Wang, J. Li, Z. Zhang, and Y. Lai, "Fluorinated Functional Groups Enhanced Composite in situ Gel Electrolytes for High Voltage Cathode of Quasi Solid-state Lithium Battery," *Journal of Power Sources* 624 (2024): 235501, https://doi.org/10.1016/j.jpowsour.2024.235501.

394. A.-M. Li, Z. Wang, T. P. Pollard, et al., "High Voltage Electrolytes for Lithium-ion Batteries with oMicrsized Silicon Anodes," *Nature Communications* 15 (2024): 1206, https://doi.org/10.1038/s41467-024-45374-0.

395. J. Du, G. Li, Y. Tan, et al., "Tuning the Li–Sn Alloy Dispersity to Improve the Lithiophilicity of Lithium Metal Anodes Toward Stable Lithium Metal Batteries," *Inorganic Chemistry Frontiers* 12 (2025): 3137–3146, https://doi.org/10.1039/D4QI02971B.

396. X. Peng, J. Han, Q. Zhang, Y. Xiang, and X. Hu, "Real-time Mechanical and Thermal Monitoring of Lithium Batteries with PVDF-TrFE Thin Films Integrated within the Battery," *Sensors and Actuators A: Physical* 338 (2022): 113484, https://doi.org/10.1016/j.sna.2022.113484.

16146840, 2026, 26, Downloaded from https://advanced.onlinelibrary.wiley.com/doi/10.1002/aenm.71073 by Jilin University, Wiley Online Library on [07/11/2026]. See the Terms and Conditions (https://onlinelibrary.wiley.com/terms-and-conditions) on Wiley Online Library for rules of use; OA articles are governed by the applicable Creative Commons License

397. M. H. Parekh, B. Li, M. Palanisamy, T. E. Adams, V. Tomar, and V. G. Pol, "In Situ Thermal Runaway Detection in Lithium-Ion Batteries with an Integrated Internal Sensor," *ACS Applied Energy Materials* 3 (2020): 7997–8008, https://doi.org/10.1021/acsaem.0c01392.

398. S. Zhu, J. Han, H.-Y. An, et al., "A Novel Embedded Method for in situ Measuring Internal iMultpoint Temperatures of lithium-ion battEries," *Journal of Power Sources* 456 (2020): 227981, https://doi.org/10.1016/j.jpowsour.2020.227981.

399. S. Zhu, L. Yang, J. Wen, et al., "In Operando Measuring Circumferential Internal Strain of 18650 Li-ion Batteries by Thin Film Strain Gauge Sensors," *Journal of Power Sources* 516 (2021): 230669, https://doi.org/10.1016/j.jpowsour.2021.230669.

400. Z. Chen, J. Lin, C. Zhu, et al., "Detection of Jelly Roll Pressure Evolution in Large-format Li-ion Batteries via in Situ Thin Film Flexible Pressure Sensors," *Journal of Power Sources* 566 (2023): 232960, https://doi.org/10.1016/j.jpowsour.2023.232960.

401. M. Nascimento, M. S. Ferreira, and J. L. Pinto, "Real Time Thermal Monitoring of Lithium Batteries with fiber Sensors and Thermocouples: a Comparative Study," *Measurement* 111 (2017): 260–263, https://doi.org/10.1016/j.measurement.2017.07.049.

402. J. Fleming, T. Amietszajew, E. McTurk, D. P. Towers, D. Greenwood, and R. Bhagat, "Development and Evaluation of in situ Instrumentation for Cylindrical Li-ion Cells Using fiber Optic Sensors," *HardwareX* 3 (2018): 100–109, https://doi.org/10.1016/j.ohx.2018.04.001.

403. W. Mei, Z. Liu, C. Wang, et al., "Operando Monitoring of Thermal Runaway in Commercial Lithium-ion Cells via Advanced Lab-on-fiber Technologies," *Nature Communications* 14 (2023): 5251, https://doi.org/10.1038/s41467-023-40995-3.

404. Z. Li, Z. Qu, Z. Jiang, H. Huang, and W. Tao, "Degradation Mechanism of Lithium-ion Battery under Appropriate in-plane Temperature Gradient," *Green Energy and Intelligent Transportation* 4 (2025): 100352, https://doi.org/10.1016/j.geits.2025.100352.

405. Y. Zhu, J. Xie, A. Pei, et al., "Fast Lithium Growth and Short Circuit Induced by Localized-temperature Hotspots in Lithium Batteries," *Nature Communications* 10 (2019): 2067, https://doi.org/10.1038/s41467-019-09924-1.

406. M. S. K. Mutyala, J. Zhao, J. Li, H. Pan, C. Yuan, and X. Li, "In situ temperature Measurement in lithium-ion battEry by Transferable Flexible Thin Film Thermocouples," *Journal of Power Sources* 260 (2014): 43–49, https://doi.org/10.1016/j.jpowsour.2014.03.004.

407. N. Martiny, A. Rheinfeld, J. Geder, Y. Wang, W. Kraus, and A. Jossen, "Development of an All Kapton-Based Thin-Film Thermocouple Matrix for <Italic>in Situ</Italic> Temperature Measurement in a Lithium Ion Pouch Cell," *IEEE Sensors Journal* 14 (2014): 3377–3384, https://doi.org/10.1109/JSEN.2014.2331996.

408. P. Yang, K. Su, S. Weng, et al., "Internal Integrated Temperature Sensor for Lithium-Ion Batteries," *Sensors* 25 (2025): 511, https://doi.org/10.3390/s25020511.

409. J. Amici, P. Asinari, E. Ayerbe, et al., "A Roadmap for Transforming Research to Invent the Batteries of the Future Designed within the European Large Scale Research Initiative BATTERY 2030^{+}," *Advanced Energy Materials* 12 (2022): 2102785, https://doi.org/10.1002/aenm.202102785.

410. L. Yang, N. Li, L. Hu, et al., "Internal Field Study of 21700 Battery Based on Long-life Embedded Wireless Temperature Sensor," *Acta Mechanica Sinica* 37 (2021): 895–901, https://doi.org/10.1007/s10409-021-01103-0.

411. Q. Zhang, C. Didier, W. K. Pang, et al., "Structural Insight into Layer Gliding and Lattice Distortion in Layered Manganese Oxide Electrodes for Potassium-Ion Batteries," *Advanced Energy Materials* 9 (2019): 1900568, https://doi.org/10.1002/aenm.201900568.

412. D. M. Brieske, A. Warnecke, and D. U. Sauer, "Modeling the Volumetric Expansion of the Lithium-sulfur Battery Considering Charge and Discharge Profiles," *Energy Storage Materials* 55 (2023): 289–300, https://doi.org/10.1016/j.ensm.2022.11.053.

413. P. Liu, L. Yang, B. Xiao, et al., "Revealing Lithium Battery Gas Generation for Safer Practical Applications," *Advanced Functional Materials* 32 (2022): 2208586, https://doi.org/10.1002/adfm.202208586.

414. Z. Liu, Y. Lu, X. Ma, et al., "Advanced Functional Optical Fiber Sensors for Smart Battery Monitoring," *Energy Material Advances* 5 (2024): 0142, https://doi.org/10.34133/energymatadv.0142.

415. Y. Li, W. Wang, X.-G. Yang, F. Zuo, S. Liu, and C. Lin, "A Smart Li-ion Battery with Self-sensing Capabilities for Enhanced Life and Safety," *Journal of Power Sources* 546 (2022): 231705, https://doi.org/10.1016/j.jpowsour.2022.231705.

416. X. Zhao, H. He, Z. Wei, R. Huang, H. Yue, and X. Guo, "Embedded fiber Sensing-enabled Multi state Joint Observation of Smart Lithium-ion Battery Based on Distributed Thermal Modeling," *Journal of Energy Storage* 118 (2025): 116085, https://doi.org/10.1016/j.est.2025.116085.

417. Y. Yu, T. Vincent, J. Sansom, D. Greenwood, and J. Marco, "Distributed Internal Thermal Monitoring of lithium-ion battEries with fiber Sensors," *Journal of Energy Storage* 50 (2022): 104291, https://doi.org/10.1016/j.est.2022.104291.

418. Y. Yu, E. Vergori, F. Maddar, Y. Guo, D. Greenwood, and J. Marco, "Real-time Monitoring of Internal Structural Deformation and Thermal Events in Lithium-ion Cell via Embedded Distributed Optical fiber," *Journal of Power Sources* 521 (2022): 230957, https://doi.org/10.1016/j.jpowsour.2021.230957.

419. K. Tan, S. Wang, J. Jiang, et al., "Operando Monitoring Gas Pressure for Accurate Early Warning of Thermal Runaway in Lithium-ion Batteries Induced by Overheating Based on an Optical fiber Fabry–Perot Interferometer," *Journal of Power Sources* 615 (2024): 235096, https://doi.org/10.1016/j.jpowsour.2024.235096.

420. M. Nascimento, S. Novais, M. S. Ding, et al., "Internal Strain and Temperature Discrimination with Optical fiber Hybrid Sensors in Li-ion Batteries," *Journal of Power Sources* 410-411 (2019): 1–9, https://doi.org/10.1016/j.jpowsour.2018.10.096.

421. X. Feng, D. Ren, X. He, and M. Ouyang, "Mitigating Thermal Runaway of Lithium-Ion Batteries," *Joule* 4 (2020): 743–770, https://doi.org/10.1016/j.joule.2020.02.010.

422. A. Su, S. Mao, L. Lu, X. Han, and M. Ouyang, "Implanted Potential Sensing Separator Enables Smart Battery Internal state Monitor and Safety Alert," *eTransportation* 21 (2024): 100339, https://doi.org/10.1016/j.etran.2024.100339.

423. S. Lyu, N. Li, L. Sun, S. Jiao, H. Chen, and W.-L. Song, "Rapid Operando Gas Monitor for Commercial lithium-ion battEries: Gas Evolution and Relation with Electrode Materials," *Journal of Energy Chemistry* 72 (2022): 14–25, https://doi.org/10.1016/j.jechem.2022.04.010.

424. Y. Jin, Z. Zheng, D. Wei, et al., "Detection of Micro-Scale Li Dendrite via H2 Gas Capture for Early Safety Warning," *Joule* 4 (2020): 1714–1729, https://doi.org/10.1016/j.joule.2020.05.016.

16146840, 2026, 26, Downloaded from https://advanced.onlinelibrary.wiley.com/doi/10.1002/aenm.71073 by Jilin University, Wiley Online Library on [07/11/2026]. See the Terms and Conditions (https://onlinelibrary.wiley.com/terms-and-conditions) on Wiley Online Library for rules of use; OA articles are governed by the applicable Creative Commons License